University of Sheffield

Department of Civil and Structural Engineering

Shear Strength and Volume Change Behaviour of Unsaturated Soils

Volume 2

Chapter 6 and 7, References and Appendices

by

Mohd.Jamaludin bin Md.Noor

A thesis submitted to

The University of Sheffield

Department of Civil and Structural Engineering

for the degree of Doctor of Philosophy

July 2006

CONTAINS PULLOUTS

Table of Contents

VOLUME 1

Chapter 6
Discussion

This chapter starts by considering the specimen consistency, test repeatability and the comparability between the results of the single stage and multistage triaxial tests. This is followed by discussion of the potential effects of the particle breakage on the definition of failure. The test results are then interpreted according the proposed shear strength model and the shear strength-volume change framework. From the soil-moisture characteristic curve and the saturated and unsaturated shear strength behaviour, the warped-surface extended Mohr-Coulomb envelope of the test material has been derived. This is followed by the presentation of the unique relationship of $\phi'_{\min_{mob}} - \varepsilon_a$ which supports the application of the Rotational Multiple Yield Surface Framework in modelling soil responses. This is also to provide evidence that the rotation of the mobilized shear strength envelope about the suction axis is acting as the growing yield surface as the soil undergoes compression. Then the applicability of the framework in predicting the soil stress-strain behaviour is demonstrated. Finally the soil volume change behaviour for wetting and loading collapse in the Rowe cell compression tests is discussed.

6.1 Specimen Consistency.

The specimen consistency in the pressure plate test in test series A is ensured by the use of the same dry mass of specimen which was compacted into the same volume in every test where a consistent dry density of 1.74Mg/m^3 was achieved. The specimens were taken from a uniformly mixed test sample.

The consistency of the compacted specimens for the triaxial tests in test series B and C was confirmed by the consistent diameters, heights and dry densities obtained. Due to the slightly different specimen preparation techniques for the saturated and unsaturated specimens the heights of the saturated specimens are expected to be slightly greater. Their dry densities narrowly varied between 1.73 and 1.75Mg/m^3 as shown in Tables 5.2 and 5.5 for the saturated and unsaturated specimens respectively, irrespective of the moisture content during compaction. This is probably due to the clean granular particles of the test material. Most important of all, the necking formed due to the sliding method of specimen placement previously used by Salman (1995)

was overcome. This was a consequence of a consistent specimen preparation technique and an effective placement procedure. As expected, a lower but consistent, dry density was obtained for the loosely prepared saturated specimens reported in Table 5.2.

Identical dry densities of 1.64Mg/m^3 were obtained for test series D specimens of particle size varying between 5 to 10mm. This is due to the uniformity of the sieved material used and the consistent specimen preparation and placement technique applied similar to the preparation of the loose specimens in test series B.

A consistent specimen dry density that varied between 1.45 and 1.47Mg/m^3 was obtained for the Rowe cell compression tests in test series E. This was the result of using the same dry mass and a consistent pouring technique.

6.2 Test Repeatability.

Table 5.1 shows the results for the pressure plate test in test series A. Repeat tests were conducted for suctions of 6, 10, 15 and 20kPa and maximum moisture content variation of 0.7, 0.07, 0.08 and 0.08% respectively were obtained. This small variations of percentage moisture content in the repeat pressure plate tests showed good test repeatability and the resultant soil-moisture characteristic curve is plotted in Figure 5.1.

The effective stress and the corresponding deviator stress at failure for the triaxial tests on saturated specimens in test series B are listed in Table 5.3. The saturation of all the saturated triaxial specimens was carried out until a minimum Skempton's B value of 0.92 was achieved as recorded in Table 5.3. In practice, the values ranged from 0.92 to 1.0 with an average value of 0.97. This was the final step taken to make sure that the specimens' initial conditions were as consistent as possible in every test before the consolidation and the shearing stages were commenced. The repeatable test procedure applied is expected to give repeatable results. However, there was a slight variation in the test procedure for the multistage test on specimen compacted at 4% moisture content, i.e. test code S4%MST1. In this test the cell and back pressures were reduced from 390kPa and 340kPa at the end of saturation stage to 190kPa and 90kPa respectively. The result of this inconsistency in the test procedure has produced

a slightly lower deviator stress at failure than in the rest of the tests. Figure 6.1 shows a slightly lower shear strength envelope for test code S4%MST1 compared to S4%MST2. Therefore the result of this test was excluded in the repeatability check, which covers the deviator stress at failure for both the single stage and multistage tests. The deviator stress at failure for shearing of compacted specimens at a nominal effective stress of 100kPa are 563, 614, 600 and 580kPa for test codes S4%SSES100, S6%SSES100, S8%SSES100 and S12%MST1ES100 respectively, at effective stress of about 200kPa are 813, 867, 871, 833 and 822kPa for test codes S4%SSES200, S6%SSES200, S8%SSES200, S4%MST2ES200 and S12%MST2ES200 respectively and at effective stress of about 300kPa are 915, 1074, 980 and 974kPa for test codes S4%SSES300, S8%SSES300, S4%MST2ES300 and S12%MST2ES300 respectively. The maximum variations of deviator stress at failure for these tests at effective stresses of 100, 200 and 300kPa are 8.3, 6.7 and 14.8% respectively.

There were no repeat tests for test series C, D and E. However the reliability of the results in test series C depends on the comparability between the single stage and multistage tests in test series B that will be discussed in the following section. The reliability of test series E is totally dependent on the repeatability of similar tests conducted by Goodwin (1991). These tests that used the same modified Rowe cell and an almost similar test material obtained from the same quarry, showed excellent repeatability. As a similar test procedure had been adopted the results of test series E are assumed to be repeatable.

6.3 Comparability between Single Stage and Multistage Triaxial Tests.

The consistency in the prepared specimen dimensions, dry densities, and the repeatability in the test procedure adopted for the triaxial tests on saturated specimens discussed earlier should give comparable results between single stage and multistage tests if the latter procedure is valid.

Section 6.2 has proved the repeatability between these two types of triaxial test at effective stresses of 100, 200 and 300kPa and therefore confirmed their comparability. This thereby confirmed the reliability of the multistage test on saturated specimens and thus would indicate the reliability of the similar tests on unsaturated specimens since the only difference in conditions between them is the

presence of suction in the unsaturated specimens. Therefore any difference in deviator stress at failure must be attributed to the suction in the unsaturated specimens. The result for the multistage triaxial test on saturated specimens compacted at 4% moisture content has to be omitted again due to the inconsistent test procedure adopted.

The reliability of multistage triaxial tests on unsaturated specimens is also supported by the work of Ho and Fredlund (1982) where a similar "cyclic loading" procedure was adopted.

6.4 Membrane Penetration.

A problem when dealing with coarse-grained soils is the penetration of the rubber membrane into the interstices between the outer particles of the specimen when the cell pressure is increased during the consolidation stage of a triaxial test. This causes errors in the measurements of specimen volume change during consolidation. A reasonable and accurate technique is required to determine the volume change due to membrane penetration. Some researchers like Molenkamp and Langer (1981), Baldi and Nova (1984) and Kramer *et al.* (1990) have developed theoretical equations to determine the volumetric strain due to membrane penetration. Their theoretical equations are a function of cell pressure, mean grain size, specimen diameter, membrane elastic modulus and thickness and a constant factor. The only difference between their equations is the constant factor. However there is a problem in the selecting the most appropriate equation for the current tests and the selection of the right value for the parameters to be used in the equation. A slight change in values would give a different value of volumetric strain and this could jeopardise the end result. Thus the best way for determining the membrane penetration is by judging it from the consolidation curve based on reasonable assumptions as described for the saturated and unsaturated triaxial specimens in Sections 5.2.3 and 5.3.3 respectively. The results of the two different methods used for the determination of volume of membrane penetration in the saturated and unsaturated tests have shown a reasonable comparability between them. Nonetheless the accuracy of these methods would have been better if a faster data logging rate had been applied for the tests on unsaturated specimens. Then the point of divergence from linearity could have been determined to support the derivation made from the lateral shrinking of the specimen.

6.5 Stress, Strain and Volume Change Behaviour of Triaxial Specimens.

The deviator stress and the volumetric strain during shearing for the unsaturated specimens are calculated by assuming the specimen volume change indicated by the VCU is uniformly distributed within the gauge height (i.e. 200 mm) of the specimens. This is to avoid to the non-uniform deformation of the specimen affected by end friction. The specimen's effective cross sectional area A' is based on the measured volume change and the measured internal axial strains. On the other hand the deviator stress and the volumetric strains during shearing for the saturated specimens are calculated based on the measured volume change and assuming a uniform distribution throughout the whole specimen height. This is because there is no internal strain measurements were carried out for the saturated specimens.

The generalized behaviour of both the saturated and the unsaturated specimens can be summarized as follows:

1. The graphs (e.g. Figures 5.14 and 5.20) that show a well defined peak deviator stress have a well defined dilation point on the graph of ε_v versus ε_a.
2. The graphs for compacted specimens with well defined peak stress are those tested at effective stresses of 100, 200 and 250 kPa, the apex is achieved at variable axial strain less than 1.0% and the dilation point occurs at axial strain just before the point of peak stress.
3. For compacted specimens at an effective stress or net stress of 300 kPa that show a continuously increasing deviator stress after 1.0% axial strain, the dilation point is at higher axial strains, and some specimens show a continuous contraction during shearing.
4. The compressive volumetric strains measured at peak deviator stress increase almost linearly with confining pressure (e.g. Figures 5.15 and 5.21).

The variability of axial strain at peak deviator stress for similar effective stresses of less than 300 kPa, as noted in point no. 2 above, is taken as a sign of the occurrence of particle breakage during shearing. This is supported by the works of Bishop (1966) and Billam (1972). The similar behaviour at elevated effective stresses reported by Indraratna *et al.* (1993) and Futai and Almeida (2005) when testing coarse-grained

soils, as presented in Section 2.3.3 may be attributed to particle breakage. Even though in the sample preparation procedure described in Section 4.2.1 the softer particles of shale were ground down in 10 minutes mixing in a 30kg concrete mixer, in some specimens some of them could still remain and cause this variability in the stress-strain and volume change behaviour. Therefore, if the variability in behaviour is caused by particle breakage of the softer remaining shale bits then this could be the reason for the occurrence of peak stress at higher axial strains for tests at effective stress of 300 kPa.

The inconsistency in the volume change behaviour during shearing for specimens tested at an effective stress of 300 kPa as noted in point no.3 above, also implies variability in the constituent soil particles. The continuous specimen contraction during shearing of the compacted specimens is also an indication of the occurrence of particle breakage according to Bishop (1966) and Billam (1972) for tests at elevated stress levels. This type of stress-strain and volume change behaviour is similar to the graphs for greywacke rockfill at net cell pressures of 600 kPa in Figure 2.12(a) and (b) reported by Indraratna *et al.* (1993). When dilation is suppressed by the higher confining pressure it causes particle breakage and this is responsible for the continuous specimen contraction at failure. The almost linear increase in the compressive volumetric strains at peak deviator stress at increasing confining pressure as noted in point no. 4 above is typical volume change behaviour in drained triaxial compression test on coarse-grained soils as reported by Indraratna *et al.* (1993) as review in Section 2.3.3.

However, another possibility for this kind of volumetric strain behaviour where it is contracting towards a constant value while the deviator stress is levelling off is the onset of a critical state condition. This characteristic is shown in the third shearing stage for unsaturated specimens at suction 60 and 90 kPa (Figures 5.35 and 5.36). Since the internal axial and radial strains were measured in these tests then Equation 2.10 can be applied to check whether the specimens have attained the critical state condition. The equation indicates that the volumetric strain, ε_v, for a drained triaxial test is the sum of twice the radial strain and axial strain. Therefore if the graphs of twice the radial strain plus axial strain are plotted against axial strain as shown in

Figures 6.2(a)-(d), it would indicate the volumetric strain behaviour of the specimens during shearing based on the measured local radial and axial strains. If the graph tends towards the horizontal then it indicates that the shearing is approaching the critical state condition. This volumetric strain behaviour can be compared with that indicated by the large (1770 cc) volume change unit.

The graphs of $2\varepsilon_r + \varepsilon_a$ versus ε_a for the third shearing stage on all unsaturated specimens at suctions of 25, 50, 60 and 90 kPa are shown in Figures 6.2(a)-(d) respectively. The graphs in Figures 6.2(a)-(c) indicate that the specimen was still dilating to the end of the shearing stage. On the other hand the graph in Figure 6.2(d) for 90 kPa suction is showing that the specimen was contracting from the point of application of the deviator stress up to the failure point and continuing to contract after the failure point where the deviator stress is slowly continuing to increase as shown in Figure 5.36. Therefore, even though the graphs of deviator stress versus axial strain for the third shearing stage on all unsaturated specimens at suctions of 25, 50, 60 and 90 kPa shown in Figures 5.33 – 5.36 respectively are levelling off at higher axial strains, their volumetric strain behaviour is not indicating the onset of a critical state. Possibly the graph in Figure 6.2(d) is indicating the occurrence of particle breakage since the specimen continuously contracting during shearing.

These results correspond with the volumetric strain behaviour indicated by the volume change unit, except for the specimen with a suction 60 kPa where the volume change unit indicated a continuous specimen contraction (refer Figure 5.39) and the measurement of the local radial and axial strains (refer Figure 6.2(c)) indicated the opposite. The reason for this difference is not understood. The possibility of the leakage in the volume change unit is very unlikely since the tube lines and connections were thoroughly inspected while carrying out the tests. Also the calibration drift for this volume change unit is negligible as indicated in Table 4.9. As the volumetric strain according to the local displacement transducers indicates that the shearing has not reached a critical state condition, the inconsistency in behaviour could be attributed to particle breakage. The continuously increasing deviator stress towards a higher axial strain at failure (i.e. more than 1.0% axial strain) beyond the normal axial strain at failure for the shearing at a lower net confining stress (i.e. less

than 1.0% strain) is attributed to the particle breakage according to Bishop (1966) and Billam (1972). This type of stress-strain and volume change behaviour at elevated net confining stress was similar to the graphs reported by Indraratna *et al.* (1993) and Futai and Almeida (2005) as presented in Section 2.3.1. Therefore the continuing increase in the deviator stress at axial strains higher than 1.0% in Figures 5.13, 5.15, 5.17, 5.18, 5.35 and 5.36 are prone to indicate the occurrence of particle breakage. In other words particle breakage in coarse-grained soils is inclined to be responsible for the increase in the deviator stress which is similar to the stress-strain behaviour for normally consolidated clays. The following section introduces the graph of mobilized friction angle, ϕ'_{mob}, versus void ratio, e, which can be an additional indication of particle breakage.

6.5.1 Detection of Particle Breakage on the Graphs of Mobilized Friction Angle, ϕ'_{mob}, Versus Void Ratio, e.

Figures 6.3(a) and 6.3(b) shows plots of mobilized friction angle versus void ratio for the compacted specimens in test series B and C at the limited range of values for clarity. It can be noticed that in some of the graphs in Figure 6.3(a) there is a sharp change in curvature, e.g. the graphs for S4%SSES300 (i.e. thickest yellow line) and S12%MSES300 (i.e. thickest pink line). The kink in the graphs is indicating a sharp reduction in void ratio and this is suspected to be due to particle breakage which fill up the void spaces with the smaller chipping material. Then if their corresponding plots of volumetric strain versus axial strain shown in Figures 5.19 and 5.24 respectively are studied, it can be seen that the dilation began at about 2.5% axial strain in both cases. These points correspond to the minimum void ratio in the considered graphs in Figure 6.3(a). The particle breakage is suspected to be taking place at axial strain lesser than 2.5% at the point where there is a sharp reduction in void ratio indicated by the kink in the graphs. The subsequent gradual increase in the deviator stress beyond axial strain of 2.5% as shown in Figures 5.13 and 5.18 is due to the specimen dilation as indicated by the graphs in Figures 5.19 and 5.24. However whether the earlier occurrence of particle breakage is influencing the succeeding gradual increase in the deviator is uncertain.

Figure 6.3(b) shows identical lines of gradient $\frac{\Delta\phi'_{mob}}{\Delta e}$ for shearing of saturated and unsaturated triaxial test specimens at effective or net stresses of 100kPa. The onset of a linear variation of ϕ'_{mob} relative to void ratio before reaching the point of minimum void ratio could be a characteristic of a "no breakage" condition, since this characteristic is not likely to occur at effective stresses higher than 100 kPa for this material.

The plots of mobilized friction angle versus void ratio for specimens compacted at 4% and 6% moisture content sheared at effective stresses of 100 and 200 kPa in Figure 6.3 have been redrawn with a larger horizontal scale in Figure 6.4(a). There is a divergence from linearity for the graph of S4%SSES200 compared to the linear section in the graph of S6%SSES200. This could be taken as another criteria for the sign of particle breakage. Reference to the graph of deviator stress versus axial strain for S4%SSES200 (Figure 5.13) shows that the deviator stress remained constant after the specimen starts to dilate as shown by graph no. 2 in Figure 5.19, which is at 0.6 % axial strain.

This suggests that only when the specimen continuously undergoes contraction while the deviator stress is continuously increasing and correspondingly the graph of $\phi'_{mob} - e$ shows a sharp reduction in void ratio then particle breakage can be suspected to occur. The close up views at the plots of mobilized friction angle versus void ratio for the shearing at an effective stress of 100kPa in Figure 6.4(a), show a distinct linear behaviour before the dilation point. This characteristic of the graph of $\phi'_{mob} - e$ is proposed as a sign for the condition of "no particle breakage". Correspondingly, the graphs of deviator stress versus axial strain for tests S4%SSES100 and S6%SSES100 in Figures 5.13 and 5.14 respectively show well defined peaks to indicate strain softening after the dilation point when there is likely to be no particle breakage.

If the graph of mobilized friction angle versus void ratio for test S8%SSES300 is redrawn with a bigger void ratio scale as shown in Figure 6.4(b) it can be seen that there is a sharp reduction in void ratio followed by a clear divergence from linearity. This is to mark that the rate that void ratio decrease is increasing to indicate the

occurrence of particle breakage. If the corresponding plots of deviator stress, cell pressure, pore water pressure and specimen volume change versus axial strain are redrawn, as in Figure 6.5, it can be seen that the breakage is suspected to occur when axial strain is approaching the point of minimum volumetric strain. Beyond that, the specimen dilation is responsible for the increase in the deviator stress. Then the earlier occurrence of particle breakage is again suspected to influence the succeeding gradual increase in the deviator stress. However the manner of the influence is uncertain.

The particle size distribution curve taken after shearing for test S8%SSES300 is shown by curve number 4 in Figure 4.1. There is a slight increase in the proportion of particle sizes less than 5mm compared to curve number 2, which represents the general initial particle size distribution before shearing. This therefore provides evidence that particle breakage has occurred and could be the cause of the graph of mobilized friction angle versus void ratio diverging from linearity as it approaches the dilation point. This supports the earlier proposition that either a kink or divergence from linearity in the graph of $\phi'_{mob} - e$ as a sign of particle breakage. Besides, the different gradient of the linear section of the graph of $\phi'_{mob} - e$ for different effective or net stresses (Figures 6.3(a) and 6.4(a)) indicates that it doesn't exhibit a unique relationship and thus cannot be the basis for the formulation of the shear strength-volume change framework.

6.5.2 Effect of Particle Breakage on Definition of Failure.

Section 2.3 has discussed the two types of the graph of deviator stress versus axial strain where one shows a well defined peak and the other shows a continuously increasing deviator stress after a kink. The failure point for the first type of graph is taken at the maximum deviator stress and for the second type of graph is either taken at the kink in the graph or at an arbitrary strain. A problem arose when some of the graphs of deviator stress versus axial strain showed a slightly different behaviour where, upon approaching the peak deviator stress, the trend suddenly changes to a continuously increasing deviator stress instead of decreasing. This is probably due to particle breakage as discussed in Sections 5.2.4 and 5.3.4. Particle breakage is seemed to cause an increase in the deviator stress at a much slower rate than the first phase. Failure is taken at the point that the deviator stress started to undergo the slower

increase rate, which is estimated i.e. at 0.2% strain after the first kink since particle breakage is taken as one of the criteria for failure.

6.6 Effect of Grading on the Shear Strength.

A specimen with uniform grading (i.e. test series D) has less total contact area between grains when compared to a well graded specimen. By using a uniform and a wider graded material the effect of this overall contact area on the shear strength envelope can be investigated. This may then be linked to particle breakage which results in an increase in the overall particle contact area and an increase in strength.

This was investigated by conducting triaxial tests on saturated specimens of material retained on a 5mm diameter sieve in test series D (grain size distribution curve is given by curve no. 3 in Figure 4.1). The specimens were loosely prepared to avoid particle breakage and the applied effective stresses were 100 and 200kPa; the results are presented in Table 5.10. These results are compared with the results of triaxial tests on loosely prepared specimens presented in Table 5.3 marked as test codes S0%SSES100, S0%SSES200 and S0%SSES300. The corresponding shear strength envelopes for these grading are obtained by drawing Mohr circles as shown in Figure 6.6. For the loosely prepared saturated specimens of the normal test material the transition effective stress, $(\sigma - u_w)_t$, transition shear strength, τ_t, and the minimum internal friction angle, ϕ'_{min}, are estimated to be 300kPa, 265kPa and 28° respectively. For the loosely prepared specimen with test material retained on a 5mm diameter sieve the transition effective stress, $(\sigma - u_w)_t$, transition shear strength, τ_t, and the minimum internal friction angle, ϕ'_{min}, are estimated to be 300kPa, 275kPa and 30° respectively. Apparently, the shear strength for the coarser material of uniform grading is slightly higher than the loosely prepared "well graded" grading. Therefore there is no evidence in this particular case that the greater overall contact area between grains is giving higher shear strength.

6.7 Shear Strength of the Test Material.

The shear strength of the test material according to the proposed warped-surface shear strength model formulated specifically for coarse-grained soils is plotted based on the saturated and unsaturated shear strength behaviour, plus the point of maximum

apparent shear strength according to the soil-moisture characteristic curve. The procedure for obtaining the seven soil shear strength parameters that are required for the plotting of the warped-surface shear strength envelope has been described in Section 3.2.5. The shear strengths parameters were obtained from consolidated drained triaxial tests on saturated and unsaturated specimens in test series B and C respectively. The data obtained from the consolidated drained triaxial tests on loosely prepared saturated specimens (i.e. S0%SSES100, S0%SSES200 and S0%SSES300) are omitted in the derivation of the warped-surface shear strength envelope of the test material due to the slightly low shear strength attained.

In the consolidated drained triaxial tests, both the saturated and unsaturated specimens were sheared at strain rate of 0.0256mm/min. This strain rate was chosen since during trial consolidated drained triaxial tests on both saturated and unsaturated specimens this rate was slow enough not to cause any increase in the pore water pressure. This strain rate also satisfied the requirement (Head, 1981) that a minimum time for failure must be 2 hours. According to the past applied strain rate for triaxial tests on unsaturated specimens as listed in Table 6.1, this strain rate is the second fastest rate applied for granular soil and proved to be appropriate for the test material.

6.7.1 Saturated Shear Strength.

The Mohr circles based on data obtained from effective stress analysis for saturated conditions, as presented in Table 5.3, are plotted in Figure 6.7(a) and the Mohr Coulomb envelope for saturated conditions is sketched to enclose the Mohr circles. The Mohr circles for the loosely prepared specimens (i.e. S0%SSES100, S0%SSES200 and S0%SSES300) and for the multistage test on a specimen compacted at 4% moisture content (i.e. S4%MSES100, S4%MSES200 and S4%MSES300) are omitted here. Figure 6.7(b) shows the shear strength parameters and the minimum internal friction angle, ϕ'_{min} for the deduced Mohr Coulomb envelope. The transition effective stress, $(\sigma - u_w)_t$, transition shear strength, τ_t, and the minimum internal friction angle, ϕ'_{min}, are estimated to be 200kPa, 230kPa and 34° respectively.

Substituting these first two shear strength parameters (i.e. $(\sigma - u_w)_t$ and τ_t) and the minimum internal friction angle, ϕ'_{min}, into Equations 3.13, 3.14 and 3.15 will produce Equations 6.1 and 6.2 which are the shear strength equations of the test material for saturated conditions.

$$\tau_{sat_f} = \frac{(\sigma - u_w)}{200}\left[1 + \frac{200 - (\sigma - u_a)}{N \times 200}\right]230 \qquad \text{Equation 6.1}$$

where $N = \dfrac{1}{1 - \left[200 \times \dfrac{\tan 34°}{230}\right]} = 2.41855$

for $(\sigma - u_a) \leq 200kPa$

$$\tau_{sat_f} = (\sigma - u_w)\tan 34° + [230 - 200\tan 34°] \qquad \text{Equation 6.2}$$

for $(\sigma - u_a) \geq 200kPa$

The shear strength envelope drawn in Figure 6.7 was plotted based on these equations and it defines the minimum shear strength of the test material.

The saturated condition shear strength envelope obtained for the triaxial tests on loose poured specimens is slightly lower than that of the compacted specimens as shown in Figure 6.8. The transition effective stress, $(\sigma - u_w)_t$, transition shear strength, τ_t, and the minimum internal friction angle, ϕ'_{min}, are estimated to be 300kPa, 265kPa and 28° respectively.

6.7.2 Unsaturated Shear Strength.

The value of residual suction that corresponds to the maximum apparent shear strength is determined at 15kPa from the soil moisture characteristic curve as shown in Figure 5.1 and discussed in Section 5.1. Therefore the curve that represents the variation of apparent shear strength with respect to suction must have its vertex at a suction of 15kPa.

The consolidated drained triaxial shear strength tests on unsaturated specimens were conducted at suctions of 25, 50, 60 and 90kPa. These tests were to determine the magnitude of the apparent shear strength at the respective suction and effective stress.

The specimens were compacted at 4% moisture content except for the test at suction 90kPa which was compacted at 1% moisture content. The latter was intended to accelerate the equalization stage. It reduced it from between 4 to 6 weeks to just less than one week as indicated by the equalization curves shown in Figure 5.11. This was carried out after realizing that the moisture content of the specimen at compaction did not have a significant effect on the shear strength envelope as long as the specimens were compacted in a similar way. The similarities in the shear strength envelopes may be attributed to the almost equal specimen initial dry densities as shown in Table 5.5. This can be seen from the results of the saturated shear strength tests in test series B which gave a single shear strength envelope as shown in Figure 6.7(a), despite the specimens being compacted at different moisture contents.

Once a specimen has equalised, i.e. when the outflow of moisture from the specimen is less than 0.05cc in 12 hours, it is ready for the consolidation and shearing stages. The consolidation and shearing were performed by the multistage triaxial test method described in Section 4.5.3.7. All of the specimens were consolidated and sheared at effective stresses of 100, 200 and 300kPa. The cell pressure, pore air pressure and pore water pressure applied in every test are shown in Table 5.7.

The graphs of deviator stress and specimen volume change versus internal axial strain are shown in Figures 5.33 – 5.36 and Figures 5.37 – 5.40 respectively. From the graphs of deviator stress versus internal axial strain the deviator stress at failure for each case was determined and the results are listed in Table 5.7. The major principal net stress is taken as the sum of the failure deviator stress, $\Delta\sigma_f$, and the net stress, $(\sigma_3 - u_a)$, while the minor principal stress is taken as the net stress. From these data the Mohr circles are drawn for each suction case as shown in Figures 6.9 - 6.12. In the same figures the shear strength envelope at saturation was also drawn and the distance the Mohr circles extend vertically above the envelope is taken as the apparent shear strength with respect to the corresponding net stress and suction (refer Section 3.2.2). If the Mohr circle just touches or lies slightly below the envelope, the apparent shear strength was considered to be zero. The total shear strength is taken as the sum of the apparent shear strength and the shear strength at saturation. Table 6.2 summarizes the apparent and the total shear strength obtained in each case.

6.7.3 Warped-surface Shear Strength Envelope.

The shear strength behaviour of the test material according to the new 3-D warped-surface extended Mohr-Coulomb envelope is obtained from the interpretation of the results in test series A, B and C. Section 6.4.1 has identified two shear strength parameters which are transition effective stress, $(\sigma - u_w)_t$, and transition shear strength, τ_t, and the soil inherent property, which is the minimum internal friction angle, ϕ'_{min}. Section 6.4.2 has identified the magnitude of residual suction, $(u_a - u_w)_r$, which is the result of test series A. The data from the shear strength tests on unsaturated specimens discussed in Section 6.4.2 have been used to determine the remaining three shear strength parameters, which are the maximum apparent shear strength, c_s^{max}, rate of increase of ultimate suction with respect to net stress, ς, and ultimate suction at zero net stress, $(u_a - u_w)_u^{\sigma'=0}$.

The next step is to determine the maximum apparent shear strength, c_s^{max}, by extrapolating from the variation of the apparent shear strength with respect to suction at suctions of 25, 50, 60 and 90kPa and the three different net stresses of 100, 200 and 300kPa. The apparent shear strengths at the respective effective stress and suction are summarized in Table 6.2. The graphs for variation of apparent shear strength with respect to suction relative to the saturated shear strength at effective stress of 100, 200 and 300kPa are drawn as in Figure 6.13. In other words the figure considers the apparent shear strength for the respective net stress, and not the sum of the saturated and apparent shear strength. From here the maximum apparent shear strength, c_s^{max} is estimated as 30kPa corresponding to a suction of 15kPa (i.e. residual suction). At the same time Figure 6.13 helps to estimate the values of ultimate suction with respect to the effective stresses applied.

The ultimate suction for the respective effective stress is the value of suction at the point where the graph returns to the suction axis. From the values of ultimate suctions for the three graphs in Figure 6.13, the variation of ultimate suction relative to effective stress is drawn as in Figure 6.14. This is based on the assumed linear variation according to Equation 3.14 proposed in Section 3.2.2. From here the rate of

increase of ultimate suction with respect to effective stress, ζ, for the test material is deduced as 0.05. The value of ultimate suction at effective stress zero, $(u_a - u_w)_u^{\sigma'=0}$ is deduced by extrapolating the line and a value of 50kPa is obtained. At this stage all of the seven shear strength parameters have been deduced and are summarized in Table 6.3. Consequently the 3-D warped-surface Mohr-Coulomb shear strength envelope of the test material can be defined and drawn using the four shear strength equations i.e. Equations 3.22 - 3.25.

Substituting the seven estimated shear strength parameters into Equation 3.15, 3.20, 3.21, 3.22 and 3.23 will produce Equation 6.3 - 6.7 respectively.

$$(u_a - u_w)_u = 0.05(\sigma - u_a) + 50 \qquad \text{Equation 6.3}$$

$$\tau_f = \frac{(\sigma - u_a)}{200}\left[1 + \frac{200 - (\sigma - u_a)}{2.41855(200)}\right]230 + \frac{(u_a - u_w)}{15}\left[1 + \frac{15 - (u_a - u_w)}{15}\right]30$$

..... Equation 6.4

Valid for Zone 1 where suction; $0 \geq (u_a - u_w) \leq 15\,\text{kPa}$ and effective stress; $0 \geq (\sigma - u_a) \leq 200\,\text{kPa}$.

$$\tau_f = \frac{(\sigma - u_a)}{200}\left[1 + \frac{200 - (\sigma - u_a)}{2.41855(200)}\right]230 + 30\left[\frac{(u_a - u_w)_u - (u_a - u_w)}{(u_a - u_w)_u - 15}\right] \times \left[1 - \frac{15 - (u_a - u_w)}{(u_a - u_w)_u - 15}\right]$$

..... Equation 6.5

Valid for Zone 2 where suction; $15kPa \geq (u_a - u_w) \leq (u_a - u_w)_u$ and effective stress; $0 \geq (\sigma - u_a) \leq 200\,\text{kPa}$.

$$\tau_f = (\sigma - u_a)\tan 34° + [230 - 200\tan 34°] + \frac{(u_a - u_w)}{15}\left[1 + \frac{15 - (u_a - u_w)}{15}\right]30$$

..... Equation 6.6

Valid for Zone 3 where suction; $0 \geq (u_a - u_w) \leq 15\,\text{kPa}$ and effective stress; $(\sigma - u_a) \geq 200\,\text{kPa}$.

$$\tau_f = (\sigma - u_a)\tan 34° + [230 - 200\tan 34°] + 30\left[\frac{(u_a - u_w)_u - (u_a - u_w)}{(u_a - u_w)_u - 15}\right] \times \left[1 - \frac{15 - (u_a - u_w)}{(u_a - u_w)_u - 15}\right]$$

..... Equation 6.7

Valid for Zone 4 where suction; $15kPa \geq (u_a - u_w) \leq (u_a - u_w)_u$ and effective stress; $(\sigma - u_a) \geq 200\,\text{kPa}$.

These equations are the five shear strength equations needed to define the extended warped-surface Mohr-Coulomb envelope for the test material. These equations were used to draw the analytical contour lines in Figure 6.15 which is the extended warped-surface Mohr-Coulomb envelope plotted in two-dimensions. It will be noticed that the analytical contours for effective stresses of 100, 200 and 300kPa closely match the corresponding experimental data points. These results thereby validate the applicability of the proposed five shear strength equations (Equations 3.14, 3.22, 3.23, 3.24 and 3.25). The smooth analytical contour lines plotted in Figure 6.15 using these equations indicate that the equations manage to produce a smooth transition between zones.

The shear strength equations of the test material (Equations 6.3 - 6.7) were then used to plot a three-dimensional perspective view of the envelope as shown in Figures 6.16 and 6.17 using software called Origin. They were plotted for a net stress range from zero to 500kPa with increments of 50 kPa, and a suction range from zero to 90kPa, with increments of 5kPa. The seven shear strength parameters listed in Table 6.3 representing dimensions in the shear strength model are shown in Figure 6.17.

The perspective view of the plotted warped-surface Mohr-Coulomb envelope shown in Figures 6.16 and 6.17 shows a smooth transition between the four zones on the envelope surface. This proves the applicability of the proposed shear strength equations to map exactly with the anticipated physical model (i.e. extended warped-surface Mohr-Coulomb shear strength envelope) as shown in Figure 3.3. The fact that the proposed shear strength equations are able to map closely with the laboratory shear strength behaviour as shown in Figures 3.3, 3.4, and 3.5 provides supporting evidence for their general applicability.

6.8 Prediction of Soil Response by the Shear Strength-Volume Change Framework.

Suction between soil particles provides an extra effective stress. Inundation is actually reducing the magnitude of the suction between the particles and thereby implies that the soil compression due to inundation is occurring under effective stress decrease. This is contrary to the Terzaghi's theory of effective stress which implies that soil compression occurs under an increase in effective stress. The soil compression under

the reducing effective stress is the main difficulty in formulating behaviour under a single framework. The problem faced by the critical state framework to model volume change due to alternate wetting and drying is suspected to be due to the consideration of failure purely based on suction changes without considering the combined effect of principal stresses and suction together. These problems have been accounted for through the changes in net stress and suction within the extended Mohr-Coulomb space according to the proposed volume change framework.

The proposed volume change framework is specifically developed based on the soil stress-strain behaviour to predict the response of coarse-grained unsaturated soils at low stress levels due to different types of loading condition. The low stress level condition limits the framework to stress at which no particle breakage occurs during the soil compression or shearing. Failure is considered to occur at identical axial strain for any stress level within this low stress range. The occurrence of particle breakage will cause failure at inconsistent axial strains and this will stop the mobilized shear strength envelope acting as the yield surface and therefore invalidate the applicability of the framework. This is an effort to explain the volume change behaviour of coarse-grained soils under different types of stress changes such as the stress conditions during wetting and loading collapse. The framework is based on the concept of progressive failure by stress equilibrium between mobilized shear strength and the soil state of stress, and assuming that the mobilized shear strength envelope is the yield surface in the extended Mohr Coulomb space defined by the unique relationship of $\phi'_{\min_{mob}} - \varepsilon_a$. These concepts will be applied to interpret the soil behaviour in the triaxial compression tests on saturated and unsaturated specimens conducted in this research.

The qualitative simulation of soil compression in the volume change framework proposed in Section 3.4 suggests that the rotation of the mobilized shear strength envelope is representing the increase in axial strain. The location of the mobilized shear strength envelope is represented by the mobilized minimum friction angle, $\phi'_{\min_{mob}}$, and the axial strain, ε_a, is taken as the yield parameter. Furthermore, the framework is proposing that the mobilized shear strength envelope is representing the yield surface. Every point on a yield surface is representing identical axial strain even

though of different effective or net stresses. For this to be true then the plots of $\phi'_{\min_{mob}}$ versus ε_a for different effective or net stresses must be unique whereby they must overlap to represent a single relationship.

The mobilized shear strength envelope is a curvilinear surface, therefore it cannot be represented by the angle ϕ'_{mob} since the value varies with effective or net stresses. Alternatively the effective mobilized minimum friction angle, $\phi'_{\min_{mob}}$, is used to establish the position of the envelope. The unique relationship of $\phi'_{\min_{mob}}$ - ε_a is explicit to the soil state of compactness defined through the mobilized friction angle, ϕ'_{mob}, where the changes in $\phi'_{\min_{mob}}$, is defined based on the changes in ϕ'_{mob} (refer to Equation 3.34). The mobilized friction angle is an intrinsic soil property and independent of the stress condition as discussed in Section 2.3.1. This is similar to the unloading of shear stress at point A in Figure 2.4(a) where it does not affect the mobilized friction angle, ϕ'_{mob}, and in fact acts like a recorded history of the soil. Whenever the mobilized friction angle is exceeded during the reloading path the soil will automatically react by elastic-plastic compression. Therefore the relationship $\phi'_{\min_{mob}}$ - ε_a is assumed to be independent of the types of stress condition. This will support the applicability of the framework to model volume change due to the various changes in the stress condition like in the wetting and loading volume change behaviour.

In the following sections the rotation of the mobilized shear strength envelope with soil compression will be demonstrated. The existence of the required relationship of $\phi'_{\min_{mob}}$ - ε_a for the applicability of the framework will be proved from the soil behaviour in triaxial compression under both saturated and unsaturated conditions. The primary requirement is that the axial strain at failure is identical at different net confining pressures. The existence of this unique relationship of $\phi'_{\min_{mob}}$ - ε_a will also prove that the mobilized shear strength envelope is a yield surface for the condition of low stress levels, and the rotation of the yield surface due to stress changes is

representing the increase in axial strain. The volume change behaviour is quantified through the relationship between volumetric strain, ε_v, and axial strain, ε_a.

6.8.1 Interpretation of Yield Surface.

In this section the yield surface at increasing values of effective mobilized minimum friction angle, $\phi'_{\min_{mob}}$, under saturated and unsaturated conditions will be plotted to demonstrate that it is rotating about the suction axis as the soil is compressed. The critical requirement in order for the yield surface to represent identical axial strain is that the peak stress or the failure point for tests at different effective or net stresses must occur at the same axial strain in each test. This is only possible if the specimens do not exhibit particle breakage during the compression. If there is particle breakage in one of the tested specimens, it may be identified by the peak stress occurring at higher axial strain. Therefore this must be characteristic of the selected stress-strain curves required for proving that the mobilized shear strength envelope is the yield surface. The stress-strain curves that demonstrate this characteristic are for the saturated specimens compacted at 8% moisture content where results are plotted in Figure 5.15 showing that their failure points all occurred at 1% axial strain. The step by step procedure for drawing the yield surface is described in Section 3.4.7. Figure 6.18 shows the rotation of the hypothetical yield surface towards the soil shear strength envelope during the triaxial compression tests at effective stresses of 100, 200 and 300 kPa on those specimens. The parameters used to plot the Mohr circles and the yield surface corresponding to effective mobilized minimum friction angles of 10, 20, 30 and 34 degrees are listed in Table 6.4 and 6.5 respectively. The yield surfaces are drawn using Equations 3.13 and 3.14. Figure 6.18 indicates that the Mohr stress circles correspond reasonably well with their respective yield surface. The parameters used to draw the Mohr circles and the yield surfaces are based on the corresponding calculated values of $\phi'_{\min_{mob}}$ according to Equation 3.34.

6.8.2 Unique Relationship Between $\phi'_{\min_{mob}}$ and ε_a.

Each yield surface plotted in Figure 6.18 must be representing identical axial strain for it to be valid as a yield surface. The position of the yield surfaces is noted by the mobilized minimum friction angles (i.e. $\phi'_{\min_{mob}}$) which are 10°, 20°, 30° and 34°. As the yield surface rotates anti-clockwise about the suction axis, which is perpendicular to the page and passes through the origin, towards the soil shear strength envelope, where $\phi'_{\min_{mob}} = \phi'_{\min_f} = 34°$, the axial strain is increasing towards the common axial strain at failure irrespective of the different effective stresses. Therefore if each yield surface is representing identical axial strain then the graph of $\phi'_{\min_{mob}} - \varepsilon_a$ must be unique irrespective of the effective stress. Figure 6.19 shows the graphs of effective mobilized friction angle, $\phi'_{\min_{mob}}$, (i.e. maximum effective mobilized friction angle) versus axial strain, ε_a, and it indicates that the effective mobilized friction angle at failure, ϕ'_{mob_f}, decreases as effective stress increases and the values are shown in Table 6.4. This evidence supports the non-linear shape of the envelope at low stress levels. Figure 6.20 shows the corresponding plot of $\phi'_{\min_{mob}}$ - ε_a for triaxial tests on saturated specimens compacted at 8% moisture content at effective stresses of 100, 200 and 300 kPa. It shows that the graph of $\phi'_{\min_{mob}}$ - ε_a is unique with the plots almost overlapping each other even though they represent different effective stresses. This overlapping proves that each yield surface in Figure 6.18 is representing the same axial strain. The small positive values of $\phi'_{\min_{mob}}$ up to 10° and the negative values in Figure 6.20 need to be omitted as described in Section 3.3.4. The latter occurs when $\left(\phi'_{mob_f} - \phi'_{mob}\right)$ is greater than $\phi'_{\min_f}$ in Equation 3.34.

Furthermore, it can be noticed that from mobilized minimum friction angle of 30° to 34° in Figure 6.20 that there is a significant increase in the axial strain. This may not be realistic in the field. Figure 5.21 shows the corresponding graphs of volumetric strain versus axial strain and it can be seen that the rate of change in volumetric strain is decreasing for this range of axial strain. The significant increase in axial strain corresponding to the small decrease in the volumetric strain is implying that the

specimen is dilating. This is because the significant increase in axial strain should produce a corresponding significant decrease in the volumetric strain if the specimen is contracting. Since soil dilation is not occurring in the field for the case of 1-D compression the significant increase in axial strain between effective mobilized minimum friction angles of 30° to 34° is not representing the field volume change behaviour. Therefore the field volume change behaviour is only reflected by the linear section of the stress-strain curve.

6.8.3 Influence of Particle Breakage on the Applicability of the Framework.

This section will consider the effect of variation of the $\phi'_{\min_{mob}} - \varepsilon_a$ graphs when the axial strain at failure varies for tests at different net confining stress. This effect is the result of particle breakage during shearing which increases the axial strain at failure (Bishop 1966, 1972 and Billam 1972). When the graphs of $\phi'_{\min_{mob}} - \varepsilon_a$ at different net confining stresses do not overlap this implies that a single value of effective mobilized minimum friction angle, $\phi'_{\min_{mob}}$, is representing different axial strains at different net confining stresses. In this case the mobilized shear strength envelope cannot be regarded as a yield surface as particle breakage is invalidating the application of the mobilized shear strength envelope as a yield surface.

The graphs of deviator stress versus axial strain for triaxial tests on saturated and unsaturated specimens that exhibit failure at different axial strains chosen in this exercise confirm that particle breakage negates the unique relationship of $\phi'_{\min_{mob}} - \varepsilon_a$ for different net confining stresses. Four types of compacted triaxial specimens that exhibit failure at different axial strains during shear were chosen. They are the saturated specimens compacted at 4% and 6% moisture content and the unsaturated specimens of suctions 25 and 50 kPa. Their stress-strain curves are presented in Figures 5.13, 5.14, 5.33 and 5.34 respectively. For the multistage triaxial tests on unsaturated specimens the zero axial strain is taken at the initial condition of the respective shearing stage. The corresponding mobilized shear strength envelopes at effective mobilized minimum friction angles of 10°, 20°, 30° and 34° are shown in Figures 6.21- 6.24 respectively. The parameters used to plot the Mohr circles and the corresponding mobilized shear strength envelopes or the hypothetical yield surfaces

are shown in Tables 6.6 – 6.13 respectively. These mobilized shear strength envelopes can be regarded as the yield surfaces provided they show a unique relationship of $\phi'_{\min_{mob}} - \varepsilon_a$. The corresponding graphs of $\phi'_{mob} - \varepsilon_a$ and $\phi'_{\min_{mob}} - \varepsilon_a$ are shown consecutively in Figures 6.25 – 6.32 respectively. The graphs of $\phi'_{\min_{mob}} - \varepsilon_a$ in Figures 6.26, 6.28, 6.30 and 6.32 indicate a slight dispersion from overlapping before arriving at the maximum value of the effective mobilized minimum friction angle of 34°. The axial strains at failure are shown in Tables 6.6, 6.8, 6.10 and 6.12 and the variability of the axial strains at failure for the graphs of $\phi'_{\min_{mob}} - \varepsilon_a$ in Figures 6.26, 6.28, 6.30 and 6.32 are 31.0%, 30.8%, 24.5% and 16.1% respectively. These percentages of variability of axial strain at failure are small compared to those of coarse-grained soils when sheared at higher net confining pressures. For example the variability of axial strain at failure due to particle breakage (Bishop, 1966 and 1972 ; Billam, 1972) at higher net confining pressure is 68.8% between net confining pressures of 100 kPa and 600 kPa for stress-strain curves of greywacke rockfill in Figure 2.12(a) (Indraratna *et al.*, 1993) and 81.8% between net confining pressures of 100 kPa and 800 kPa for stress-strain curves of gneiss rock residual soil in Figure 2.15(a) (Futai and Almeida, 2005). Therefore this is implying that failure at higher axial strain will cause a greater dispersion of the graphs of $\phi'_{\min_{mob}} - \varepsilon_a$ and if this is the case then the mobilized shear strength envelope would not represent the same axial strain and thus cannot be regarded as a yield surface. Nevertheless the graphs of $\phi'_{\min_{mob}} - \varepsilon_a$ shown in Figures 6.26, 6.28, 6.30 and 6.32 can still be considered to reasonably unique despite the slight dispersion considering the soil heterogeneity. Therefore the mobilized shear strength envelopes shown in Figures 6.21 – 6.24 can still be regarded as yield surfaces within tolerable limits.

Since particle breakage will cause the dispersion of the $\phi'_{\min_{mob}} - \varepsilon_a$ graph and invalidates the representation of the mobilized shear strength envelope as the yield surface therefore the applicability of the proposed framework on the test material is limited to cases of low (< 300 kPa) stress levels only.

6.8.4 Framework Prediction of the Stress-Strain Curve from a Triaxial Compression Test.

If the unique relationship of $\phi'_{\min_{mob}} - \varepsilon_a$ and the shear strength envelope at failure are derived from the soil stress-strain behaviour, then conversely the stress-strain curve can be deduced from knowing the soil characteristics. In this section the Rotational Multiple Yield Surface Framework demonstrates its ability to predict the stress-strain curves for the triaxial tests on saturated specimens compacted at 8% and 6% moisture content sheared at effective stresses of 100, 200 and 300 kPa. The same prediction was also conducted for the unsaturated specimens sheared at a suction of 25 kPa. The procedure is as discussed in Section 3.4.8 and it involved the reverse of the process for obtaining the yield surfaces as described in Section 3.4.7.

The step by step procedure for the prediction of the stress-strain curves is as follows.

1. Obtain the shear strength envelope at failure of the test material as described in Section 6.7.3.
2. Obtain the $\phi'_{\min_{mob}} - \varepsilon_a$ relationship. This is performed by drawing the best fit curve that passes through the origin among the curves of $\phi'_{\min_{mob}} - \varepsilon_a$ for effective or net stresses of 100, 200 and 300 kPa (refer Figure 6.20, 6.26 and 6.30) for saturated specimens compacted at 8% and 6% moisture content and the unsaturated specimens at a suction of 25 kPa respectively. The curve obtained is shown in Figures 6.33, 6.38 and 6.43 and the values of ε_a and $\phi'_{\min_{mob}}$ used to plot the curve are tabulated in Tables 6.14, 6.16 and 6.18 respectively.
3. Select the values of $\phi'_{\min_{mob}}$ and the corresponding ε_a from the deduced $\phi'_{\min_{mob}} - \varepsilon_a$ relationship. The selected values of $\phi'_{\min_{mob}}$ are 10°, 20°, 30°, 31°, 32°, 33° and 34° and the corresponding ε_a% are as shown in Tables 6.14, 6.16 and 6.18 respectively.
4. Determine the yield surfaces. The parameters that describe them are shown in Tables 6.5, 6.9 and 6.11 respectively. The yield surfaces for $\phi'_{\min_{mob}}$ of 10°, 20°, 30°, 31°, 32°, 33° and 34° are drawn in Figures 6.34 – 6.36, 6.39 – 6.41

and 6.44 – 6.46 respectively. The axial strains represented by the yield surfaces are shown in Tables 6.14, 6.16 and 6.18 respectively as in step 3.

5. Predict the stress-strain curves for the shearing of the saturated specimens compacted at 8% and 6% moisture content at effective pressures of 100, 200 and 300 kPa and 100, 199 and 245 kPa respectively. For the unsaturated specimens with a suction of 25 kPa the stress-strain curves are to be predicted at net stresses of 100, 200 and 300 kPa.
6. Draw the predicted Mohr circles corresponding to the yield surfaces and the shear strength envelope at failure. For the saturated specimens compacted at 8% and 6% moisture content are shown in Figures 6.34 – 6.36 and 6.39 – 6.41 respectively. For the unsaturated specimen of suction 25 kPa the predicted Mohr circles are shown in Figures 6.44 – 6.46.
7. Determine the magnitudes of the net vertical stresses obtained from the Mohr stress circles are shown in Tables 6.15, 6.17 and 6.19.
8. The corresponding magnitudes of the deviator stresses, q, are shown in Tables 6.15, 6.17 and 6.19 respectively.
9. The predicted data points up to the failure point for the stress-strain behaviour are drawn superimposed on the experimental graphs in Figures 6.37, 6.42 and 6.47 respectively.

The experimental graphs and the data points predicted by the Rotational Multiple Yield Surface Framework shown are in Figure 6.37, 6.42 and 6.47 showed a close correlation. This demonstrates the capability of the hypothetical framework to predict the stress-strain curve at any net confining pressure. However an exact prediction cannot be achieved when the assumed unique relationship of $\phi'_{\min_{mon}} - \varepsilon_a$ used in the prediction does not exactly overlap the graph at the considered net confining stress. A slight dispersion in the graph of $\phi'_{\min_{mon}} - \varepsilon_a$ would affect the prediction of the stress-strain curve. Section 6.8.3 has demonstrated that the dispersion in the graph occurs when the axial strain at failure varies and this is caused by particle breakage during shearing which increases the axial strain at failure. The result of this prediction therefore confirmed that the occurrence of particle breakage is the limit of the application of the proposed hypothetical shear strength-volume change framework.

6.8.5 Volume Change Behaviour under Loading and Wetting Collapse from Rowe Cell Compression Tests.

This section discusses the results of test series E described in Section 5.5.4. One test was carried out for saturated conditions and the other two unsaturated tests were carried out at suctions of 25 and 50 kPa. Volume change behaviour due to wetting and loading collapse under 1-D compression will be discussed. These volume changes cannot be interpreted using the proposed Rotational Multiple Yield Surface Framework since the lateral pressure was not measured in the tests and it would be very difficult to estimate the values of the lateral pressure at every stage of the compression since the coefficient of earth pressure at rest, K_o, varies with density (Ting *et al.*, 1994).

The plots of void ratio versus net stress for the two Rowe cell compression tests on unsaturated specimens and void ratio versus effective stress for the saturated specimen are superimposed in Figure 6.48. The plots show linear behaviour between net stress and void ratio for the unsaturated specimens and linear behaviour between effective stress and void ratio for the saturated specimen. This linear behaviour is in accordance with earlier reports by Cox (1978), Brandon *et al.* (1990) and Villar (1995). The steeper graph for compression under suction of 50 kPa compared to suction of 25 kPa is as expected, since the former has lower shear strength to resist deformation as interpreted in Section 6.7. Due to the lower shear strength to resist the applied load, the rate of soil compression with respect to net normal stress will be greater.

Similarly the same linear behaviour between net normal stress and axial strain for unsaturated specimens and between effective stress and axial strain for the saturated specimen are superimposed in Figure 6.49. The volume change behaviour in the unsaturated specimens is categorised as loading collapse since the specimen compression is due to the incremental load. However the volume change behaviour in the test on the saturated specimen can be interpreted either as loading or wetting collapse. The line OC in the plot for the saturated specimen is representing wetting collapse when the initially oven dried soil was inundated and subsequently an effective stress of 50 kPa was applied. Initially when the specimen was inundated under zero net normal stress the specimen did not exhibit any collapse behaviour

since no reduction in the specimen height was noticed. Therefore when a net normal stress of 50 kPa was applied then there was a significant increase in the axial strain to indicate the wetting collapse volume change. Perhaps if the specimen had not been inundated the plot of net normal stress versus axial strain would be represented by the dotted line OM which is parallel to the section CD of the graph for the compression of the saturated specimen. The axial strain corresponding to point A on the dotted line would represent the axial strain of the oven dried specimen when a net vertical stress of 100 kPa was applied without the specimen being inundated. The percentage axial strain representing by AB would be the subsequent wetting collapse if the specimen was inundated after the application of the 100 kPa net normal stress. The axial strain represented by the horizontal distances EF, GH, IJ, KL and MD would be due to the wetting collapse if the specimen was inundated after the application of the net normal stresses of 200, 300, 400, 500 and 600 kPa respectively. This is similar to the graphs in Figure 2.17 reported by Goodwin (1991), which is showing the effect of inundation under the application of the net normal stress. The axial strains represented by BF, FH, HJ, JL and LD are the soil compressions due to loading collapse under saturated conditions when the net vertical stress was increased in steps of 100 kPa from an initial value of 100 kPa. Therefore soil volume change behaviour in the Rowe cell compression test on the saturated specimen can be interpreted in the both ways, i.e. either wetting or loading collapse.

The features exhibited during these tests are in accordance with some of the proposed hypothetical framework general characteristics underlined in Section 3.4.1 and some of the features are not covered in the tests.

1. The characteristic of plastic deformation as characteristic no. 1 was noted when there was no rebound of the specimen when the maximum applied net vertical stress was removed at the end of the tests.
2. The characteristic no. 2 was noted when increase in the net vertical stress or inundation under constant net vertical stress caused the soil to compress. Therefore the change in the stress conditions is driving the stress state to exceed the yield limit.
3. The soil compression under an increment of net vertical stress after the compression stops before the next increment is applied is implying the involvement of the multiple yield surface in the compression.

4. The demonstration of the concept of stress equilibrium that governs the soil compression was noted when the compression was triggered upon the increase in the net vertical stress or when the soil was inundated. These types of stress changes are driving the Mohr stress circles to extend above the current yield surface or the current mobilized shear strength envelope, according to the Rotational Multiple Yield Surface Framework described in Section 3.4.4 and 3.4.5.
5. Characteristic no. 6, which is a massive volume decrease near saturation was noted when significant volume change happened in the compression test on the Rowe cell loose specimen which was inundated prior to loading.
6. However characteristic no. 7 which is immediate settlement in coarse-grained soil was not noted when incremental load was applied due to the significant time taken to overcome the friction between top platen and the cell wall .

The above features encountered during the Rowe cell compression tests on coarse-grained soils support the concept applied in the proposed Rotational Multiple Yield Surface Framework. If lateral pressure was monitored during the 1-D compression test then the volume change behaviour could be interpreted according to the proposed framework, and this is recommended for further research.

Table 6.1 Previous strain rates that have been applied by researchers in shearing of coarse grain unsaturated specimens.

No.	Soil type	Type of triaxial test	Strain rate (mm/min)	Author
1	Limestone gravel	CD CW	0.0004 0.0035	Salman, 1995
2	Silty soil	CW	0.014	Nishimura and Fredlund, 2000
3	Granite residual soil	CD CW	0.00166 0.00666	Taha *et al.*, 2000
4	Granite residual soil	CD CW	0.03375	Toll *et al.*, 2000
5	Granite residual soil	CD	0.0009	Wong *et al.*, 2000

Note: CD – consolidated drained and CW – constant water content.

Table 6.2 Apparent and total shear strength at respective suctions and net stresses obtained from unsaturated triaxial tests.

Suction (kPa)	Net Stress (kPa)	Apparent Shear Strength (kPa)	Assuming negative apparent shear strength equals Zero kPa	Saturated shear strength (kPa)	Total shear strength (kPa)
0	100	0	0	138.8	138.8
25	100	17	17	138.8	155.8
50	100	17	17	138.8	155.8
60	100	-10	0	138.8	138.8
90	100	-10	0	138.8	138.8
0	200	0	0	230.0	230.0
25	200	30	30	230.0	260.0
50	200	18	18	230.0	248.0
60	200	-9	0	230.0	230.0
90	200	-5	0	230.0	230.0
0	300	0	0	284.9	284.9
25	300	26	26	284.9	310.9
50	300	9	9	284.9	293.9
60	300	7	7	284.9	291.9
90	300	-9	0	284.9	284.9

Table 6.3 The seven shear strength parameters of the test material according to the warped-surface extended Mohr-Coulomb envelope.

No.	Name of parameter	Symbol	Value
1	Maximum apparent shear strength	c_s^{max}	30kPa
2	Residual suction	$(u_a - u_w)_r$	15kPa
3	Transition effective stress	$(\sigma - u_w)_t$	200kPa
4	Transition shear strength	τ_t	230kPa
5	Effective minimum friction angle at failure	ϕ'_{min_f}	34°
6	Rate of increase in ultimate suction with respect to net stress	ζ	0.05
7	Ultimate suction at zero net stress	$(u_a - u_w)_u^{\sigma'=0}$	50kPa

Table 6.4 Parameters used to plot the Mohr circles corresponding to $\phi'_{min_{mob}}$ of 10, 20, 30 and 34 degrees for saturated triaxial specimens compacted at 8% moisture content shown in Figure 6.18.

Test code	S8%SSES100			S8%SSES200			S8%SSES300		
Effective stress (kPa)	100			200			300		
Cell pressure (kPa)	590			589			690		
Back pressure (kPa)	490			390			390		
ϕ'_{mob_f}	47.7			43.4			39.7		
$\%\varepsilon_a$ at failure	1.0%			1.0%			1.0%		
$\phi'_{min_{mob}}$	ϕ'_{mob}	q	σ'_1	ϕ'_{mob}	q	σ'_1	ϕ'_{mob}	q	σ'_1
10°	23.8	140.0	243.2	19.4	197.3	395.1	15.7	223.8	524.3
20°	33.8	257.1	359.5	29.4	381.3	578.6	25.7	457.5	756.2
30°	43.8	461.1	563.5	39.4	684.2	881.1	35.7	857.4	1163.3
$\phi'_{min_f} = 34°$	47.7	600.0	705.4	43.4	871.0	1064.8	39.7	1074.0	1376.1

Table 6.5 Parameters used to plot the yield surfaces using Equation 3.13 and 3.14 for saturated triaxial specimens compacted at 8% moisture content shown in Figures 6.18, 6.34, 6.35 and 6.36.

Test code	S8%SSES100, S8%SSES200 and S8%SSES300		
$\phi'_{\min_{mob}}$	$(\sigma - u_w)_t$	τ_t	N
10°	200	80	1.788
20°	200	130	2.272
30°	200	195	2.452
31°	200	204	2.43
32°	200	213	2.42
33°	200	222	2.41
$\phi'_{\min_f} = 34°$	200	230	2.419

Table 6.6 Parameters used to plot the Mohr circles corresponding to $\phi'_{\min_{mob}}$ of 10, 20, 30 and 34 degrees for saturated triaxial specimens compacted at 4% moisture content shown in Figure 6.18.

Test code	S4%SSES100			S4%SSES200			S4%SSES300		
Effective stress (kPa)	100			200			300		
Cell pressure (kPa)	640			540			640		
Back pressure (kPa)	540			340			340		
ϕ'_{mob_f}	46.8			41.8			37.2		
$\%\varepsilon_a$ at failure	0.69			0.76			1.0		
$\phi'_{\min_{mob}}$	ϕ'_{mob}	q	σ'_1	ϕ'_{mob}	q	σ'_1	ϕ'_{mob}	q	σ'_1
10°	22.8	130.7	234.0	17.9	180.3	384.2	13.2	177.8	477.4
20°	32.9	243.2	345.6	27.8	355.3	558.5	23.2	388.7	687.6
30°	42.8	432.8	534.9	37.8	642.6	845.4	33.2	723.1	1021.6
$\phi'_{\min_f} = 34°$	46.8	563.0	658.1	41.8	813.0	1019.1	37.2	915.0	1214.5

Table 6.7 Parameters used to plot the yield surfaces using Equation 3.13 and 3.14 for saturated triaxial specimens compacted at 4% moisture content shown in Figure 6.21.

Test code	S4%SSES100, S4%SSES200 and S4%SSES300		
$\phi'_{\min_{mob}}$	$(\sigma - u_w)_f$	τ_f	N
10°	200	80	1.788
20°	200	130	2.272
30°	200	195	2.452
$\phi'_{\min_f} = 34°$	200	220	2.585

Table 6.8 Parameters used to plot the Mohr circles corresponding to $\phi'_{\min_{mob}}$ of 10, 20, 30 and 34 degrees for saturated triaxial specimens compacted at 6% moisture content shown in Figure 6.22.

Test code	S6%SSES100			S6%SSES200			S6%SSES300		
Effective stress (kPa)	100			200			250		
Cell pressure (kPa)	590			690			640		
Back pressure (kPa)	490			490			390		
ϕ'_{mob_f}	48.2			43.3			41.9		
$\%\varepsilon_a$ at failure	0.91			0.63			0.72		
$\phi'_{\min_{mob}}$	ϕ'_{mob}	q	σ'_1	ϕ'_{mob}	q	σ'_1	ϕ'_{mob}	q	σ'_1
10°	24.2	142.7	245.3	19.3	197.2	396.2	17.9	225.6	478.9
20°	34.2	263.1	365.6	29.3	381.2	579.8	27.9	439.3	687.5
30°	44.2	470.6	572.8	39.3	685.1	883.3	37.9	793.1	1042.0
$\phi'_{\min_f} = 34°$	48.2	614.0	720.1	43.3	867.0	1070.3	41.9	1008.0	1261.1

Table 6.9 Parameters used to plot the yield surfaces using Equation 3.13 and 3.14 for saturated triaxial specimens compacted at 6% moisture content shown in Figures 6.22, 6.39, 6.40 and 6.41.

Test code	S6%SSES100, S6%SSES200 and S6%SSES250		
$\phi'_{\min_{mob}}$	$(\sigma - u_w)_f$	τ_f	N
10°	200	85	1.709
20°	200	135	2.170
30°	200	200	2.366
31°	200	206	2.400
32°	200	213	2.420
33°	200	222	2.410
$\phi'_{\min_f} = 34°$	200	232	2.389

Table 6.10 Parameters used to plot the Mohr circles corresponding to $\phi'_{\min_{mob}}$ of 10, 20, 30 and 34 degrees for unsaturated triaxial specimens of suction 25 kPa shown in Figure 6.23.

Test code	USSuc25NS100			USSuc25NS200			USSuc25NS300		
Net stress (kPa)	100			200			300		
Cell pressure (kPa)	190			290			390		
Pore air pressure (kPa)	90			90			90		
Pore water pressure (kPa)	65			65			65		
ϕ'_{mob_f}	50.3			44.8			42.0		
$\%\varepsilon_a$ at failure	0.49			0.37			0.37		
$\phi'_{\min_{mob}}$	ϕ'_{mob}	q	σ'_1	ϕ'_{mob}	q	σ'_1	ϕ'_{mob}	q	σ'_1
10°	26.3	158.8	258.7	20.8	220.4	420.5	18.0	269.0	569.5
20°	36.3	289.8	389.5	30.8	421.2	621.4	28.0	530.7	830.7
30°	46.3	520.0	619.6	40.8	753.4	953.2	38.0	960.1	1260.0
$\phi'_{\min_f} = 34°$	50.3	672.0	763.8	44.8	955.0	1155.1	42.0	1209.0	1507.4

Table 6.11 Parameters used to plot the mobilized shear strength envelopes using Equation 3.13 and 3.14 for unsaturated triaxial specimens of suction 25 kPa shown in Figures 6.23, 6.44, 6.45 and 6.46.

Test code	USSuc25NS100, USSuc25NS200 and USSuc25NS300		
$\phi^{'}_{\min_{mob}}$	$(\sigma - u_w)_t$	τ_t	N
10°	200	70	2.015
20°	200	125	2.394
30°	200	195	2.452
31°	200	204	2.433
32°	200	213	2.420
33°	200	222	2.410
$\phi^{'}_{\min_f} = 34°$	200	230	2.419

Table 6.12 Parameters used to plot the Mohr circles corresponding to $\phi^{'}_{\min_{mob}}$ of 10, 20, 30 and 34 degrees for unsaturated triaxial specimens of suction 50 kPa shown in Figure 6.24

Test code	USSuc50NS100			USSuc50NS200			USSuc50NS300		
Net stress (kPa)	100			200			300		
Cell pressure (kPa)	190			290			390		
Pore air pressure (kPa)	90			90			90		
Pore water pressure (kPa)	40			40			40		
$\phi^{'}_{mob_f}$	49.9			44.4			41.1		
$\%\varepsilon_a$ at failure	0.56			0.47			0.56		
$\phi^{'}_{\min_{mob}}$	$\phi^{'}_{mob}$	q	$\sigma^{'}_1$	$\phi^{'}_{mob}$	q	$\sigma^{'}_1$	$\phi^{'}_{mob}$	q	$\sigma^{'}_1$
10°	25.9	154.2	253.4	20.4	215.0	415.7	17.1	250.0	549.0
20°	35.9	284.8	385.2	30.4	411.6	612.1	27.1	500.7	799.0
30°	45.9	503.9	602.8	40.4	740.1	940.7	37.1	906.5	1204.4
$\phi^{'}_{\min_f} = 34°$	49.9	670.0	762.9	44.4	924.0	1137.9	41.1	1142.0	1434.8

Table 6.13 Parameters used to plot the mobilized shear strength envelope corresponding to $\phi'_{min_{mob}}$ of 10, 20, 30 and 34 degrees using Equation 3.13 and 3.14 for unsaturated triaxial specimens of suction 50 kPa shown in Figure 6.24.

Test code	USSuc50NS100, USSuc50NS200 and USSuc50NS300		
$\phi'_{min_{mob}}$	$(\sigma - u_w)_f$	τ_f	N
10°	200	90	1.644
20°	200	145	2.008
30°	200	210	2.222
$\phi'_{min_f} = 34°$	200	250	2.172

Table 6.14 The deduced values for the unique relationship of $\phi'_{min_{mob}}$ - ε_a for triaxial tests on saturated specimens compacted at 8% moisture content plotted in Figure 6.33.

$\%\varepsilon_a$	$\phi'_{min_{mob}}$
0	0
0.08	10.0
0.10	12.0
0.20	20.0
0.30	25.5
0.40	29.0
0.43	30.0
0.48	31.0
0.50	31.4
0.54	32.0
0.60	32.7
0.65	33.0
0.70	33.2
0.80	33.7
0.90	33.8
1.00	34.0

Table 6.15 The predicted major principal stresses and the deviator stresses corresponding to the yield surfaces and the represented axial strain during triaxial tests on saturated specimens compacted at 8% moisture content at effective stresses of 100, 200 and 300 kPa.

Targeted effective stress (kPa)		100		200		300	
σ_3 (kPa)		591		589		690	
u_w (kPa)		487		390		388	
$\phi'_{min_{mob}}$ (deg)	$\%\varepsilon_a$	σ'_1 (kPa)	Dev.stress q (kPa)	σ'_1 (kPa)	Dev.stress q (kPa)	σ'_1 (kPa)	Dev.stress q (kPa)
0	0	0	0	0	0	0	0
10	0.08	239	135	385	186	532	230
20	0.20	359	255	564	365	772	470
30	0.43	567	463	859	660	1162	860
31	0.48	599	495	904	705	1222	920
32	0.54	638	534	949	750	1282	980
33	0.65	677	573	1004	805	1352	1050
34	1.00	707	603	1054	855	1402	1100

Table 6.16 The deduced values for the unique relationship of $\phi'_{min_{mob}}$ - ε_a for triaxial tests on saturated specimens compacted at 6% moisture content plotted in Figure 6.38.

ε_a (%)	$\phi'_{min_{mob}}$ (deg)
0	0
0.08	9
0.088	10
0.1	11
0.2	19
0.215	20
0.3	25
0.4	29.3
0.422	30
0.43	30.3
0.457	31
0.476	31.55
0.495	32
0.533	32.8
0.545	33
0.595	33.5
0.65	33.7
0.695	33.9
0.73	34

Table 6.17 The predicted major principal stresses and the deviator stresses corresponding to the yield surfaces and the represented axial strain during triaxial tests on saturated specimens compacted at 6% moisture content at effective stresses of 105, 199 and 245 kPa.

Targeted effective stress (kPa)		105		199		245	
σ_3 (kPa)		591		690		632	
u_w (kPa)		486		491		387	
$\phi'_{\min_{mob}}$ (deg)	$\%\varepsilon_a$	σ'_1 (kPa)	Dev.stress q (kPa)	σ'_1 (kPa)	Dev.stress q (kPa)	σ'_1 (kPa)	Dev.stress q (kPa)
0	0	0	0	0	0	0	0
10	0.088	265	160	404	205	464	219
20	0.215	388	283	583	384	675	430
30	0.422	600	495	884	685	1025	780
31	0.457	625	520	919	720	1060	815
32	0.495	650	545	954	755	1103	858
33	0.545	685	580	1004	805	1155	910
34	0.73	725	620	1059	860	1225	980

Table 6.18 The deduced values for the unique relationship of $\phi'_{\min_{mob}}$ - ε_a for triaxial tests on unsaturated specimens of suction 25 kPa plotted in Figure 6.38.

ε_a (%)	$\phi'_{\min_{mob}}$ (deg)
0	0
0.028	9
0.032	10
0.035	11
0.063	19
0.069	20
0.102	25
0.13	28
0.160	30
0.180	31
0.200	32
0.250	33
0.480	34

Table 6.19 The predicted major principal stresses and the deviator stresses corresponding to the yield surfaces and the represented axial strain during triaxial tests on unsaturated specimens of suction 25 kPa at net stresses of 100, 200 and 300 kPa.

Targeted effective stress (kPa)		100		200		300	
σ_3 (kPa)		190		290		390	
u_a (kPa)		90		90		90	
$\phi'_{\min_{mob}}$ (deg)	$\%\varepsilon_a$	$\sigma - u_a$ (kPa)	Dev.stress q (kPa)	$\sigma - u_a$ (kPa)	Dev.stress q (kPa)	$\sigma - u_a$ (kPa)	Dev.stress q (kPa)
0	0	0	0	0	0	0	0
10	0.032	285	185	430	230	573	273
20	0.069	430	330	630	430	835	535
30	0.16	665	565	960	760	1260	960
31	0.18	695	595	1008	808	1320	1020
32	0.20	730	630	1055	855	1380	1080
33	0.250	770	670	1108	908	1450	1150
34	0.480	800	700	1158	958	1508	1208

Table 6.20 Parameters used to plot the Mohr stress circles and the corresponding mobilized shear strength envelope in Figure 6.50.

Net stress $(\sigma_1 - u_a)$ (kPa)	Estimated net lateral stress $(\sigma_3 - u_a)$ (kPa)	τ_f (kPa)	$(\sigma - u_w)_f$ (kPa)	$\phi'_{\min_{mob}}$ (deg.)
100	36.4	80	200	12
200	72.8	90	200	14
300	109.2	100	200	16
400	145.6	111	200	18
500	182.0	118	200	20
600	218.4	122	200	22

Note : Net lateral stresses, $(\sigma_3 - u_a)$, are calculated using $(\sigma_3 - u_a) = k_o(\sigma_1 - u_a)$, $k_o = 1 - \sin\phi'$ (Jaky, 1948) and ϕ' of 39.5°.

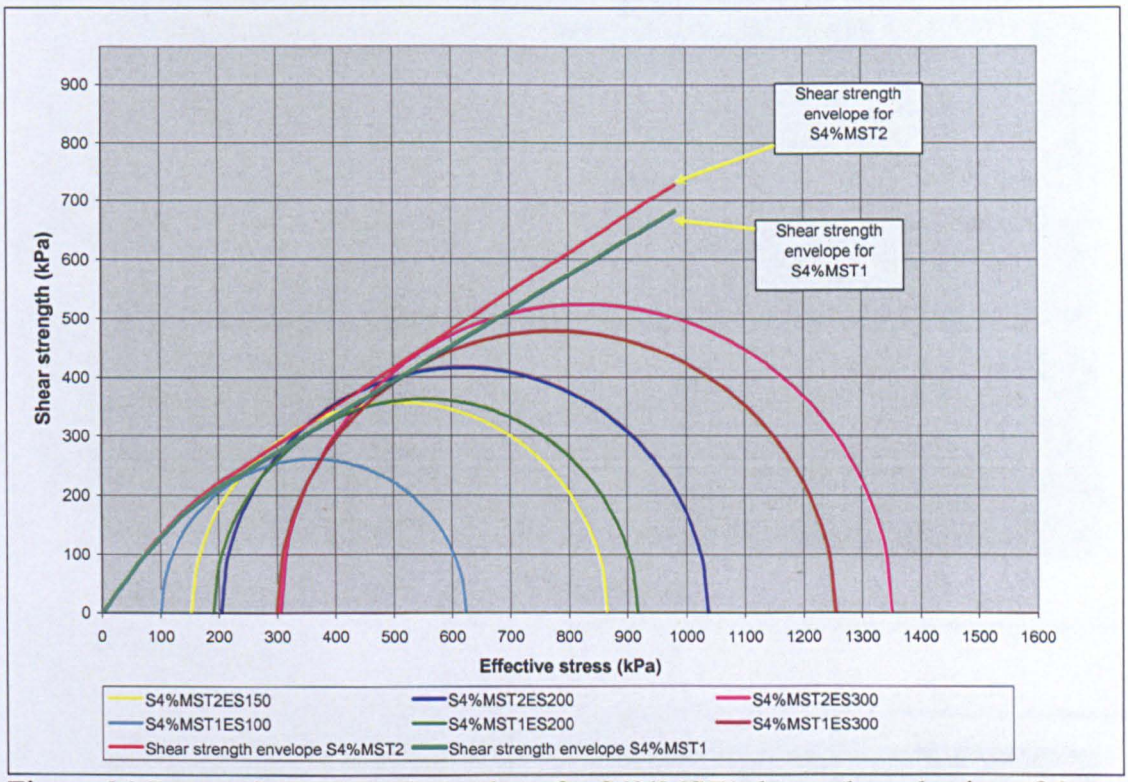

Figure 6.1 Lower shear strength envelope for S4%MST1 due to the reduction of the cell and pore water pressure by more than 150 kPa after the saturation stage.

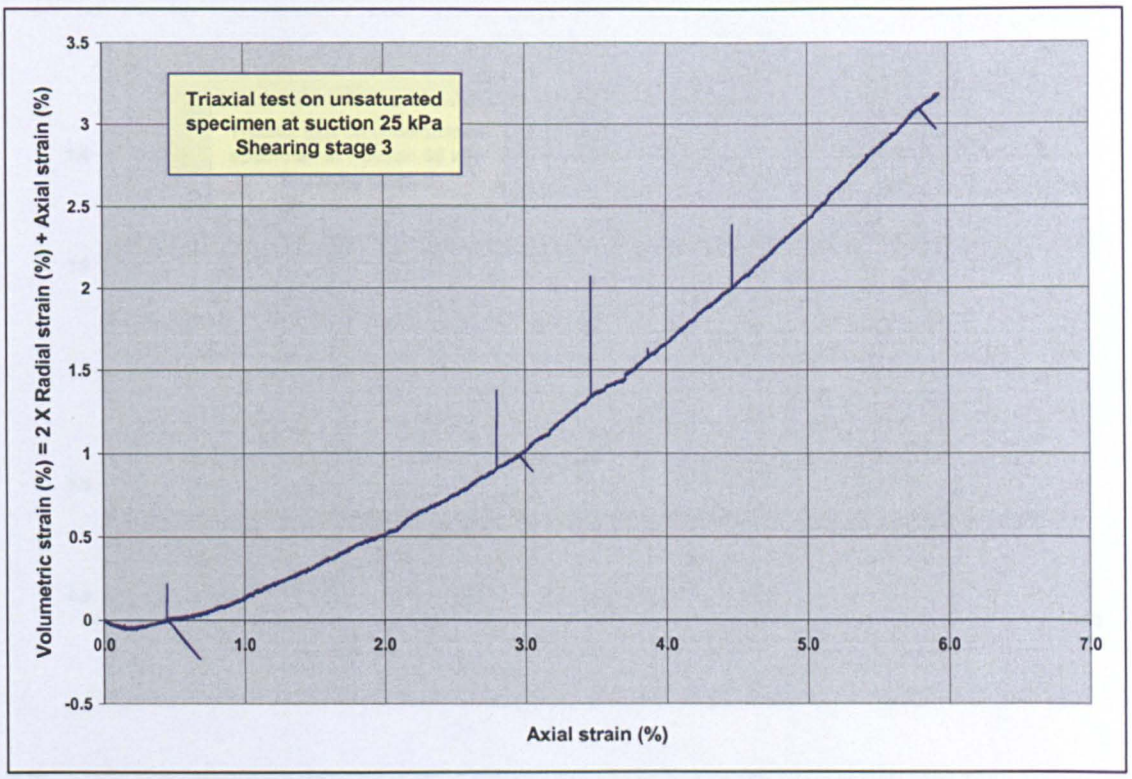

(a) Suction of 25 kPa.

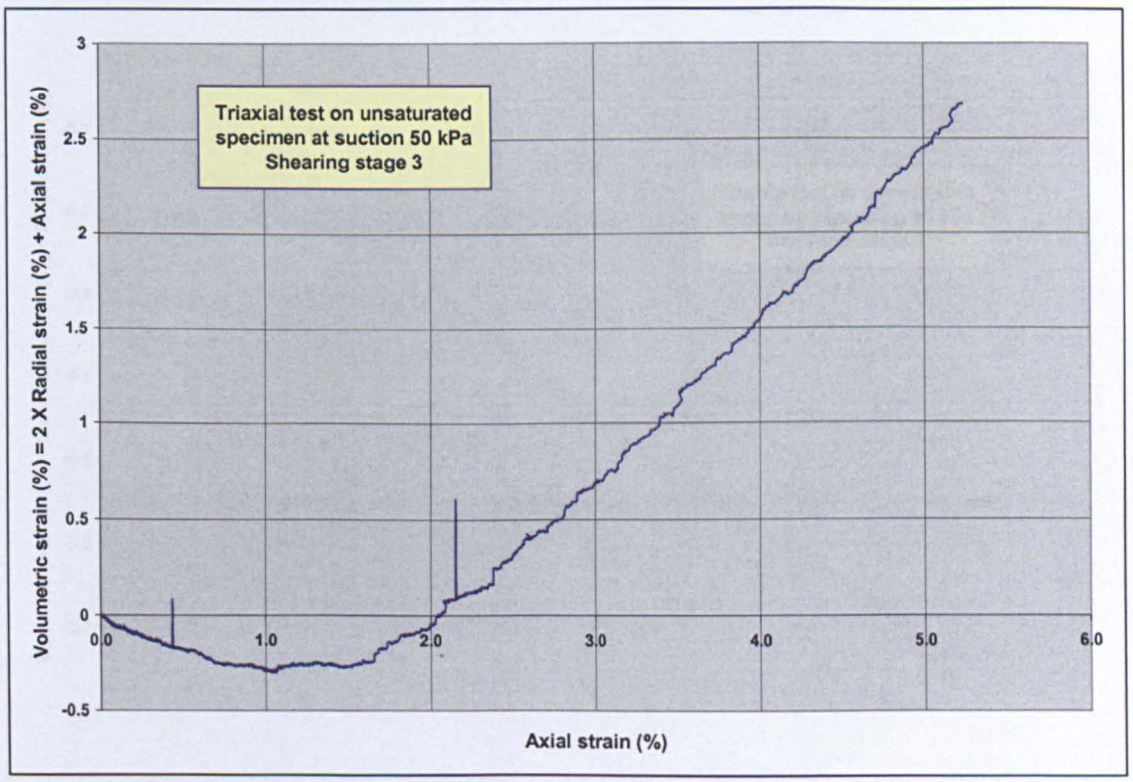

(b) Suction of 50 kPa.

Figure 6.2 Volumetric strain versus axial strain during the third shearing stage for a multistage triaxial test on an unsaturated specimen.

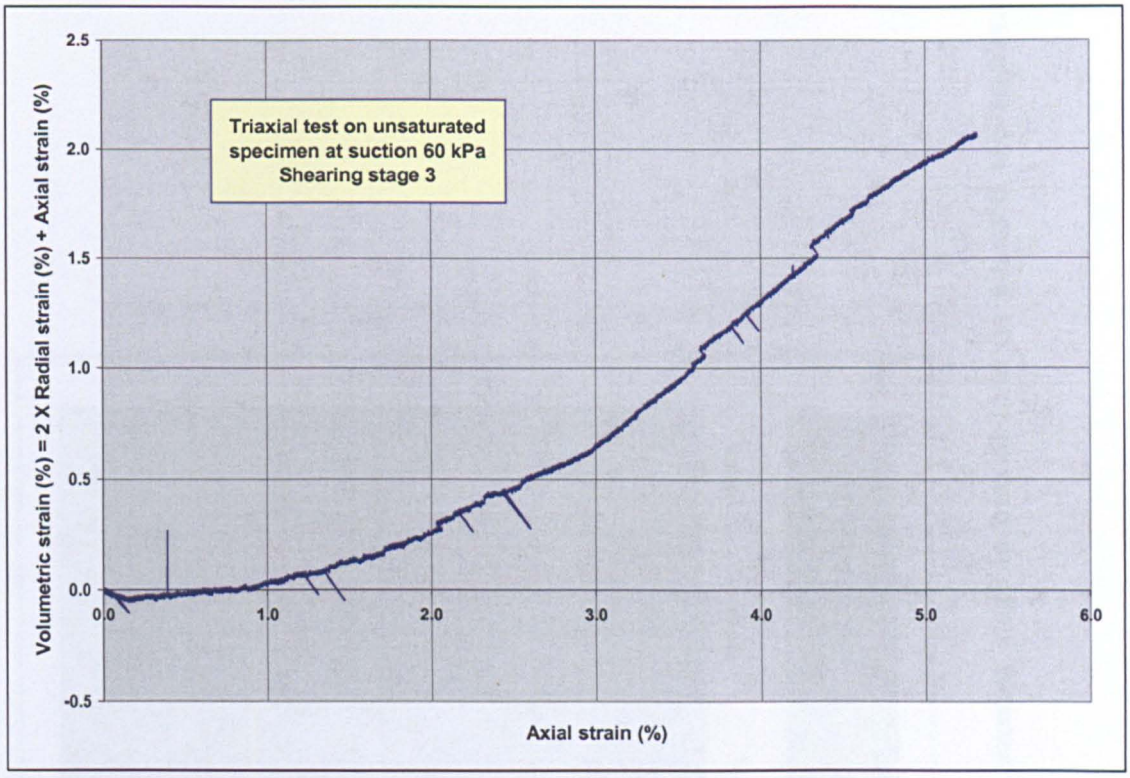

(c) Suction of 60 kPa.

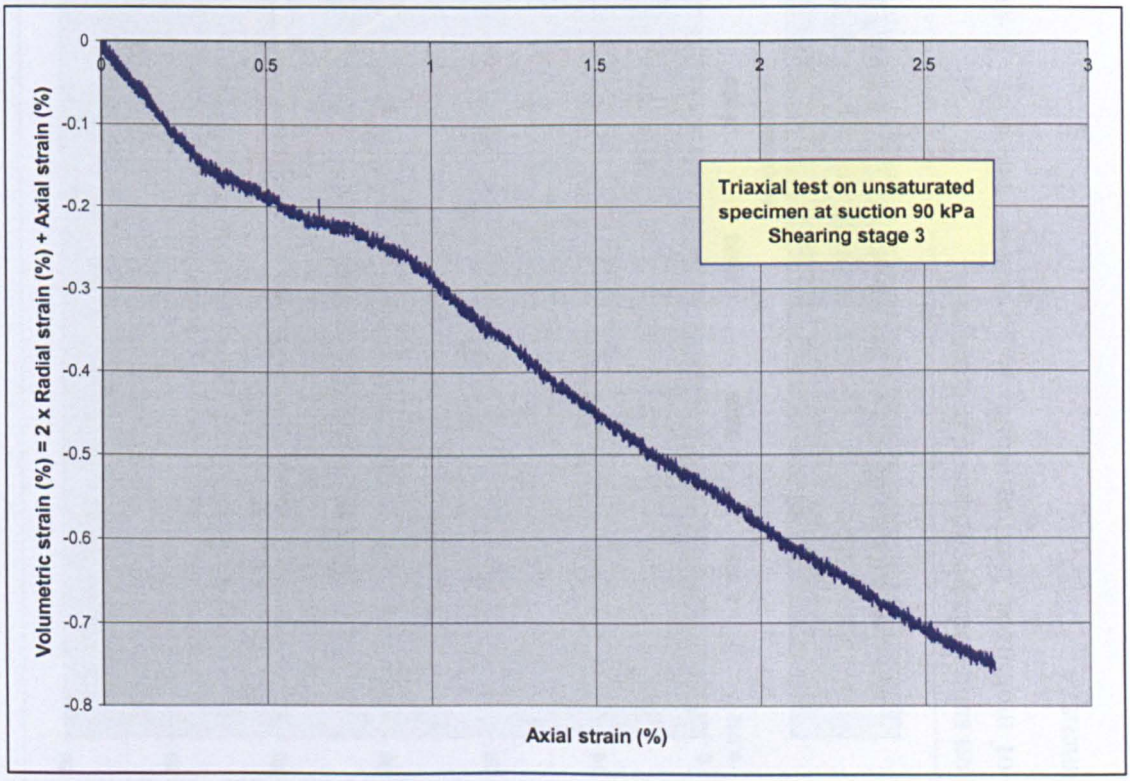

(d) Suction of 90 kPa.

Figure 6.2 (continued) Volumetric strain versus axial strain during the third shearing stage for a multistage triaxial test on an unsaturated specimen.

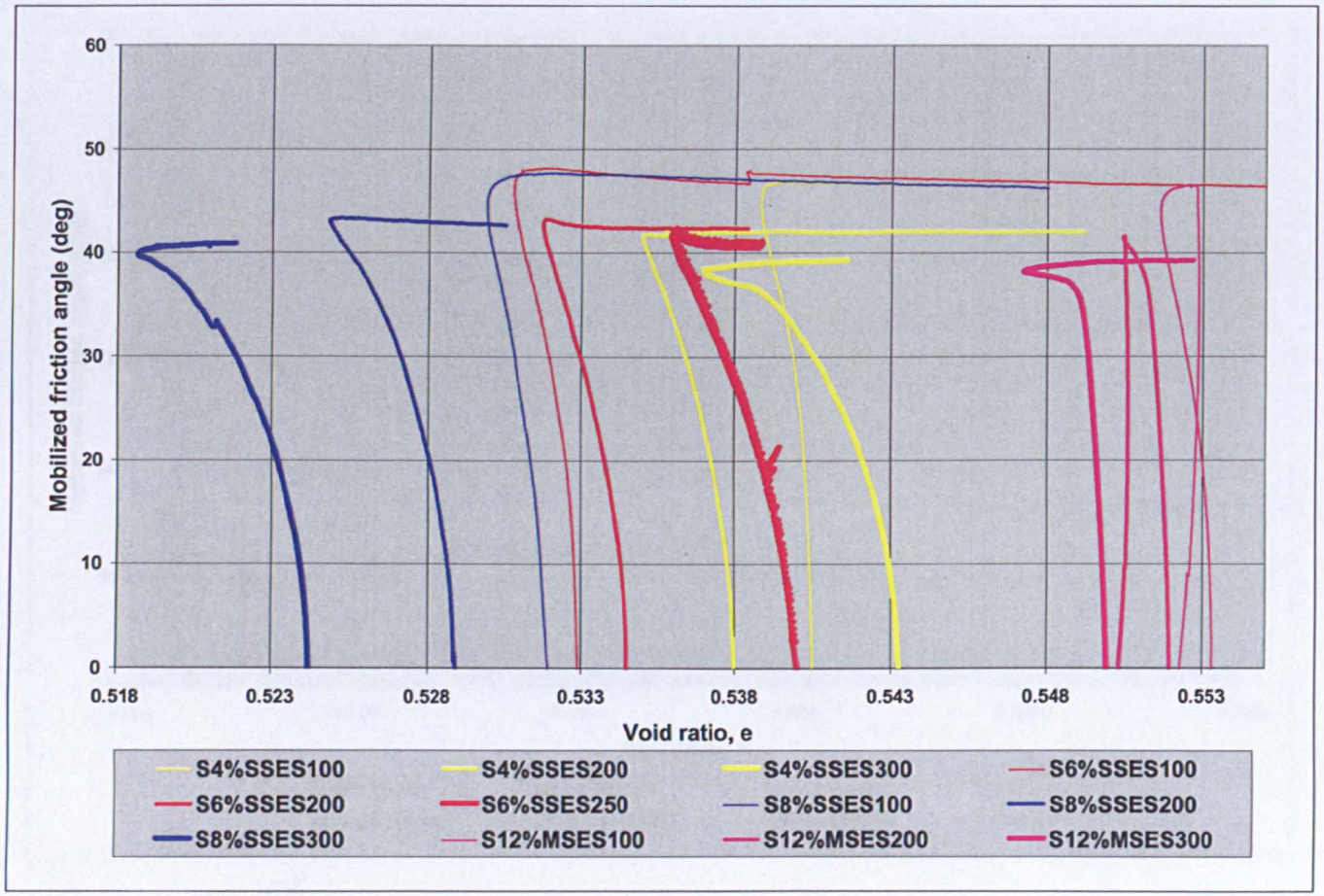

(a) Triaxial tests on saturated specimens in test series B.

Figure 6.3 Plot of mobilized friction angle, ϕ'_{mob}, versus void ratio, e, during shearing stage in triaxial tests on saturated and unsaturated specimens.

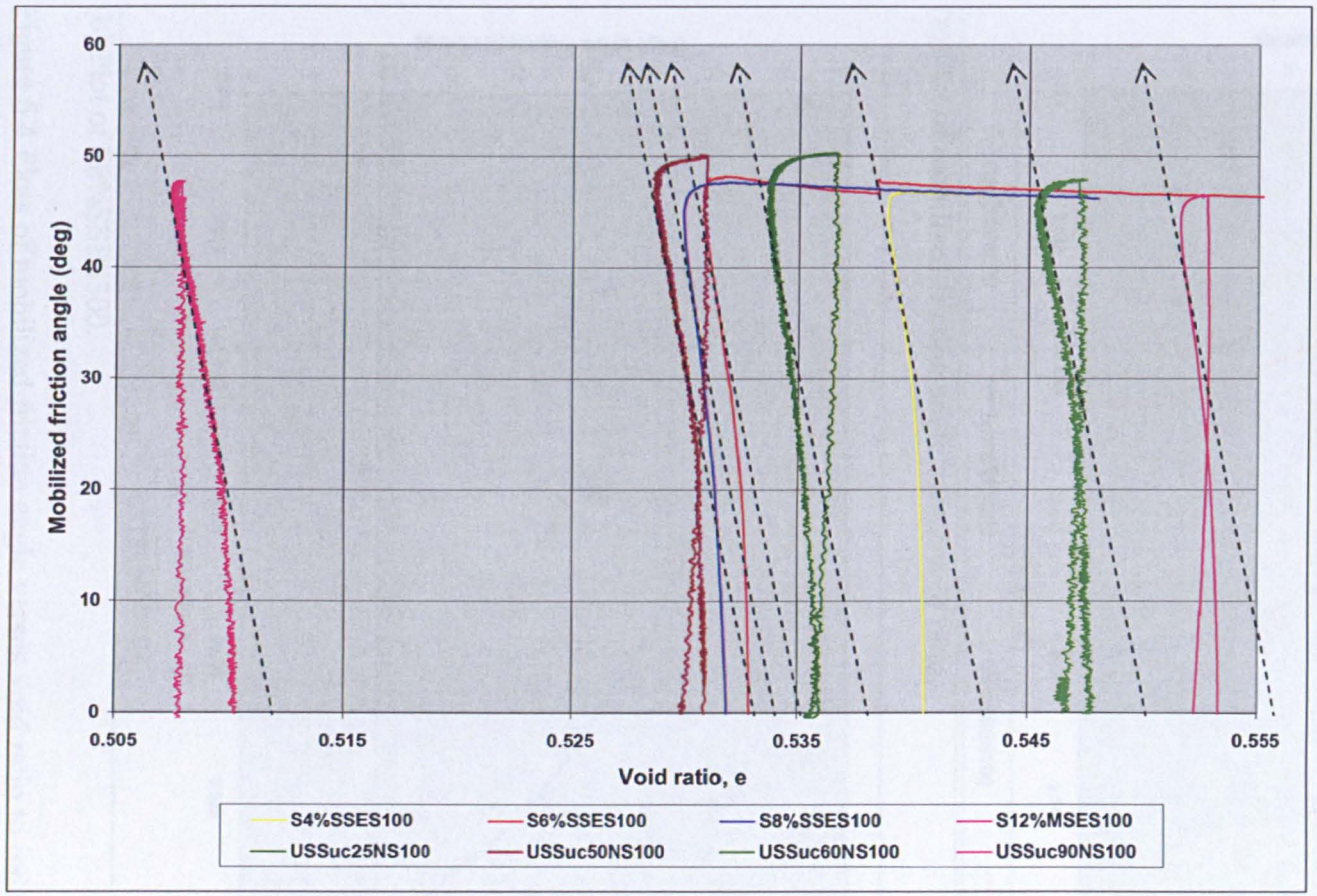

(b) Lines of identical gradient, $\frac{\Delta\phi'_{mob}}{\Delta e}$, for shearing of saturated and unsaturated triaxial test specimens at an effective or net stress of 100kPa.

Figure 6.3 (continued) Plot of mobilized friction angle, ϕ'_{mob}, versus void ratio, e during shearing stage in triaxial tests on saturated and unsaturated specimens.

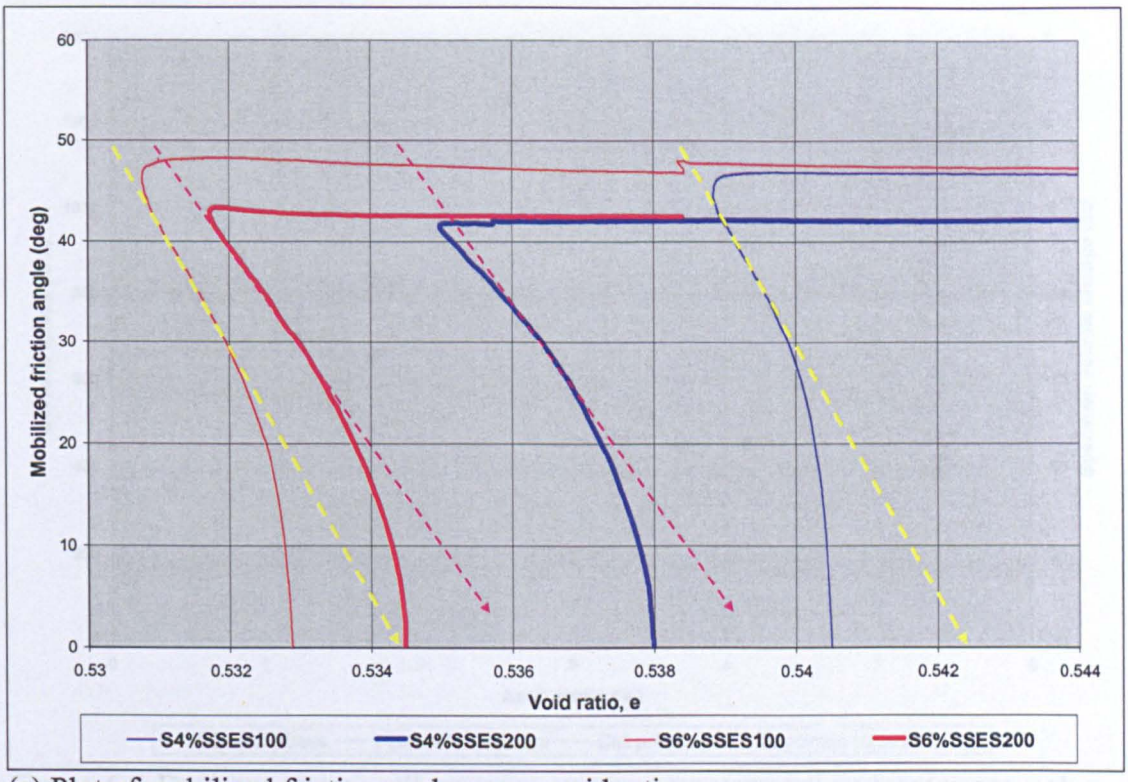

(a) Plot of mobilized friction angle versus void ratio.

(b) Plot of S8%SSES300.

Figure 6.4 Plots of mobilized friction angle versus void ratio to indicate the breakage and "no breakage" conditions.

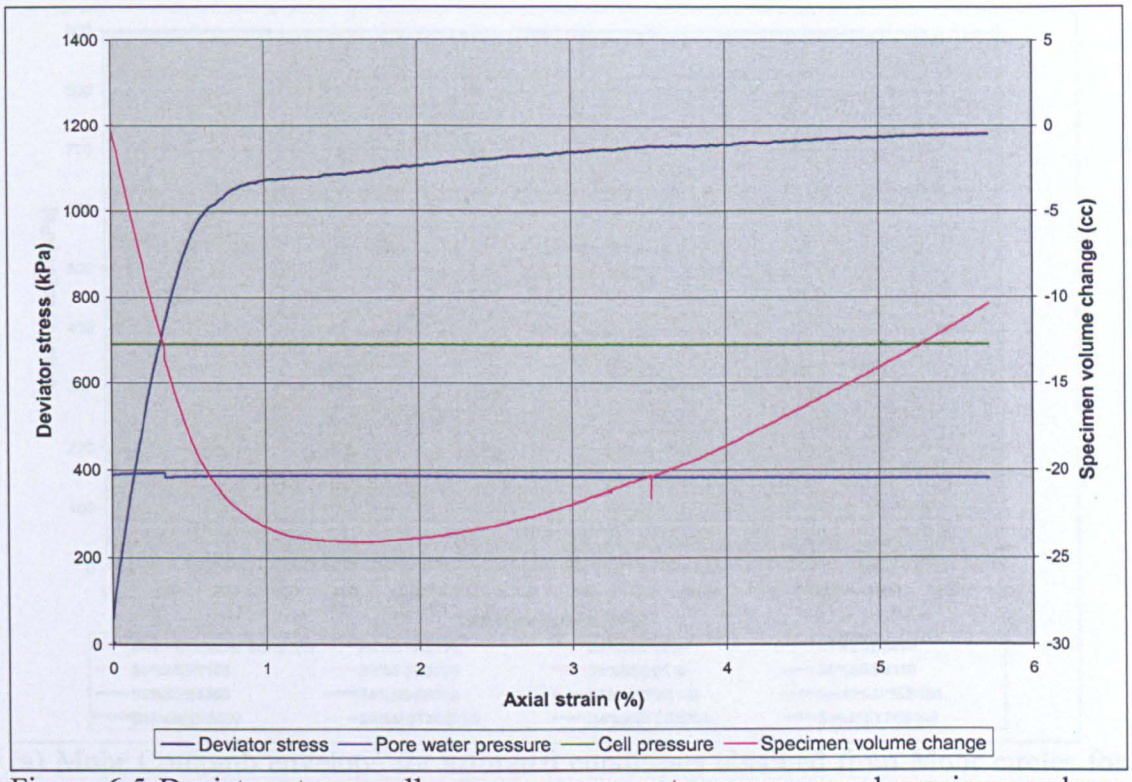

Figure 6.5 Deviator stress, cell pressure, pore water pressure and specimen volume change versus strain for S8%SSES300.

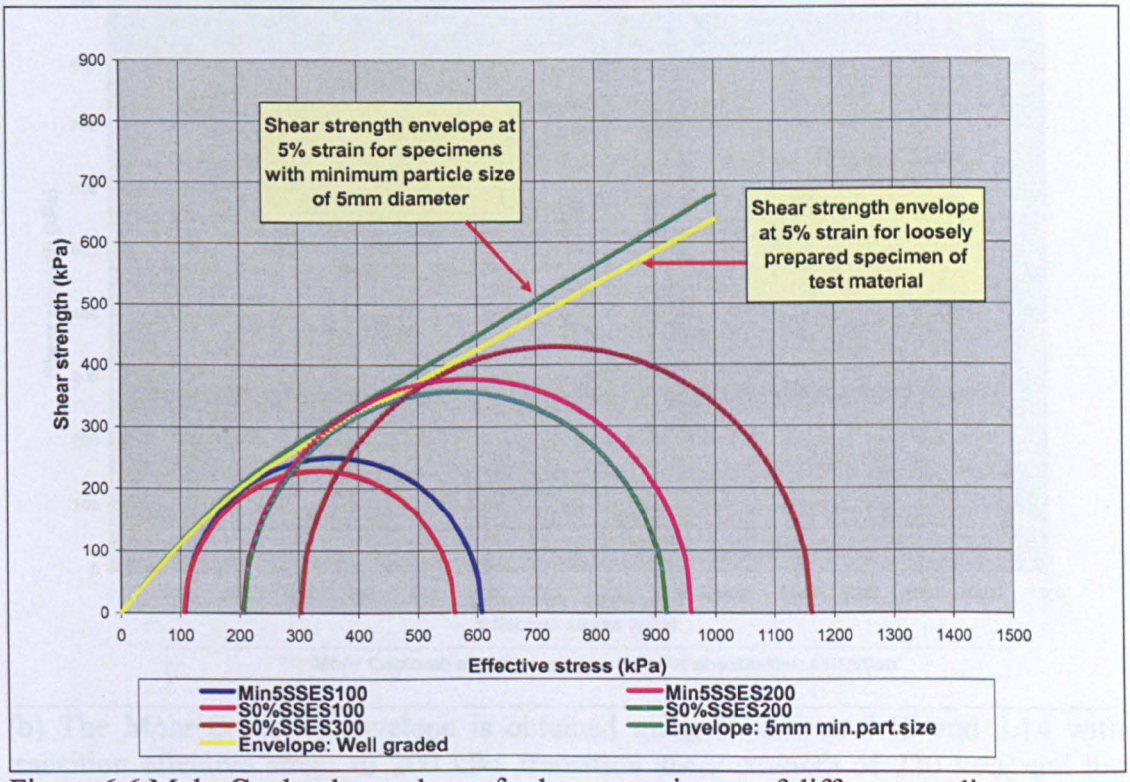

Figure 6.6 Mohr Coulomb envelopes for loose specimens of different gradings.

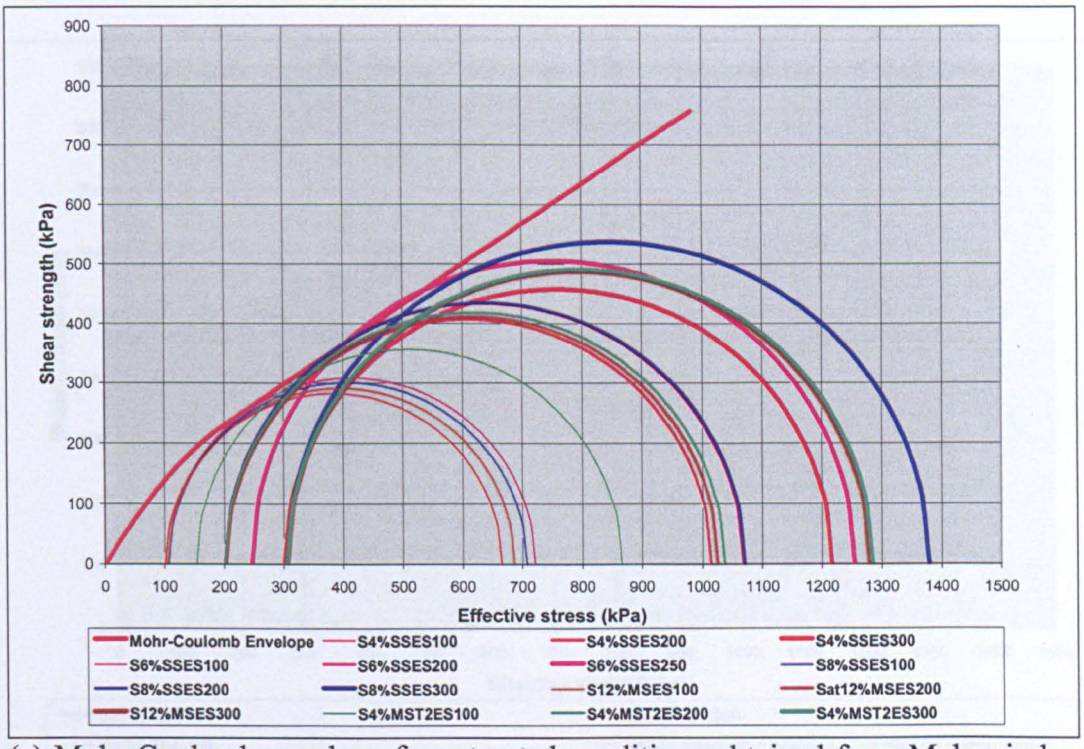

(a) Mohr Coulomb envelope for saturated conditions obtained from Mohr circles for shear strength tests on saturated specimens according to the data listed in Table 5.3.

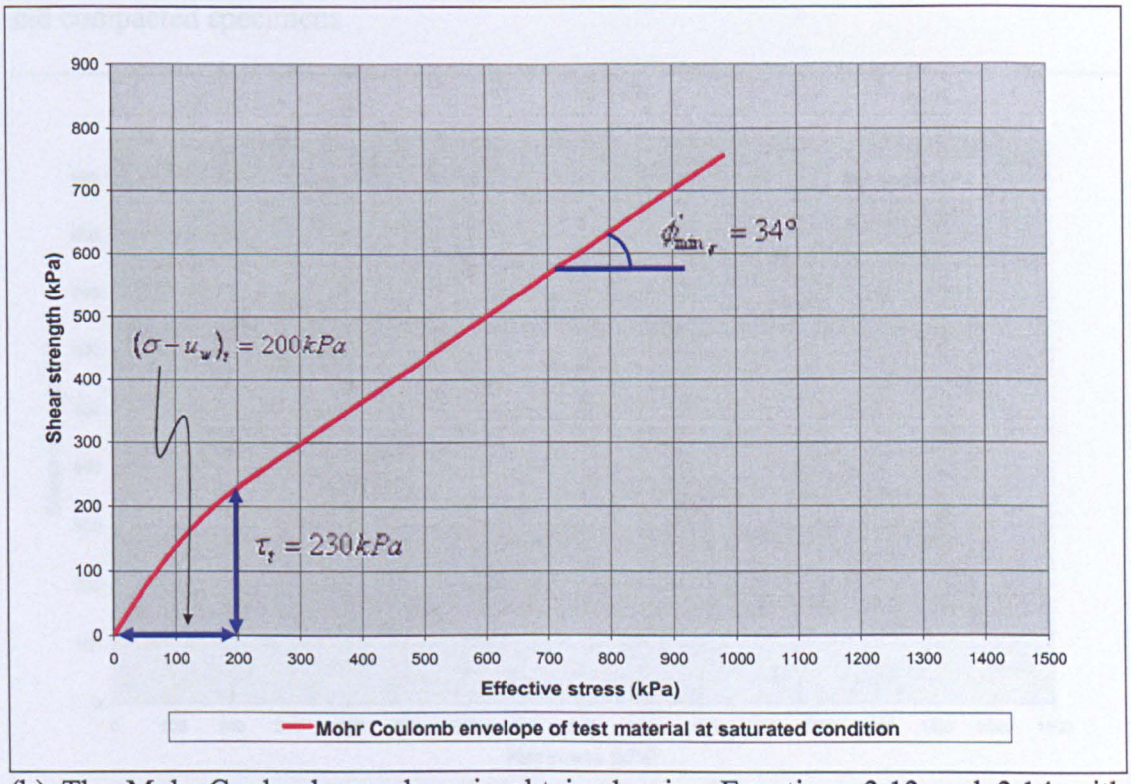

(b) The Mohr-Coulomb envelope is obtained using Equations 3.13 and 3.14 with transition effective stress of 200 kPa, transition shear strength of 230 kPa, and the minimum internal friction angle, $\phi'_{\min_f}$ of 34°.

Figure 6.7 Saturated shear strength behaviour of test material with respect to effective stress and the corresponding shear strength parameters.

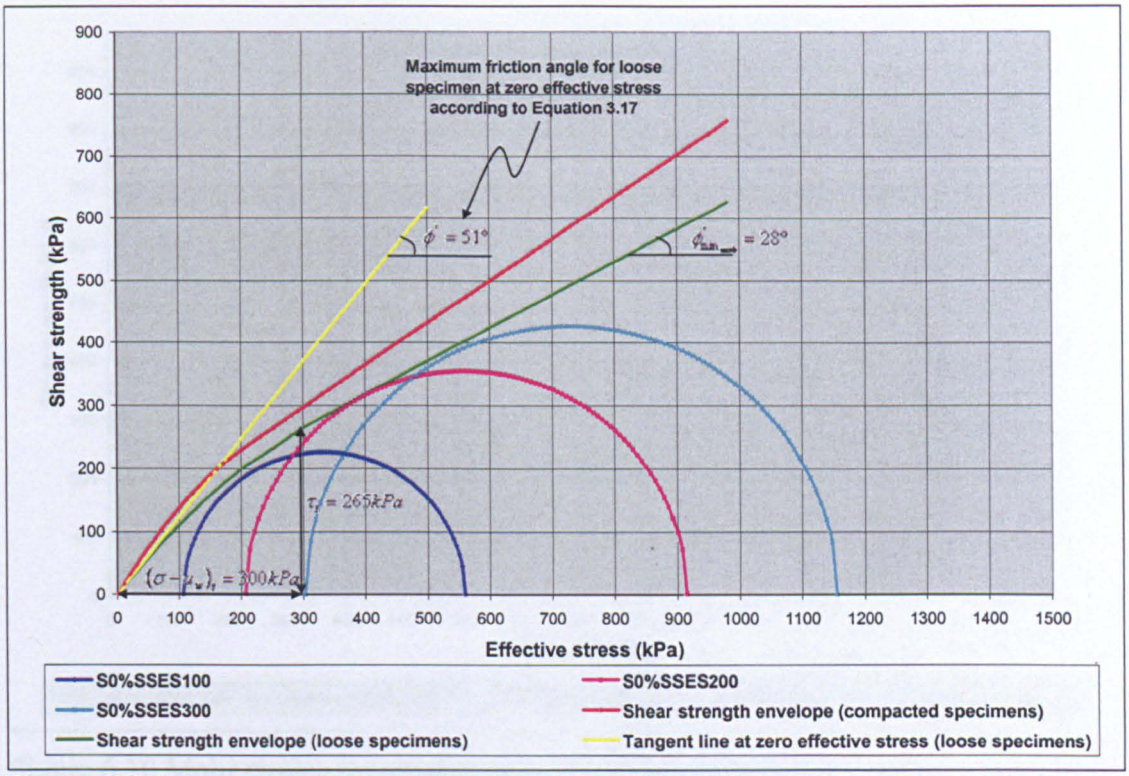

Figure 6.8 Comparison of the shear strength envelopes for loosely prepared specimens and compacted specimens.

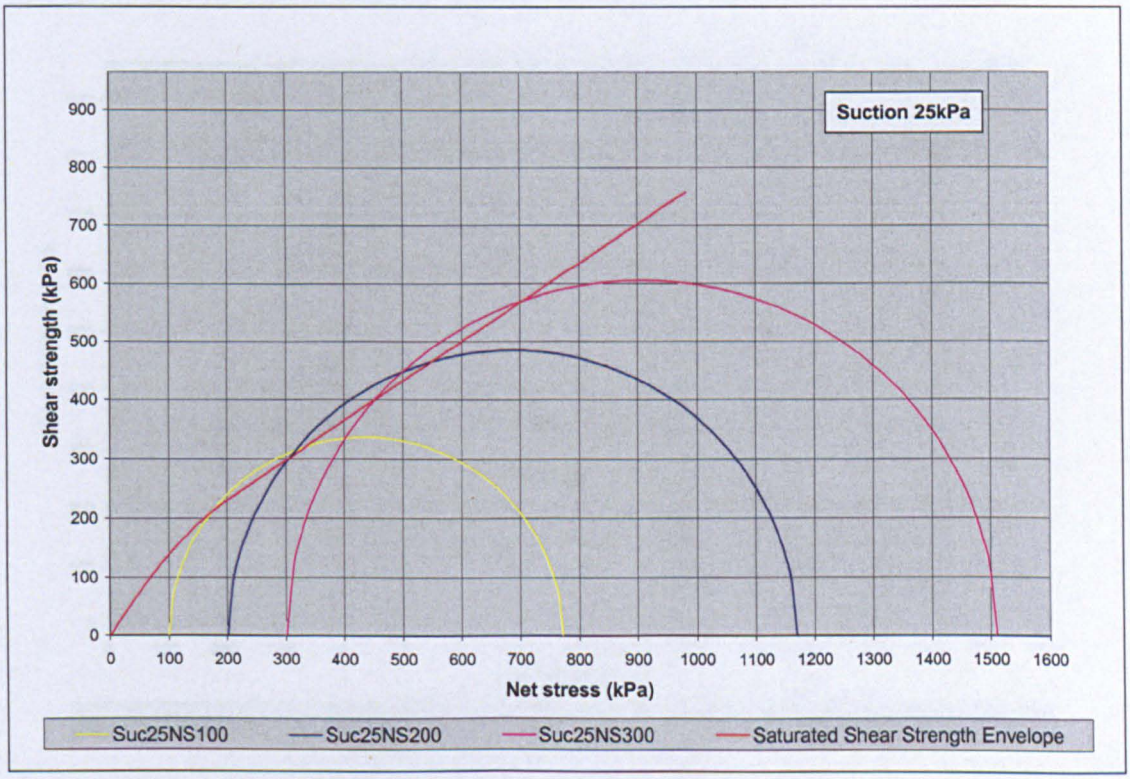

Figure 6.9 Mohr circles for unsaturated consolidated drained triaxial tests at suction 25kPa compared to the saturated shear strength envelope.

Figure 6.10 Mohr circles for unsaturated consolidated drained triaxial tests at suction 50kPa compared to the saturated shear strength envelope.

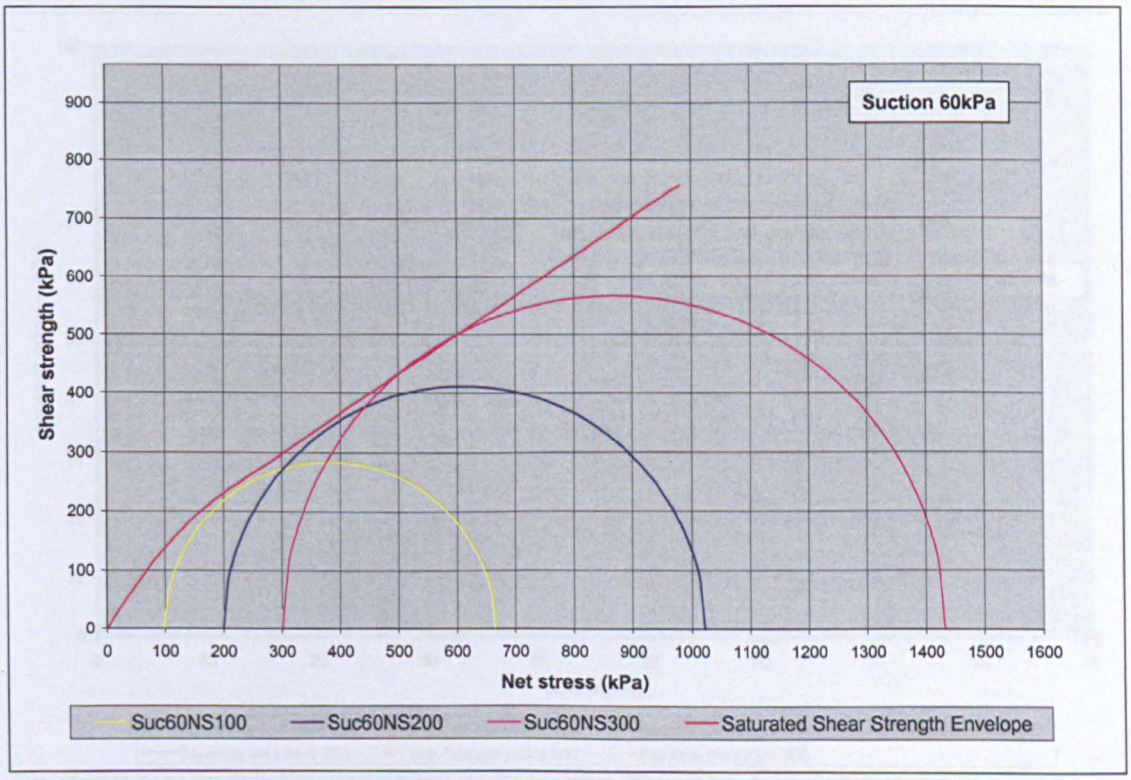

Figure 6.11 Mohr circles for unsaturated consolidated drained triaxial tests at suction 60kPa compared to the saturated shear strength envelope.

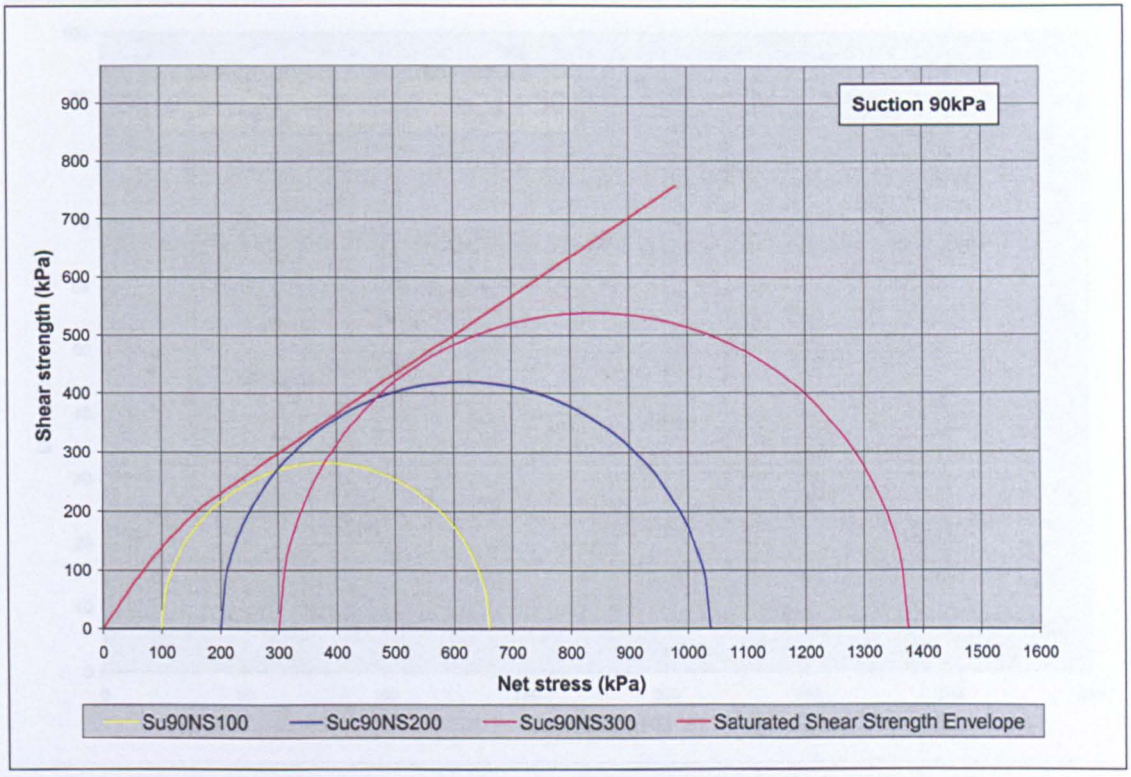

Figure 6.12 Mohr circles for unsaturated consolidated drained triaxial tests at suction 90kPa compared to the saturated shear strength envelope.

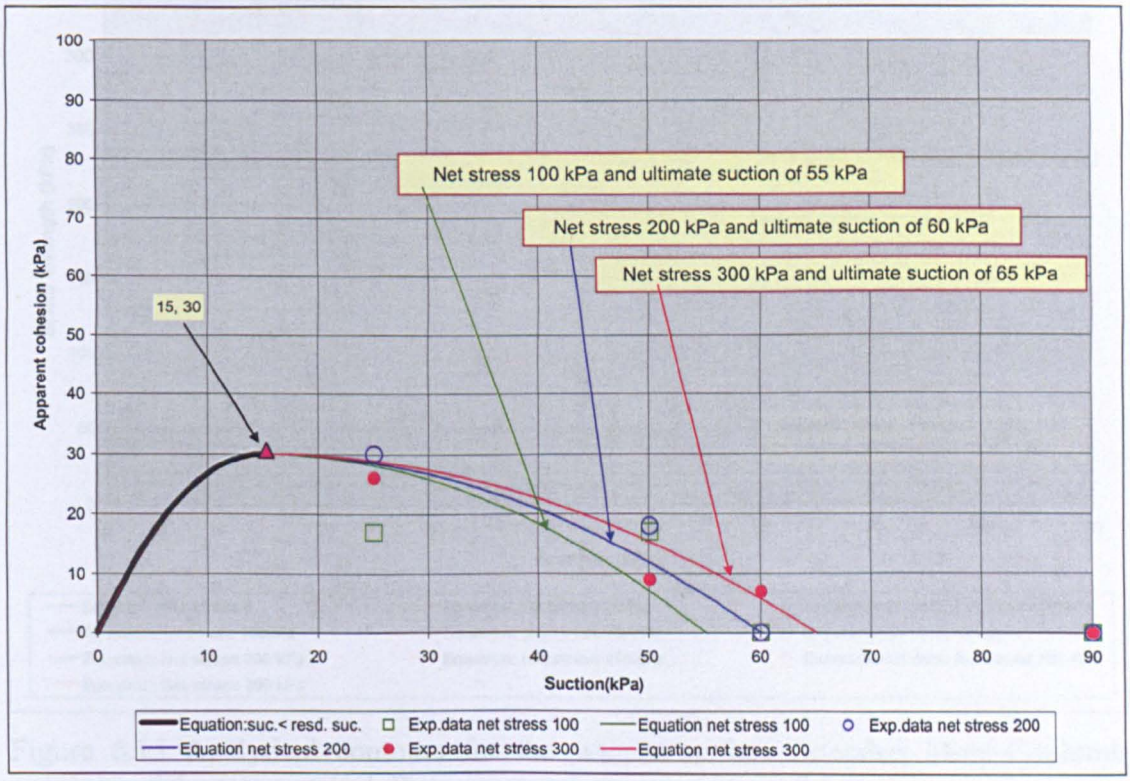

Figure 6.13 The variation of apparent shear strength with respect to suction using Equations 3.4 and 3.7 excluding the saturated shear strength.

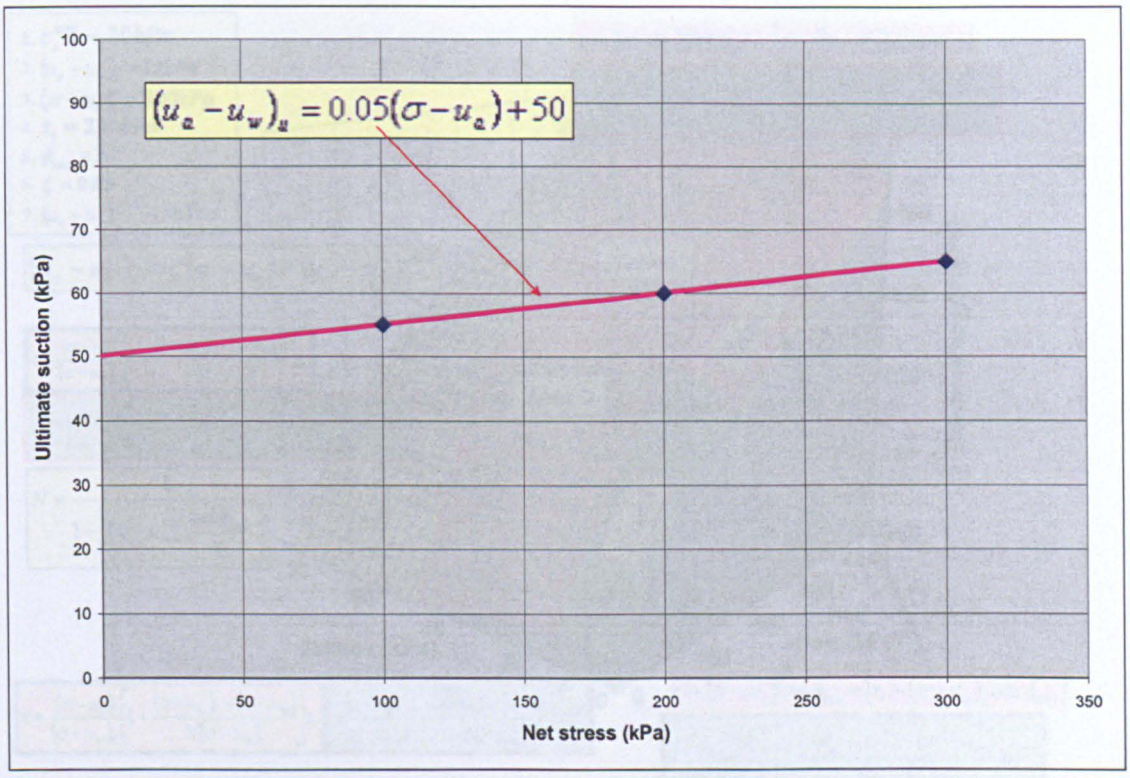

Figure 6.14 The assumed linear variation of ultimate suction with respect to effective stress from the data in Figure 6.13.

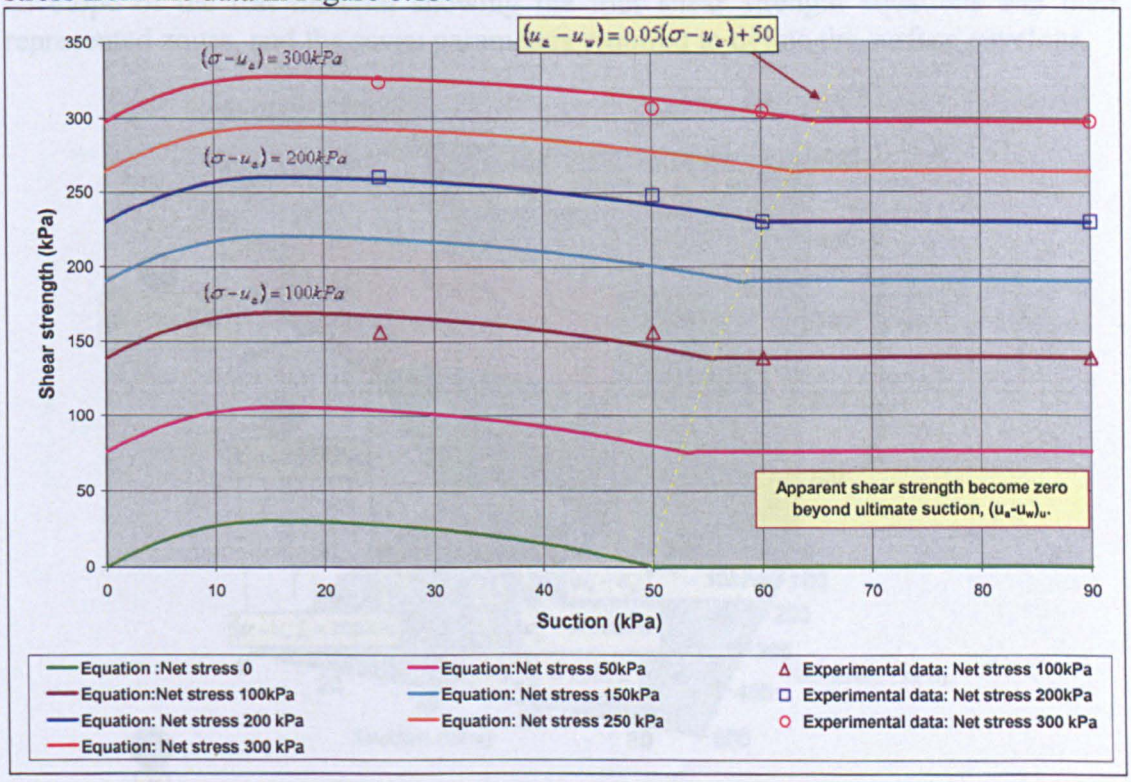

Figure 6.15 Analytical contours for the warped-surface extended Mohr-Coulomb envelope of the test material. Data points are the experimental data.

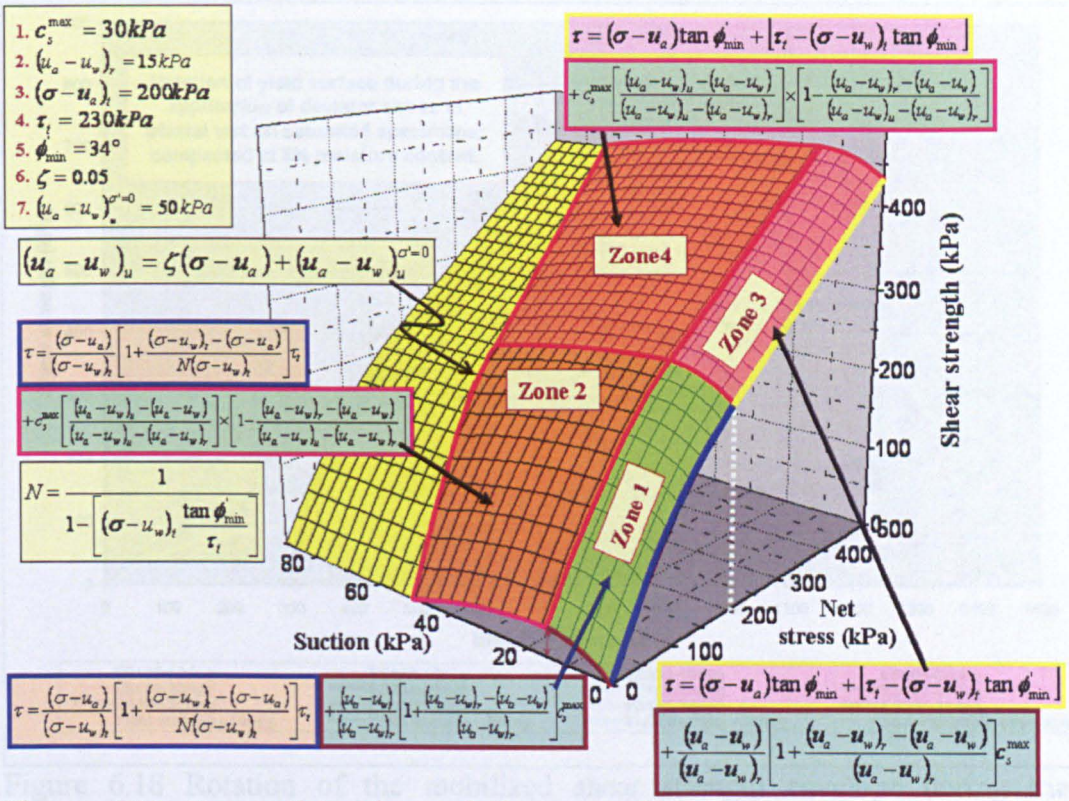

Figure 6.16 Perspective view of the warped-surface extended Mohr-Coulomb envelope of the test material showing the four shear strength equations and their represented zones, and the seven parameters required to define the surface envelope.

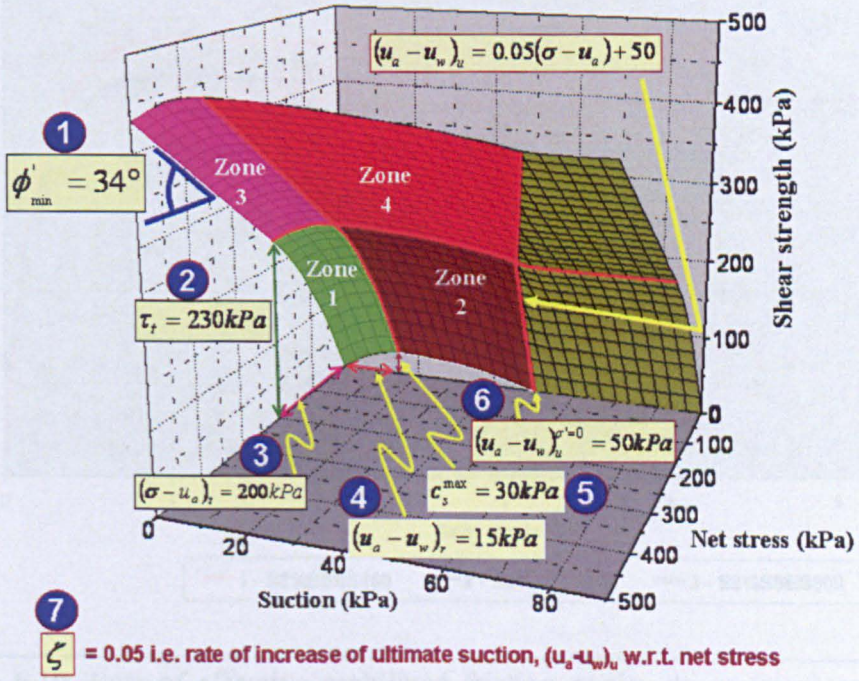

Figure 6.17 Perspective view from underneath the warped-surface extended Mohr-Coulomb envelope of the test material showing the shear strength parameters and the dimensions they represent.

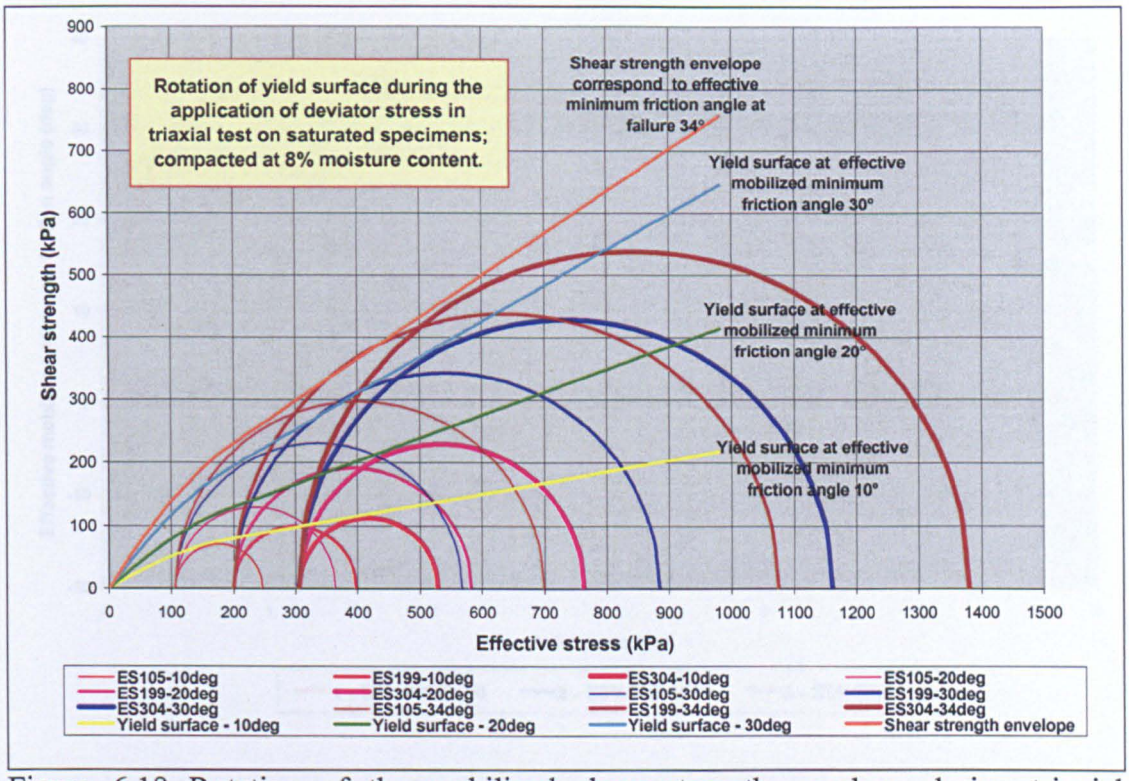

Figure 6.18 Rotation of the mobilized shear strength envelope during triaxial compression test on saturated specimens compacted at 8% moisture content.

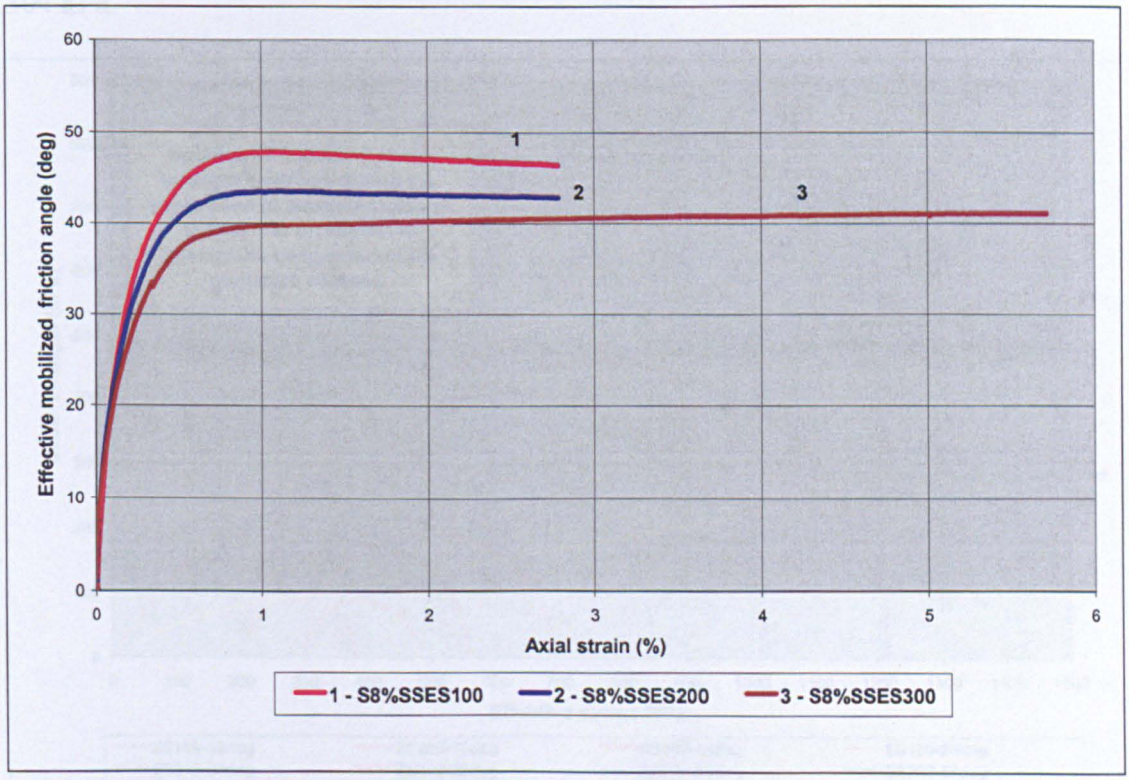

Figure 6.19 Plots of effective mobilized friction angle, ϕ'_{mob}, versus axial strain for triaxial tests on saturated specimens compacted at 8% moisture content.

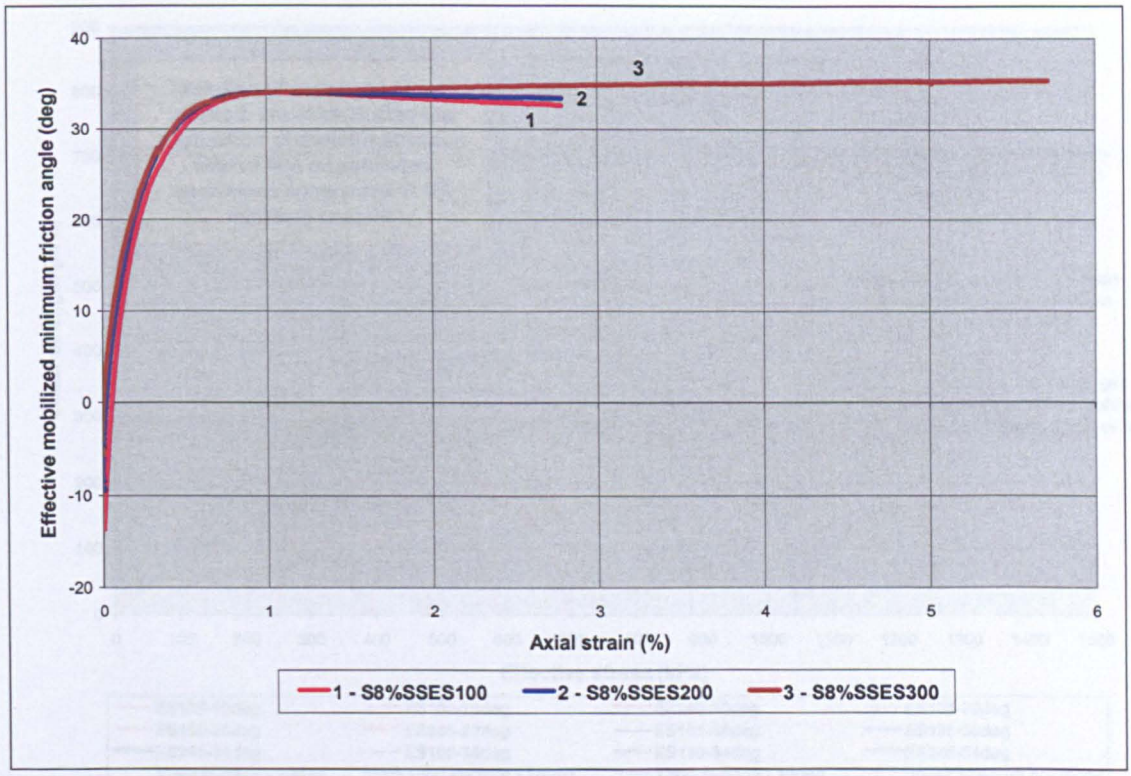

Figure 6.20 Unique graphs of $\phi'_{\min_{mob}}$ - ε_a for triaxial tests on saturated specimens compacted at 8% moisture content and sheared at effective stresses of 105, 201 and 304 kPa.

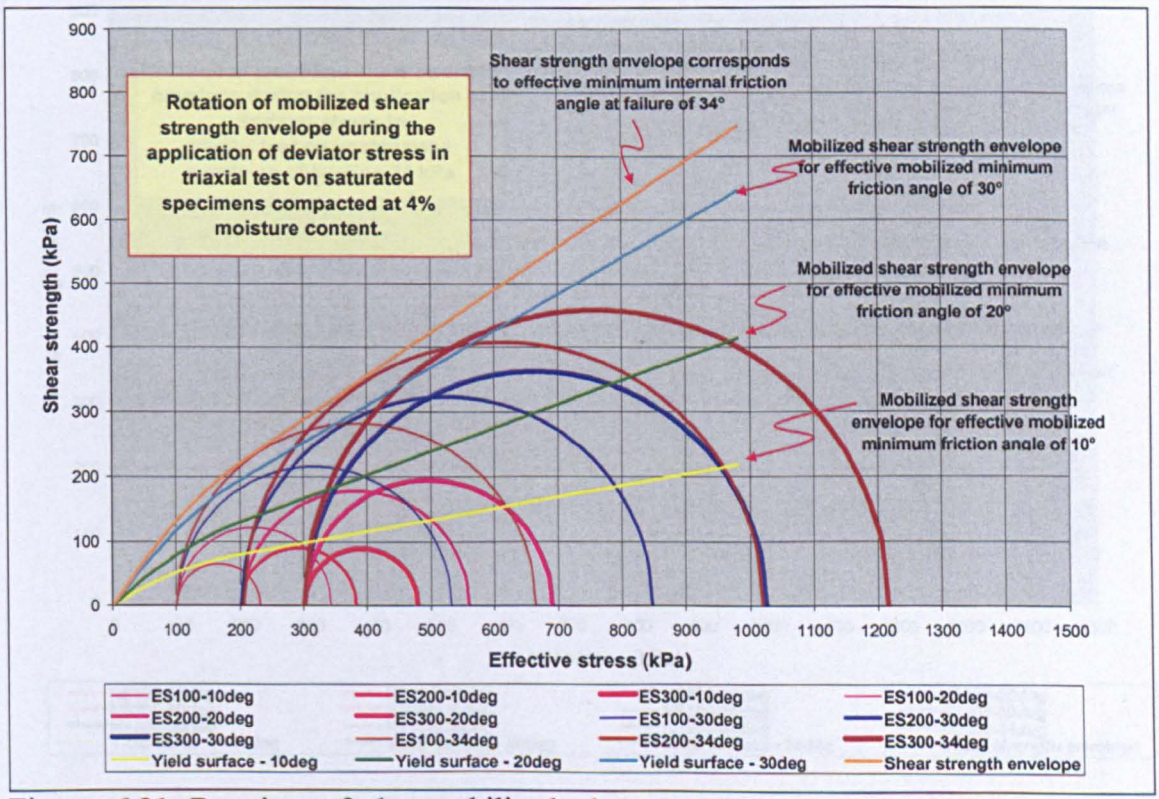

Figure 6.21 Rotation of the mobilized shear strength envelope during triaxial compression test on saturated specimens compacted at 4% moisture content.

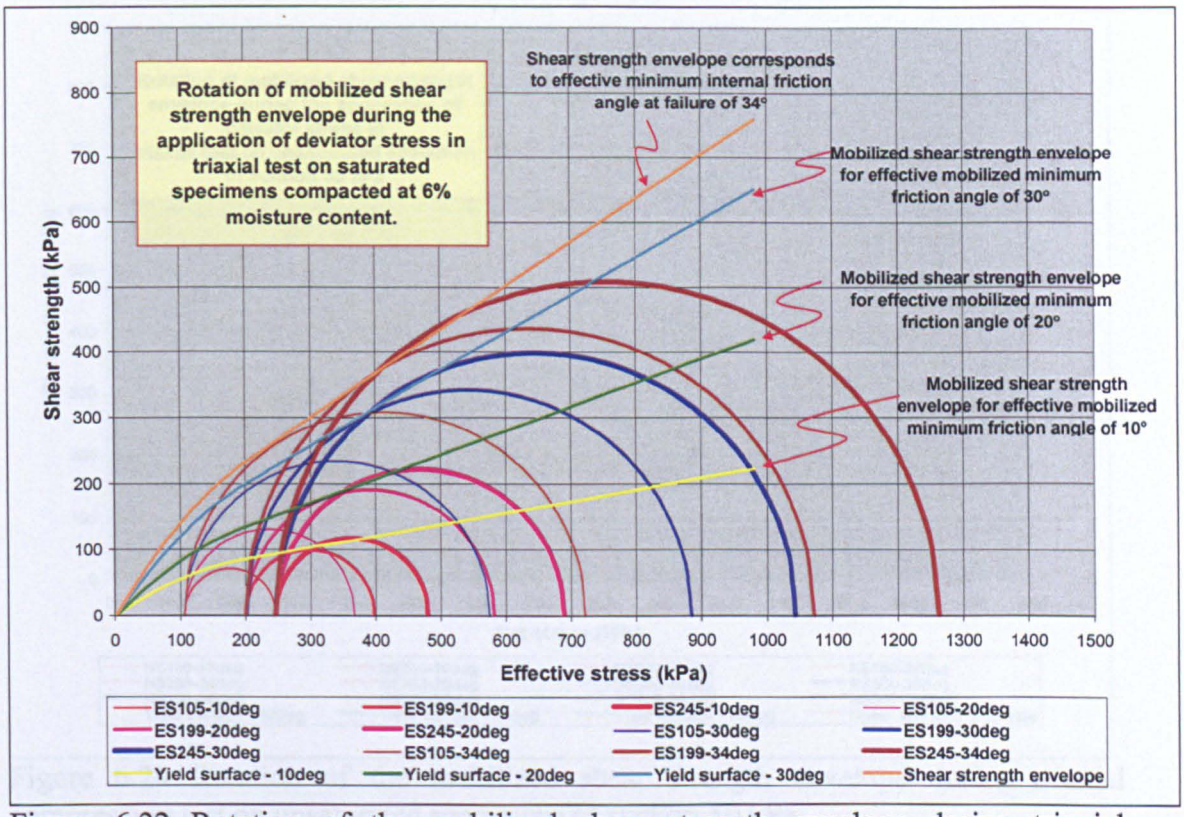

Figure 6.22 Rotation of the mobilized shear strength envelope during triaxial compression test on saturated specimens compacted at 6% moisture content.

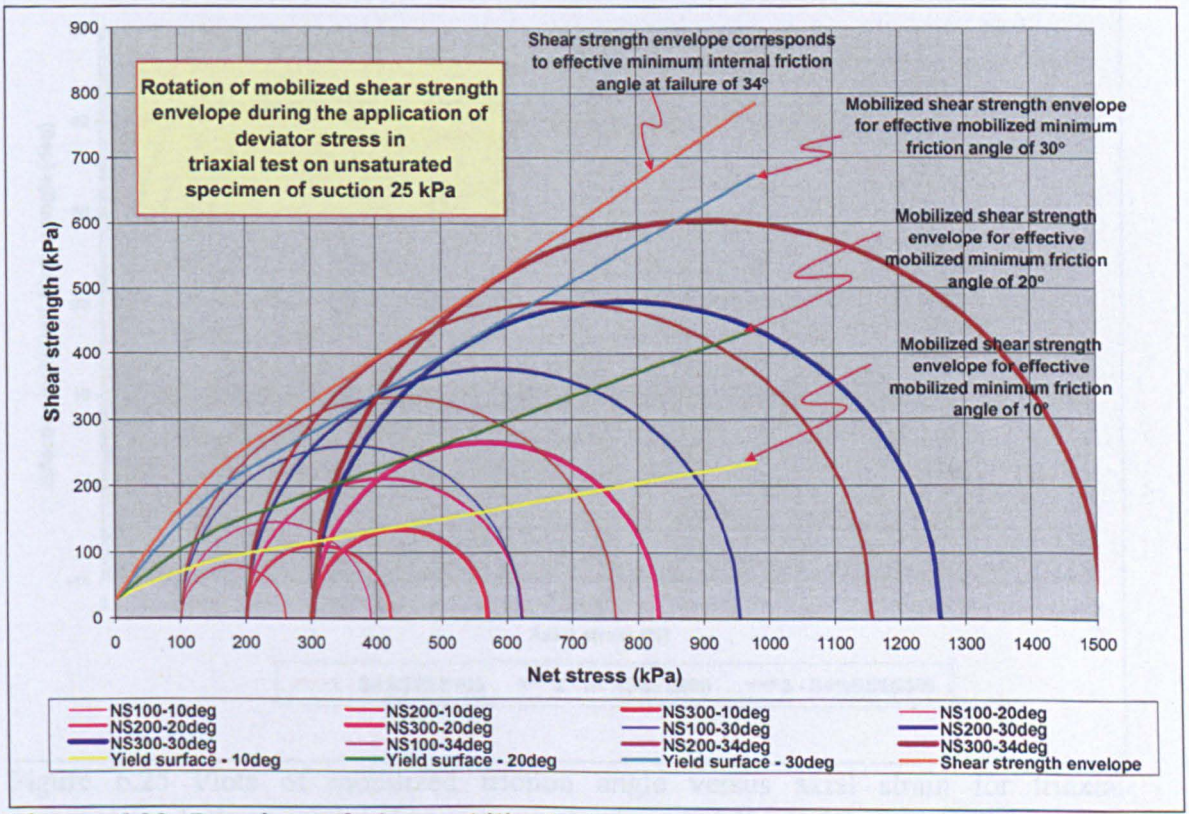

Figure 6.23 Rotation of the mobilized shear strength envelope during triaxial compression test on unsaturated specimens of suction 25 kPa.

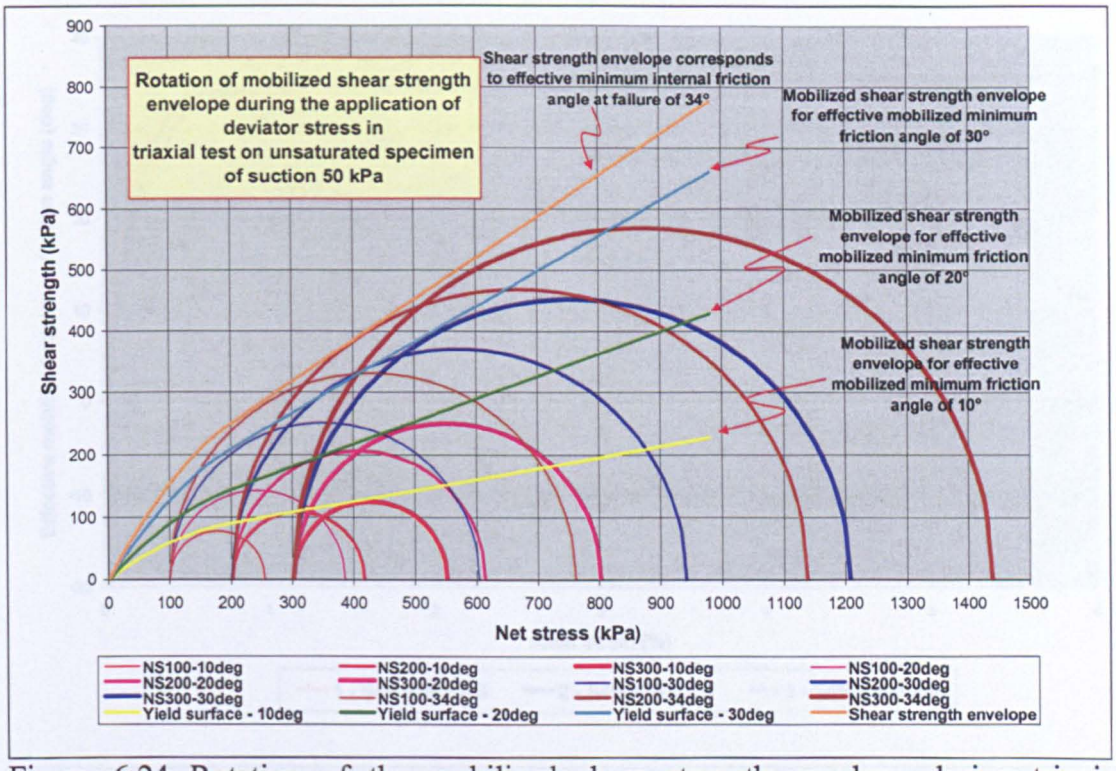

Figure 6.24 Rotation of the mobilized shear strength envelope during triaxial compression test on unsaturated specimens of suction 50 kPa.

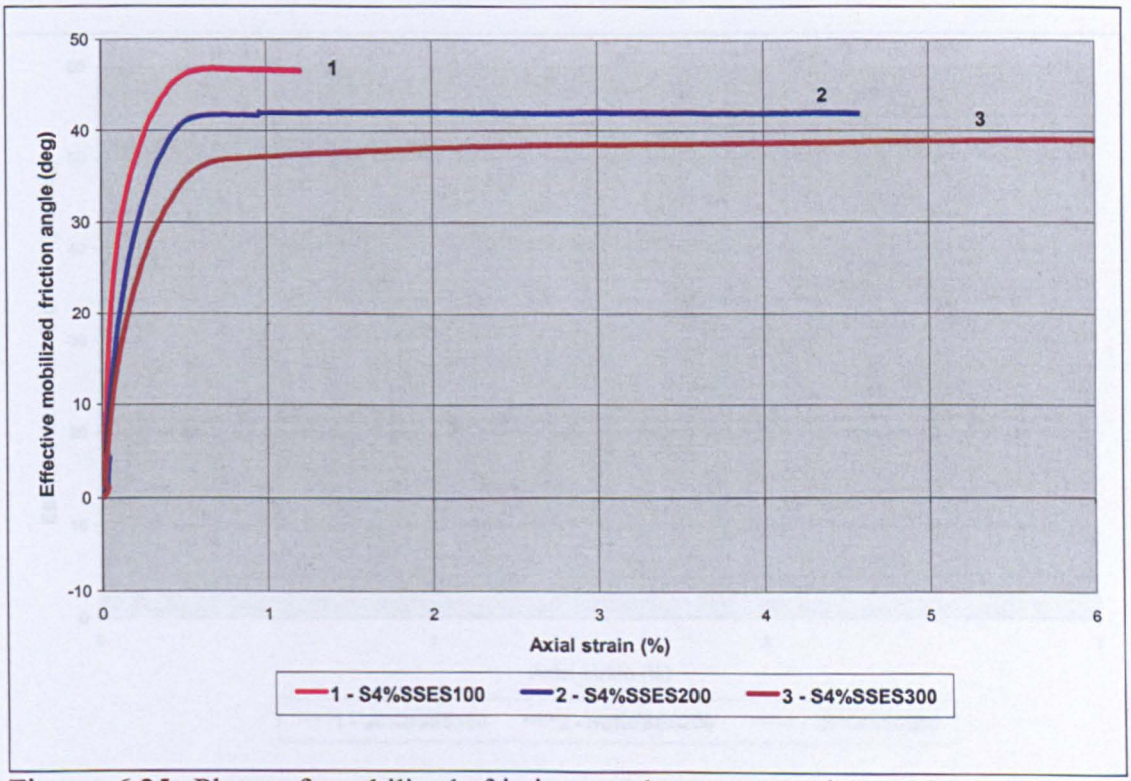

Figure 6.25 Plots of mobilized friction angle versus axial strain for triaxial compression tests on saturated specimens compacted at 4% moisture content.

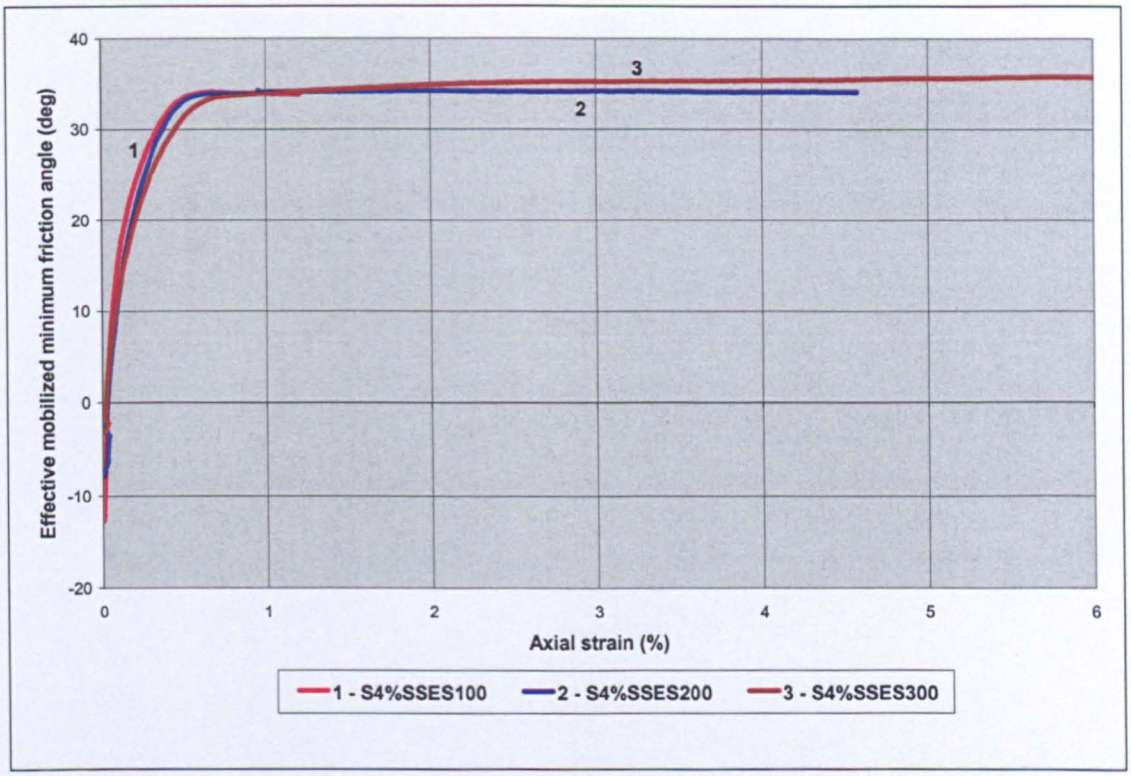

Figure 6.26 The dispersion on the graphs of $\phi'_{\min_{mob}}$ - ε_a for triaxial compression tests on saturated specimens compacted at 4% moisture content and sheared at effective stresses of 100, 200 and 300 kPa.

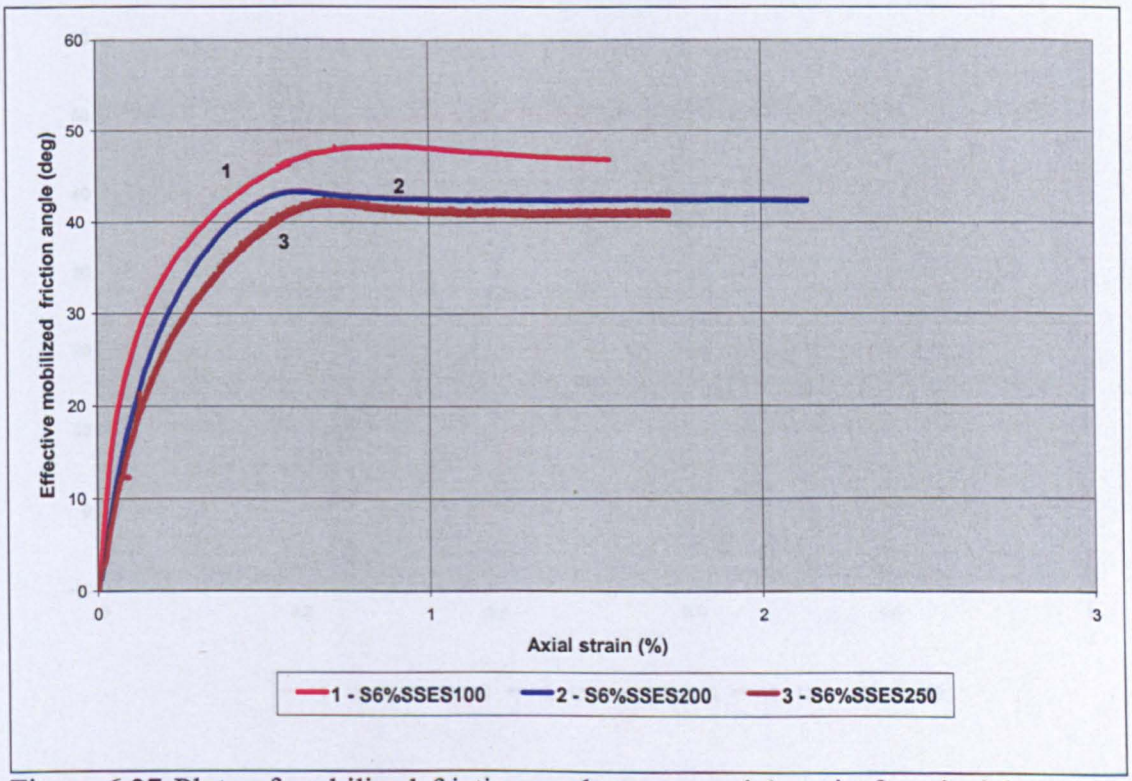

Figure 6.27 Plots of mobilized friction angle versus axial strain for triaxial tests on saturated specimens compacted at 6% moisture content.

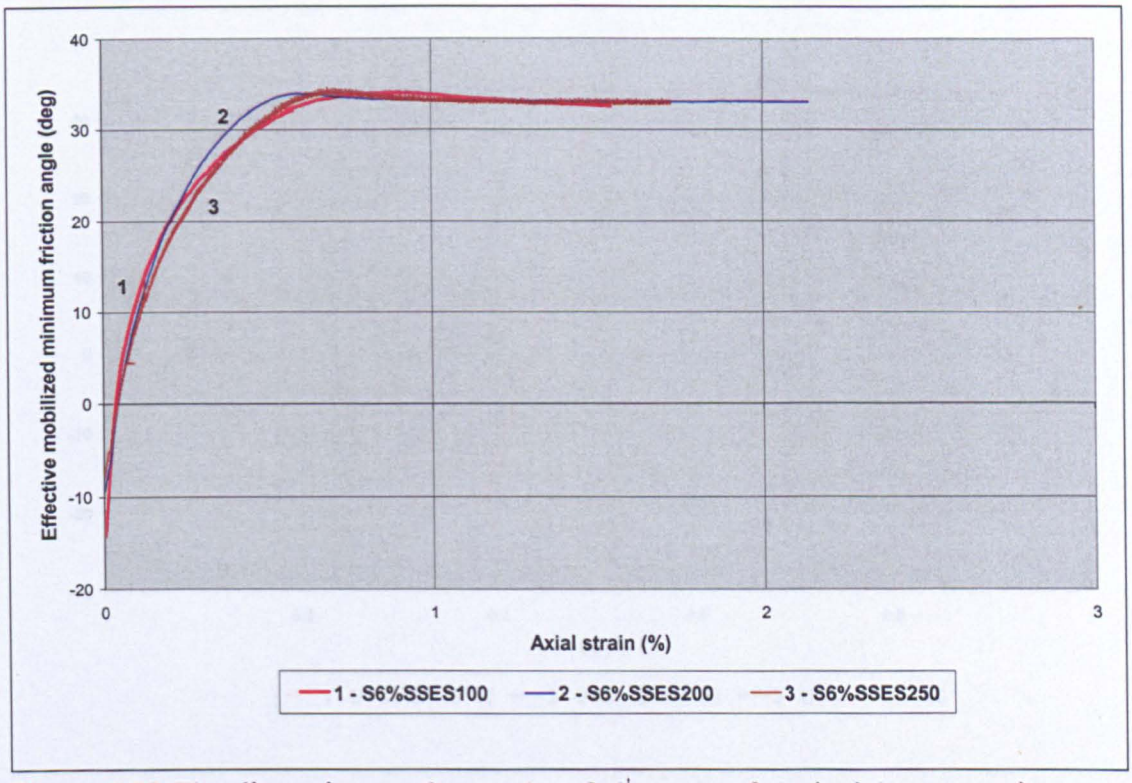

Figure 6.28 The dispersion on the graphs of $\phi'_{\min_{mob}}$ - ε_a for triaxial compression tests on saturated specimens compacted at 6% moisture content and sheared at effective stresses of 100, 200 and 300 kPa.

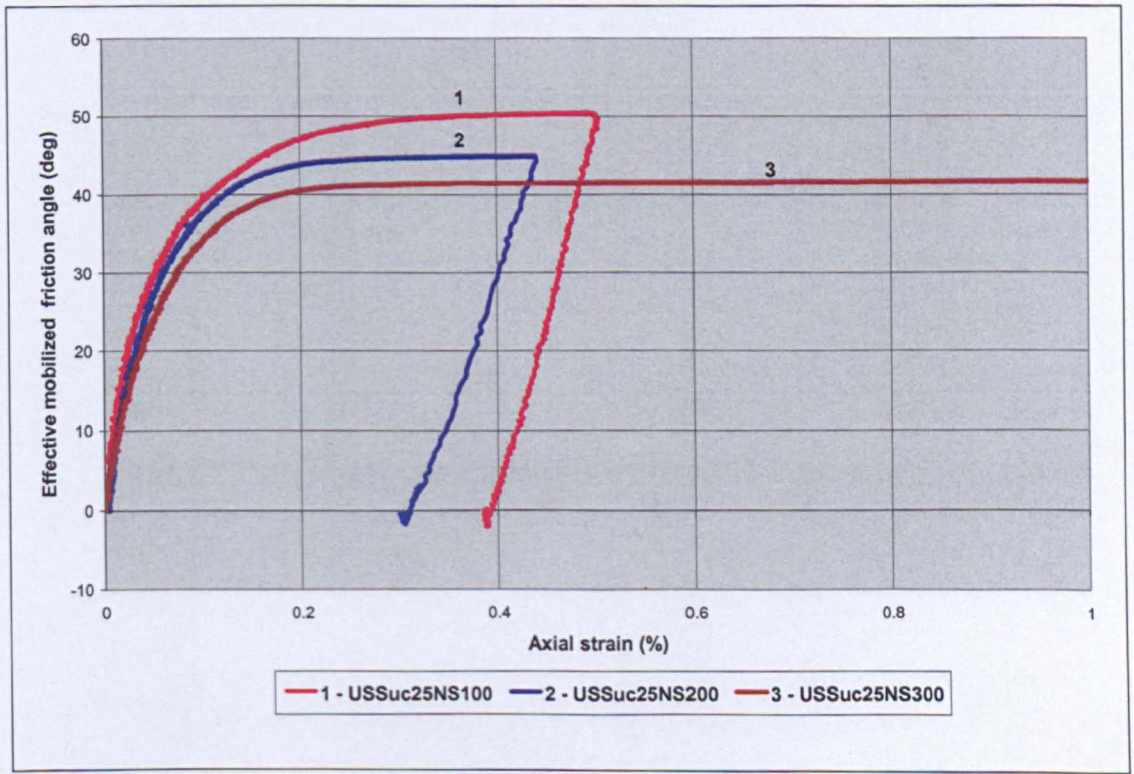

Figure 6.29 Plots of mobilized friction angle versus axial strain for triaxial tests on unsaturated specimens of suction 25 kPa and sheared at net stresses of 100, 200 and 300 kPa.

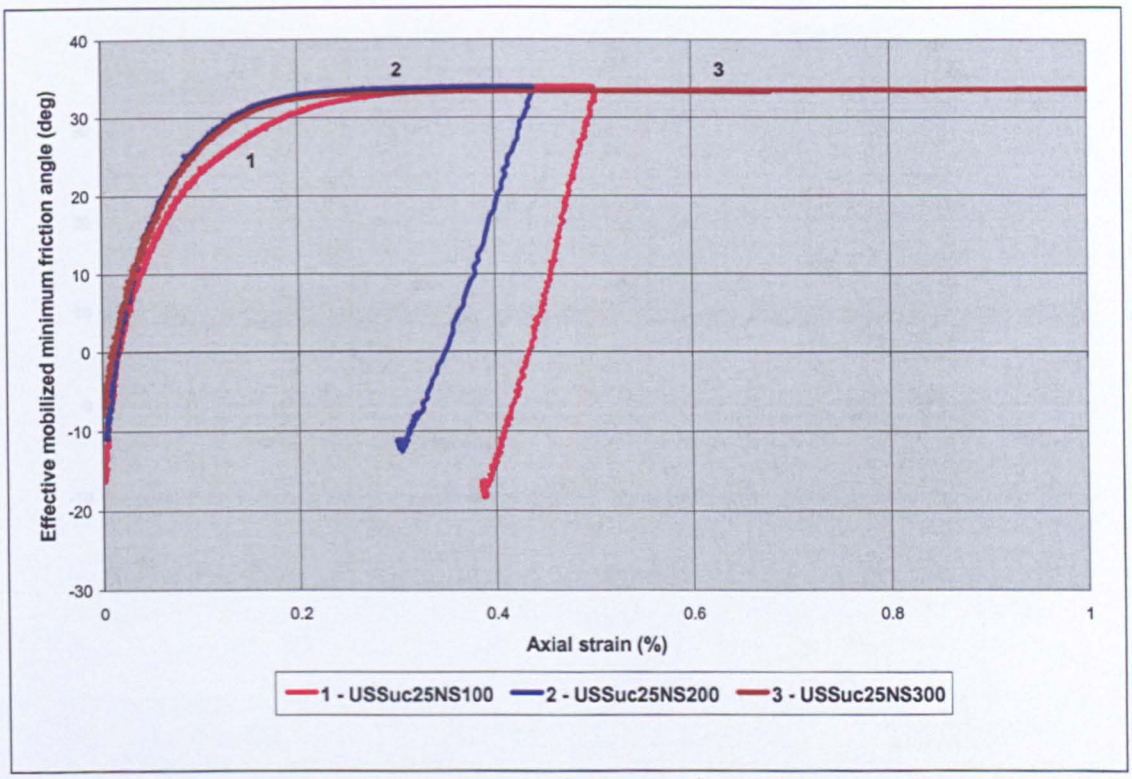

Figure 6.30 The slight dispersion on the graphs of $\phi'_{\min_{mob}}$ - ε_a for triaxial compression tests on unsaturated specimens of suction 25 kPa and sheared at effective stresses of 100, 200 and 300 kPa.

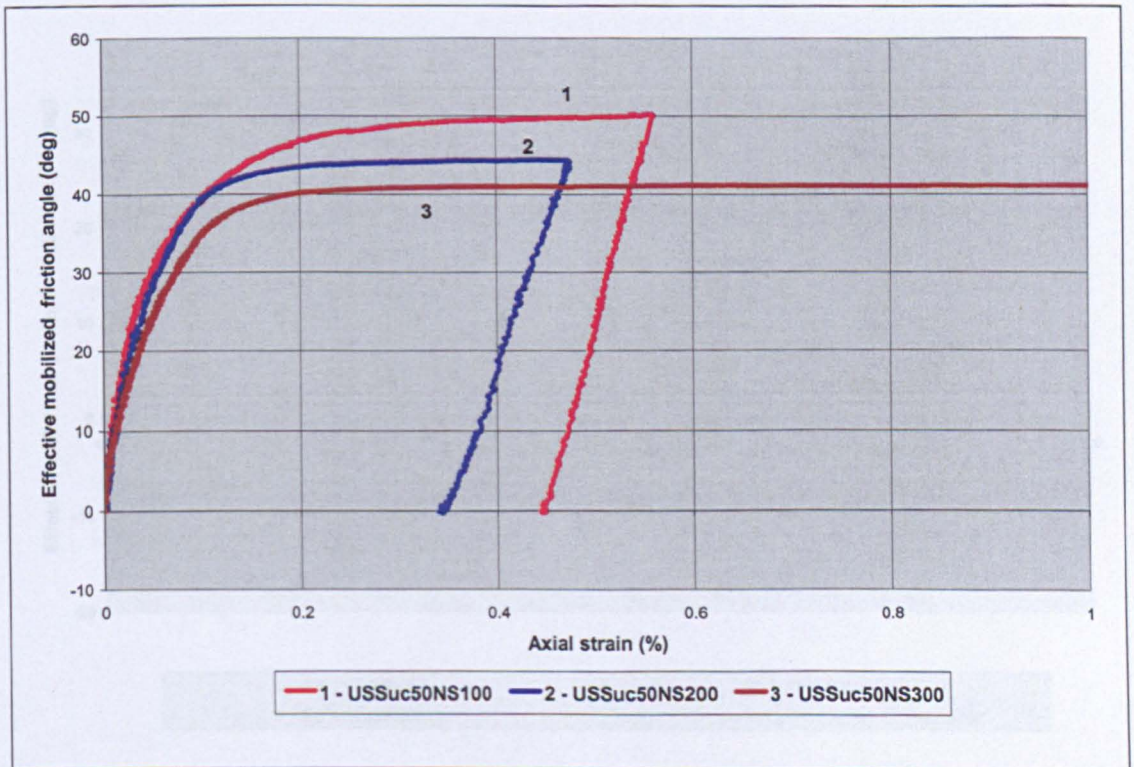

Figure 6.31 Plots of mobilized friction angle versus axial strain for triaxial tests on unsaturated specimens of suction 50 kPa and sheared at net stresses of 100, 200 and 300 kPa.

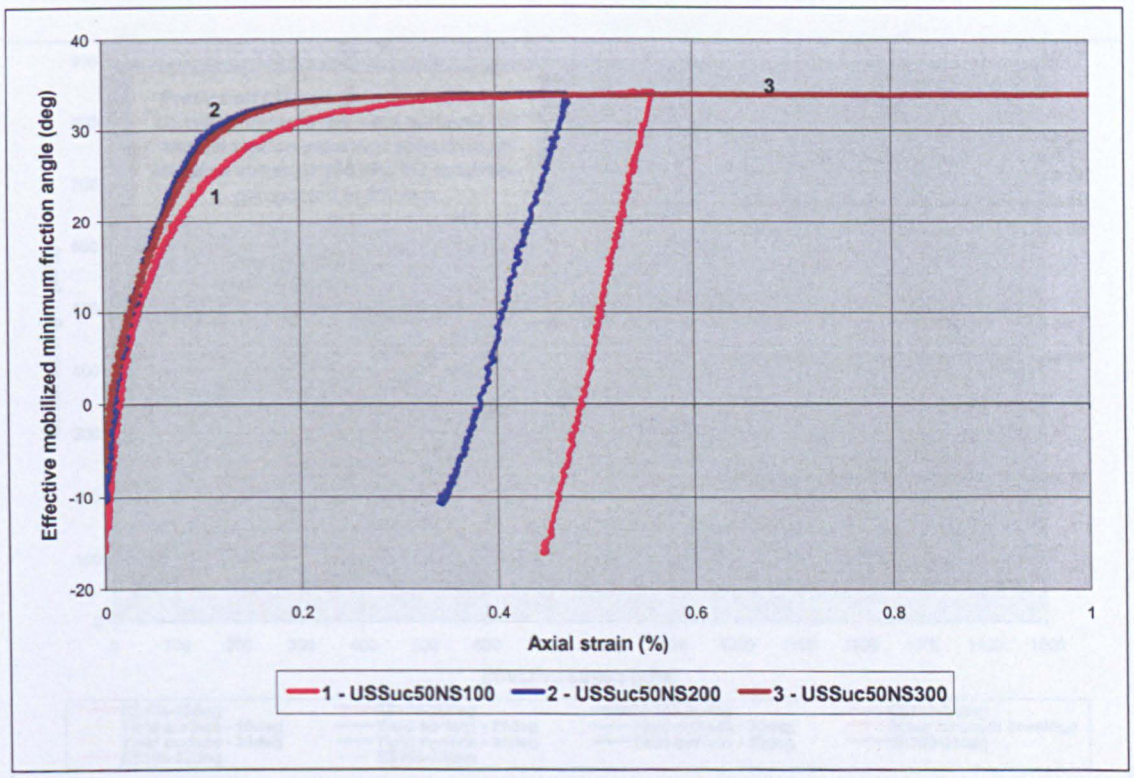

Figure 6.32 The slight dispersion on the graphs of $\phi'_{\min_{mob}} - \varepsilon_a$ for triaxial compression tests on unsaturated specimens of suction 50 kPa and sheared at effective stresses of 100, 200 and 300 kPa.

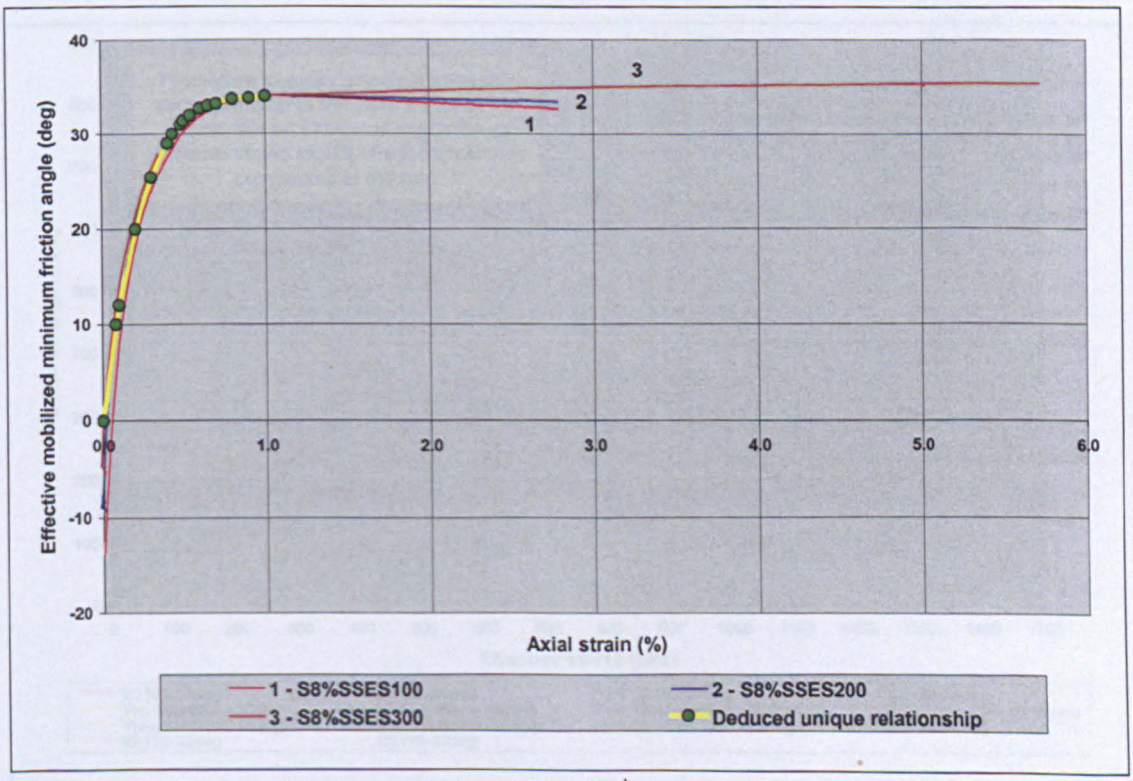

Figure 6.33 Deduced unique relationship of $\phi'_{\min_{mob}} - \varepsilon_a$ for triaxial compression tests on saturated specimens compacted at 8% moisture content.

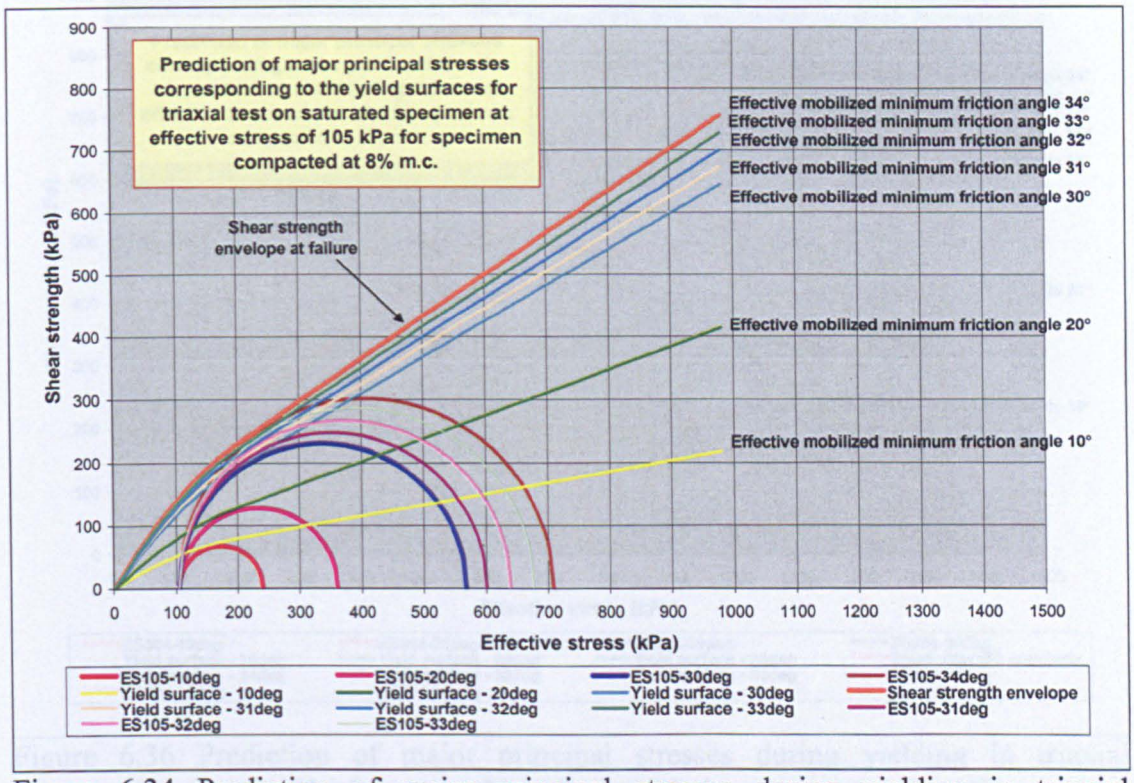

Figure 6.34 Prediction of major principal stresses during yielding in triaxial compression test at effective stress 105 kPa for specimen compacted at 8% moisture content.

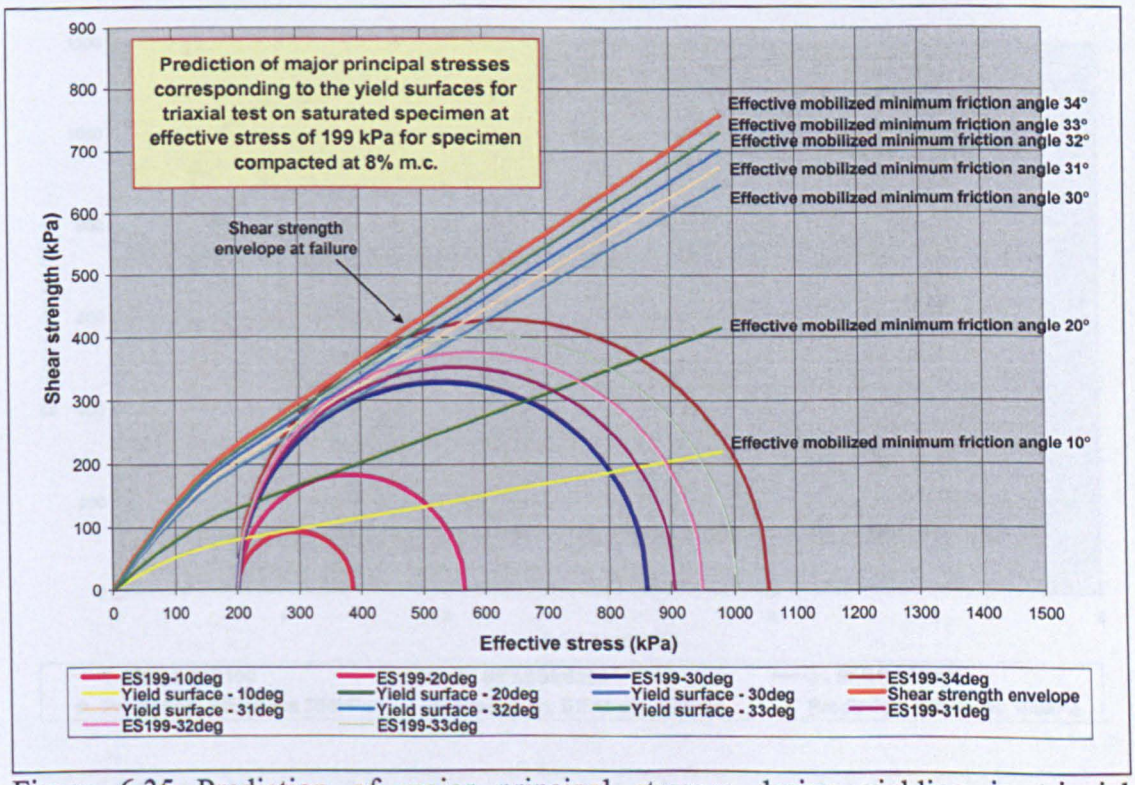

Figure 6.35 Prediction of major principal stresses during yielding in triaxial compression test at effective stress 199 kPa for specimen compacted at 8% moisture content.

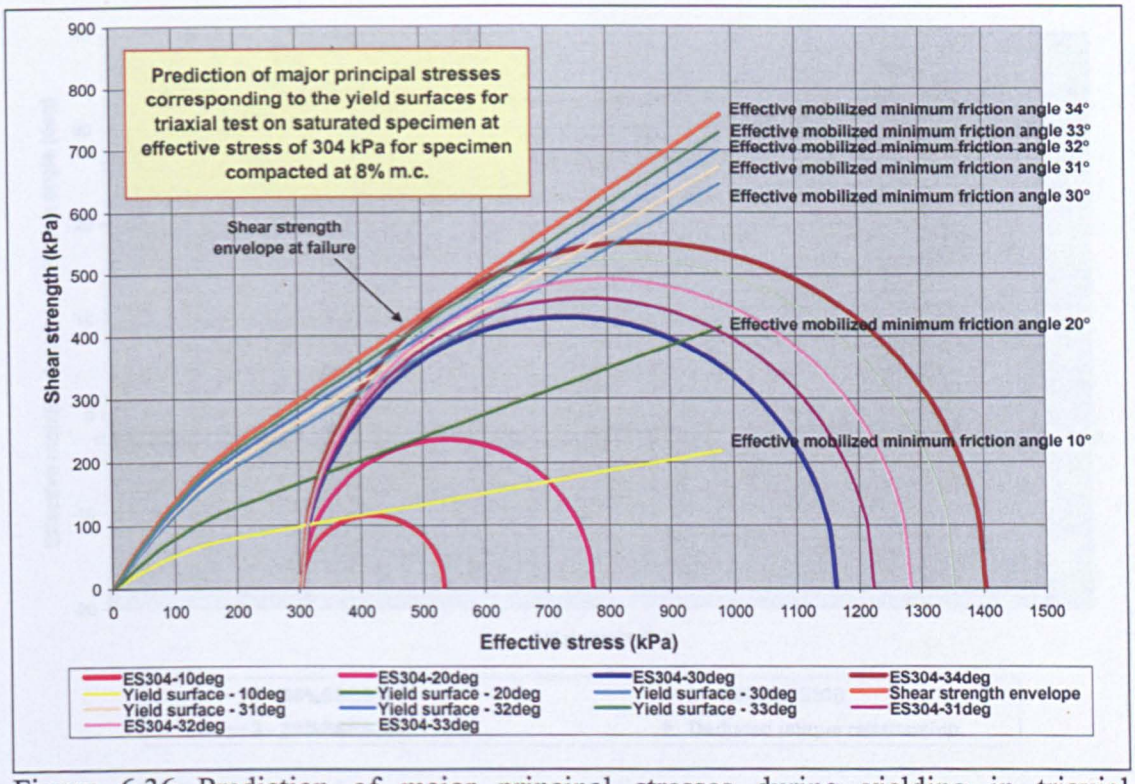

Figure 6.36 Prediction of major principal stresses during yielding in triaxial compression test at effective stress 304 kPa for specimen compacted at 8% moisture content.

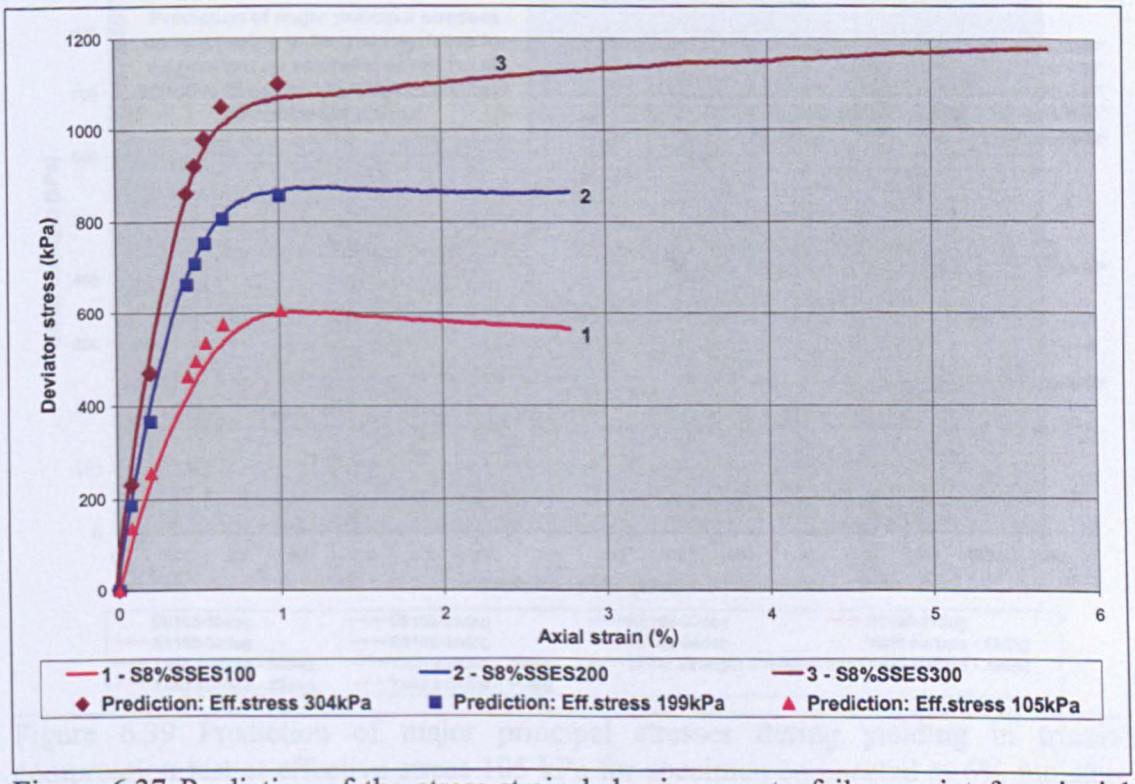

Figure 6.37 Prediction of the stress-strain behaviour up to failure point for triaxial tests on saturated specimens compacted at 8% moisture content at effective stresses of 105, 199 and 304 kPa.

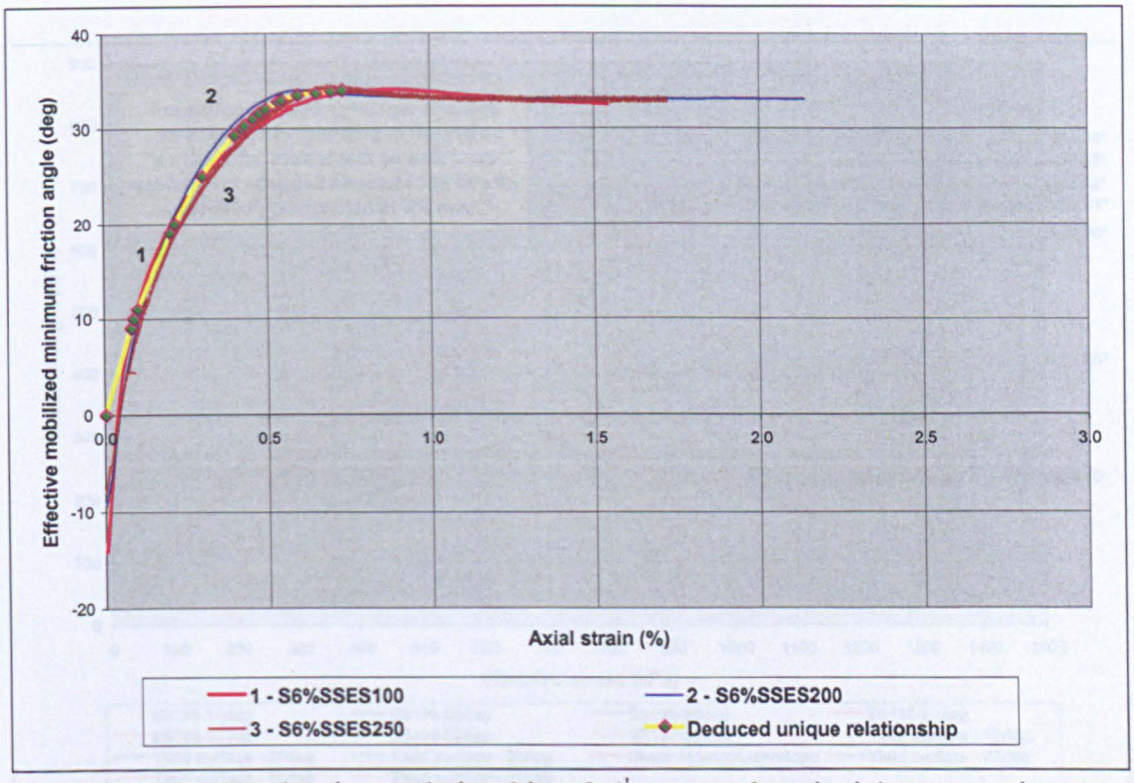

Figure 6.38 Deduced unique relationship of $\phi'_{\min_{mob}}$ - ε_a for triaxial compression tests on saturated specimens compacted at 6% moisture content.

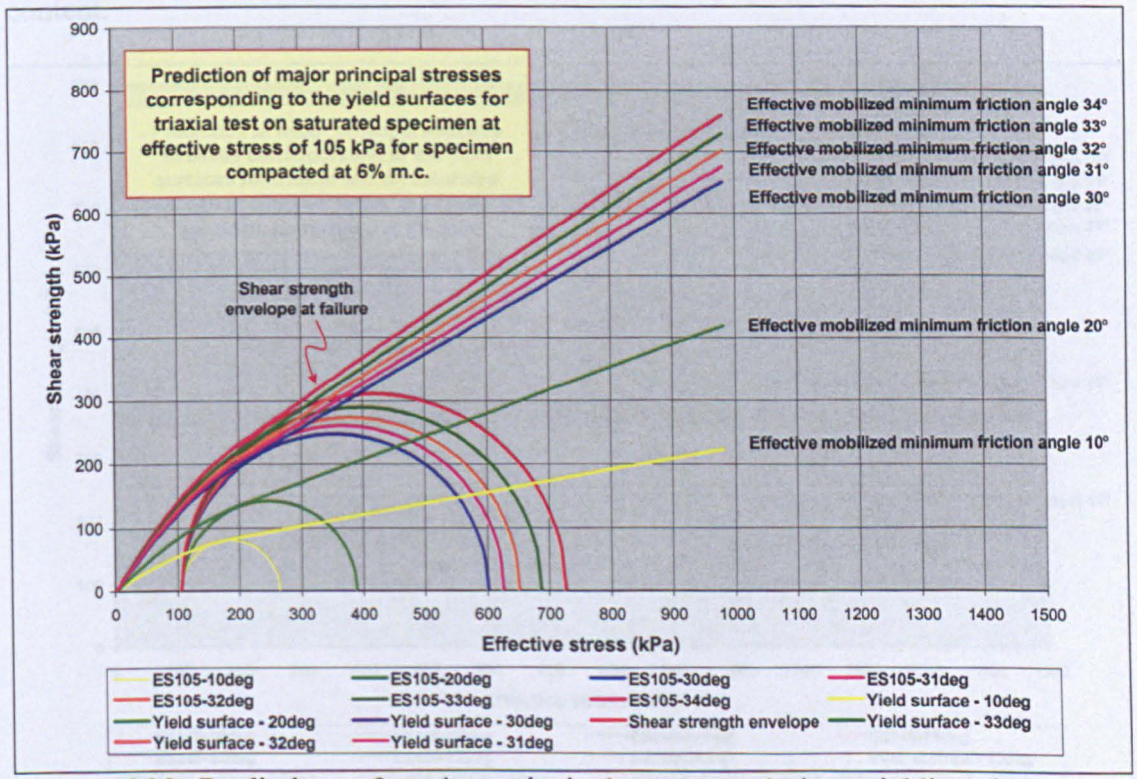

Figure 6.39 Prediction of major principal stresses during yielding in triaxial compression test at effective stress 105 kPa for specimen compacted at 6% moisture content.

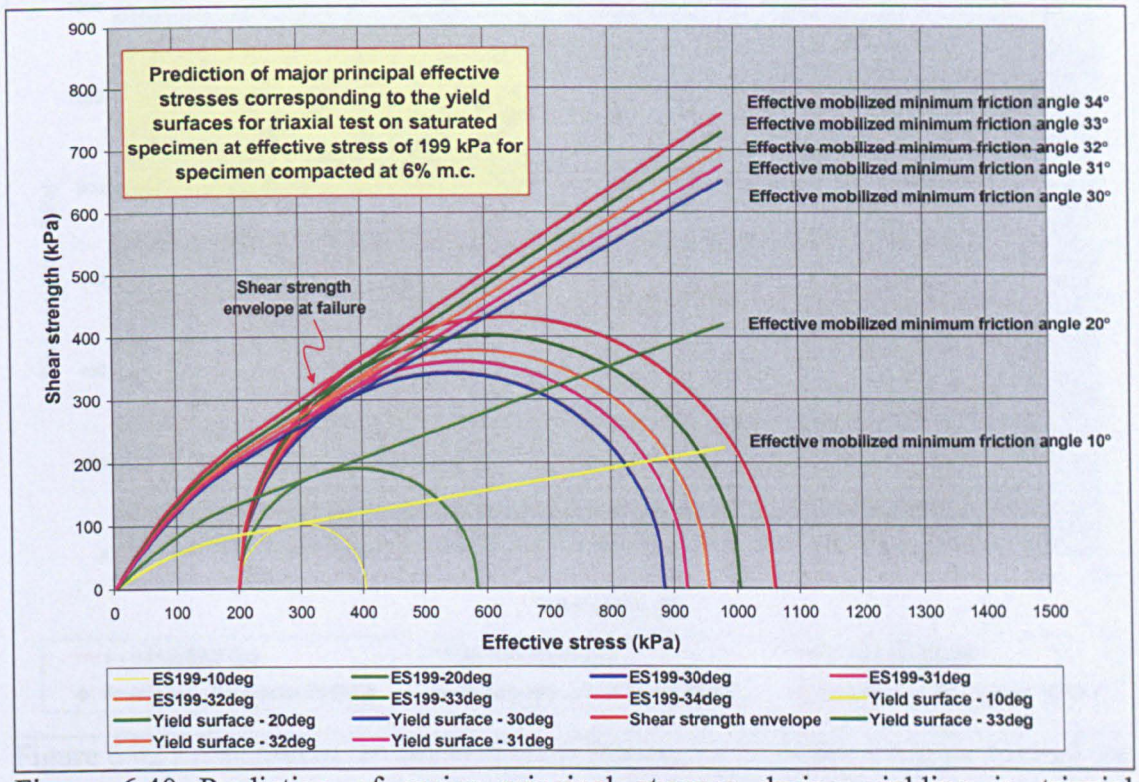

Figure 6.40 Prediction of major principal stresses during yielding in triaxial compression test at effective stress 199 kPa for specimen compacted at 6% moisture content.

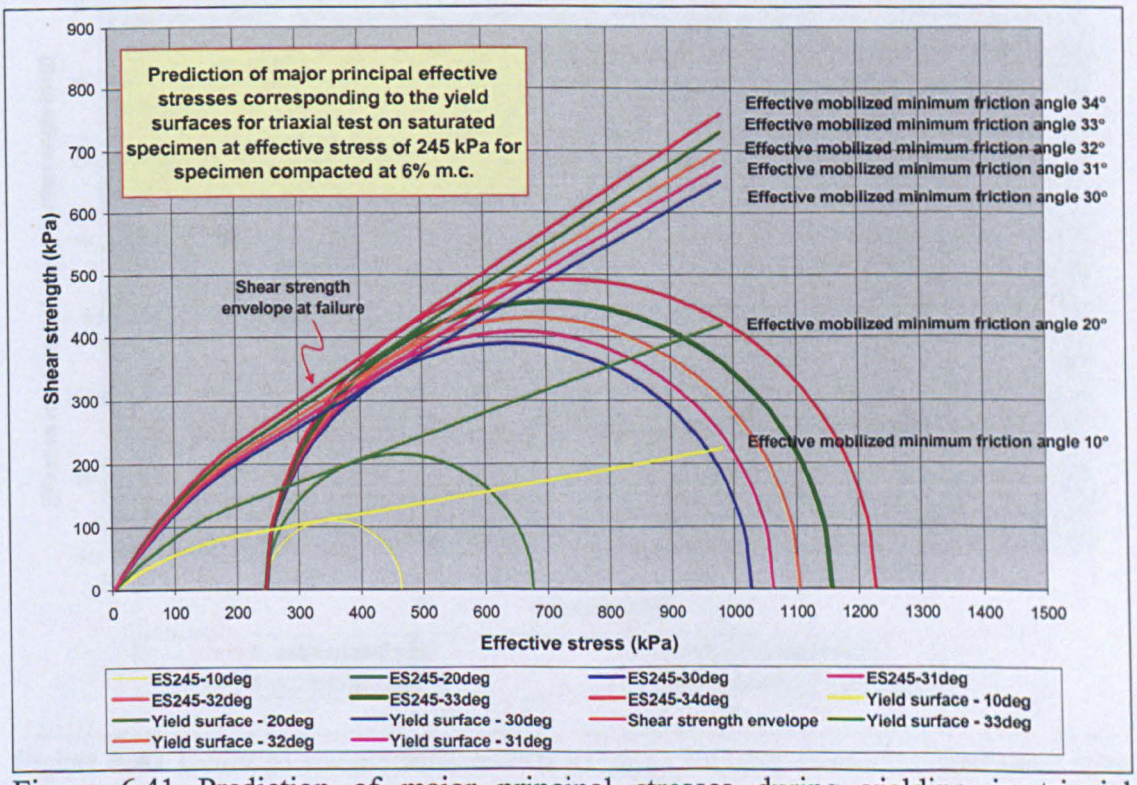

Figure 6.41 Prediction of major principal stresses during yielding in triaxial compression test at effective stress 245 kPa for specimen compacted at 6% moisture content.

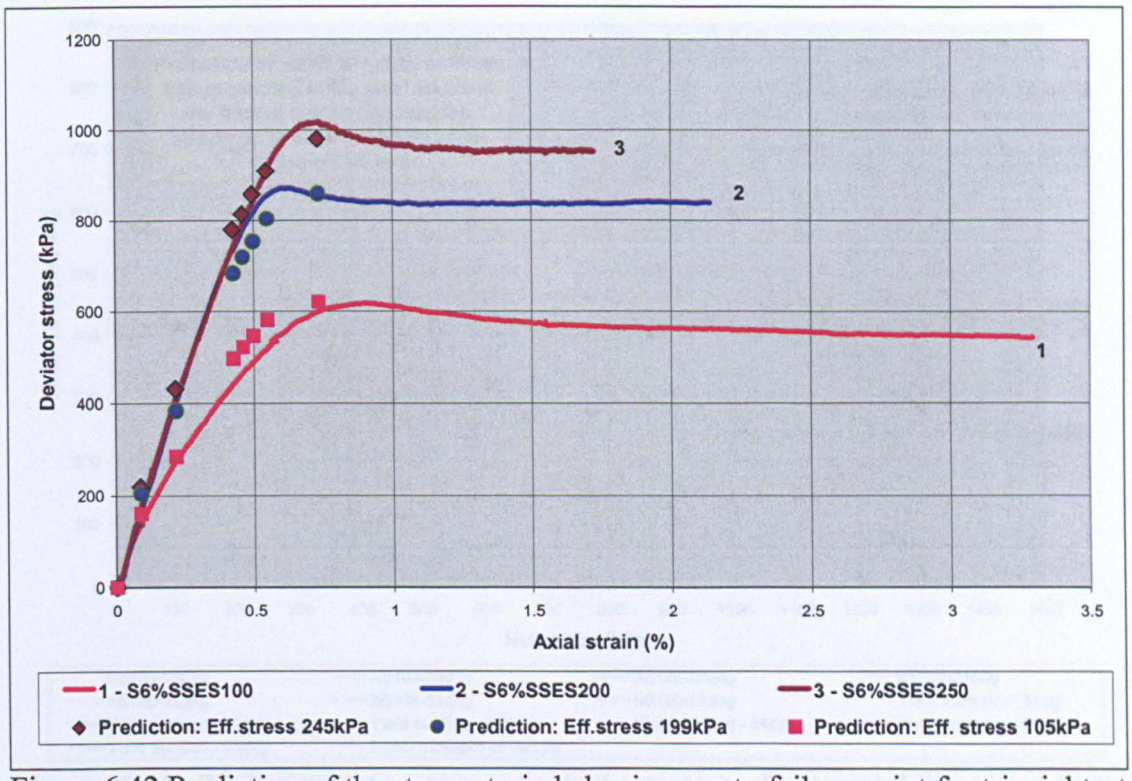

Figure 6.42 Prediction of the stress-strain behaviour up to failure point for triaxial test on saturated specimens compacted at 6% moisture content at effective stresses of 105, 199 and 245 kPa.

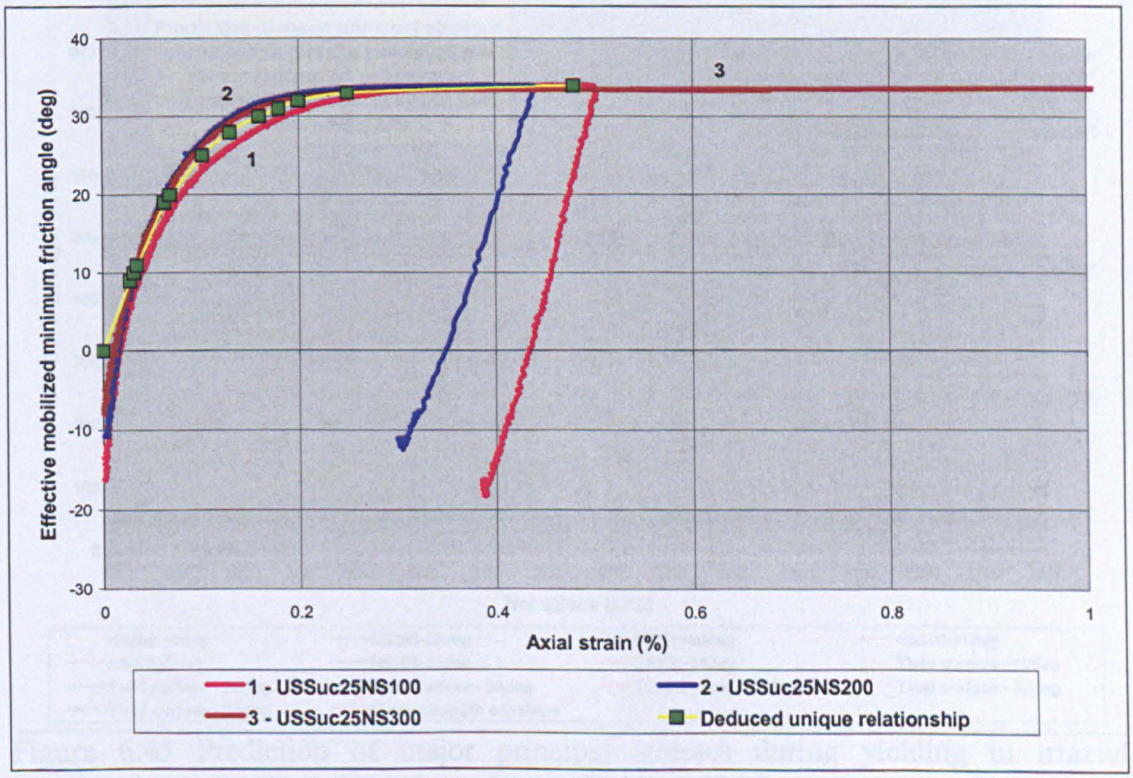

Figure 6.43 Deduced unique relationship of $\phi'_{\min_{mob}}$ - ε_a for triaxial compression tests on unsaturated specimens at suction of 25 kPa.

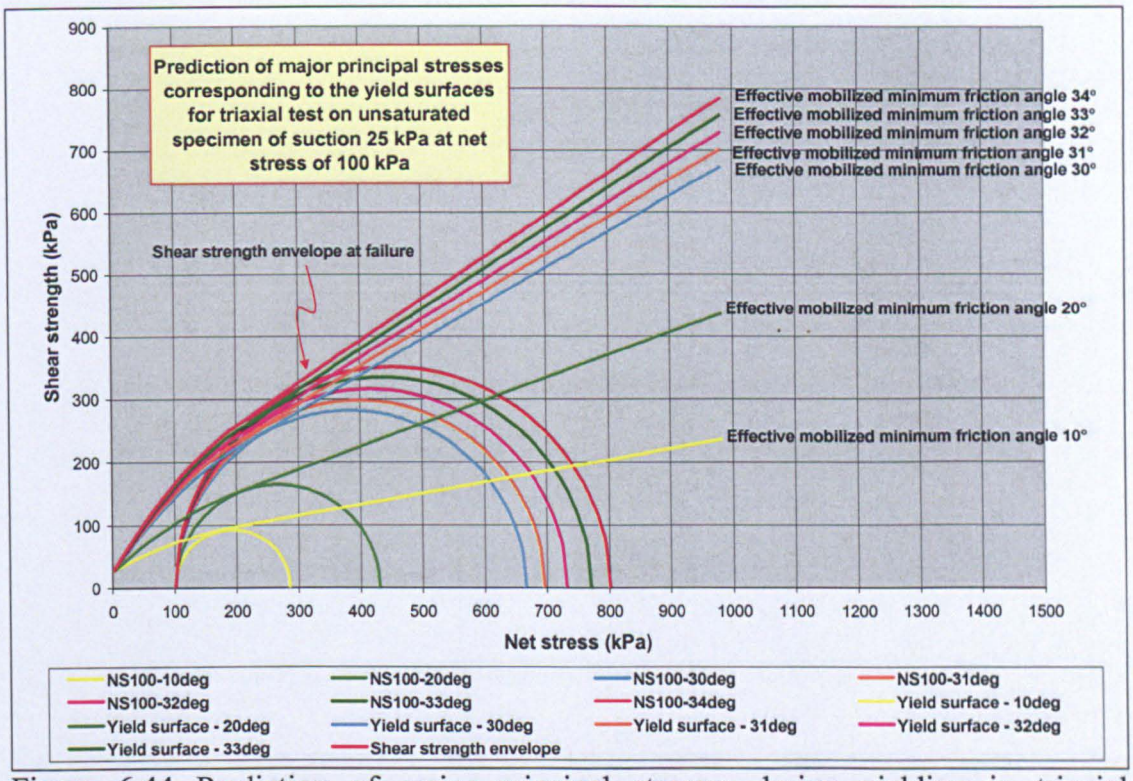

Figure 6.44 Prediction of major principal stresses during yielding in triaxial compression test on unsaturated specimen of suction 25 kPa at net stress of 100 kPa.

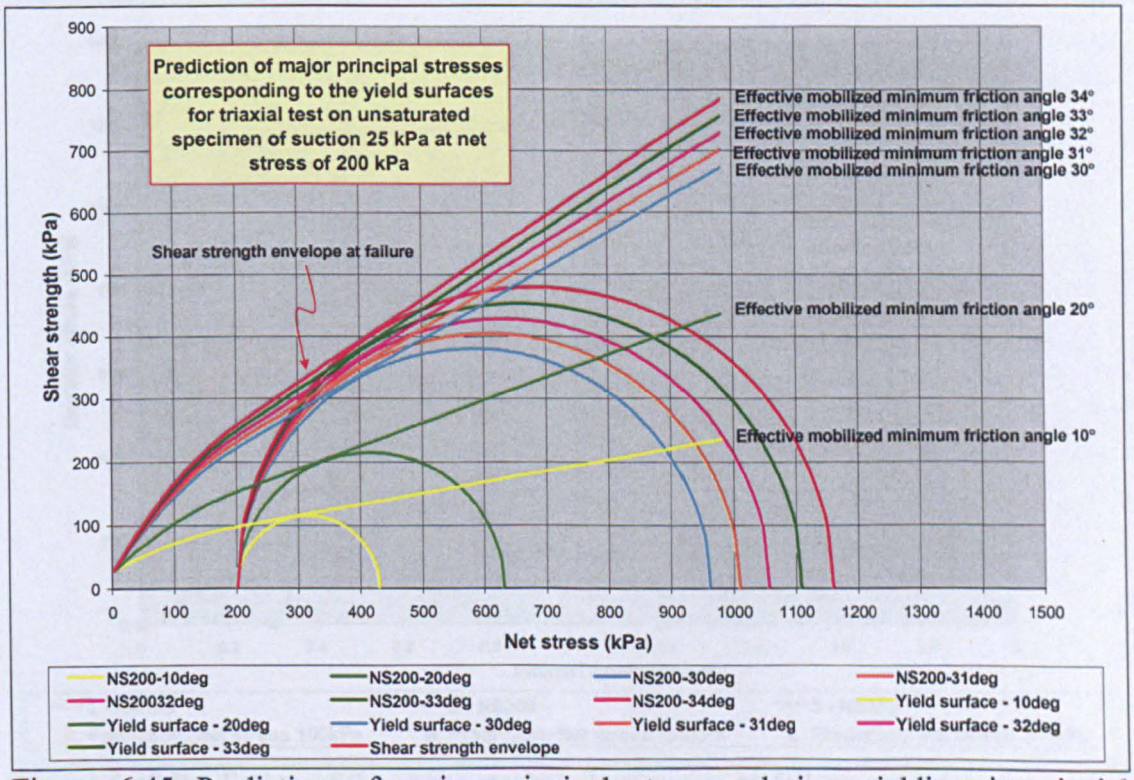

Figure 6.45 Prediction of major principal stresses during yielding in triaxial compression test on unsaturated specimen of suction 25 kPa at net stress of 200 kPa.

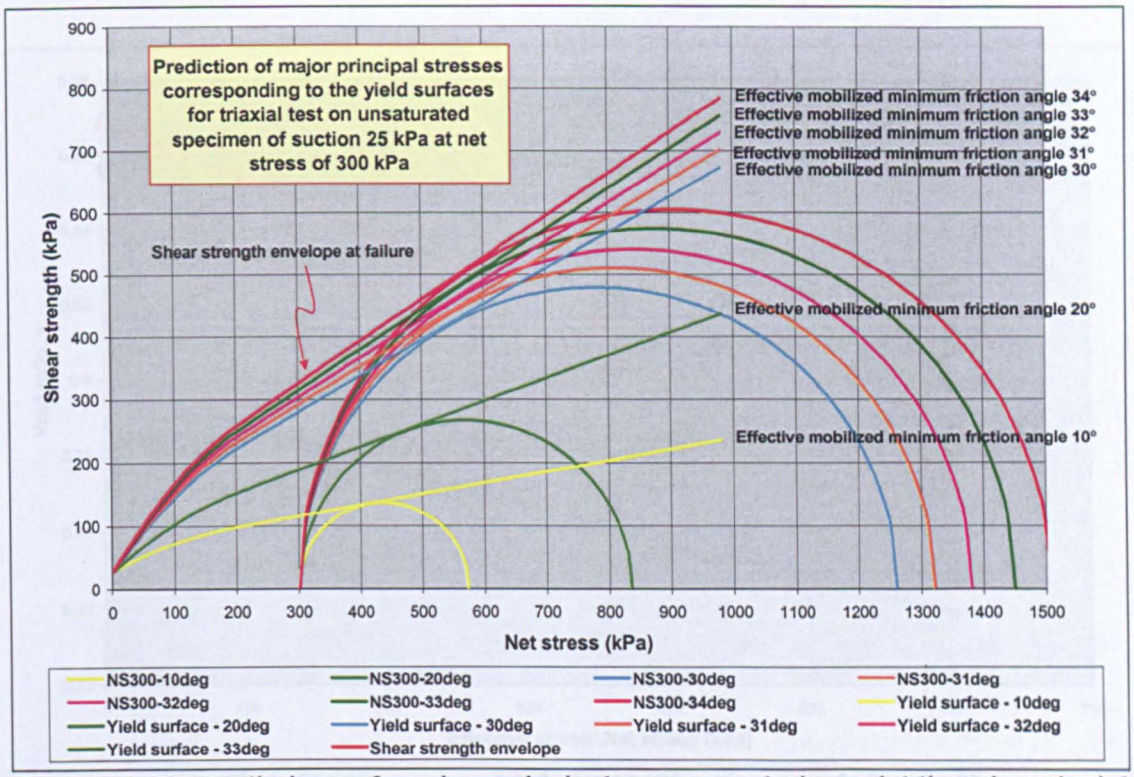

Figure 6.46 Prediction of major principal stresses during yielding in triaxial compression test on unsaturated specimen of suction 25 kPa at net stress of 300 kPa.

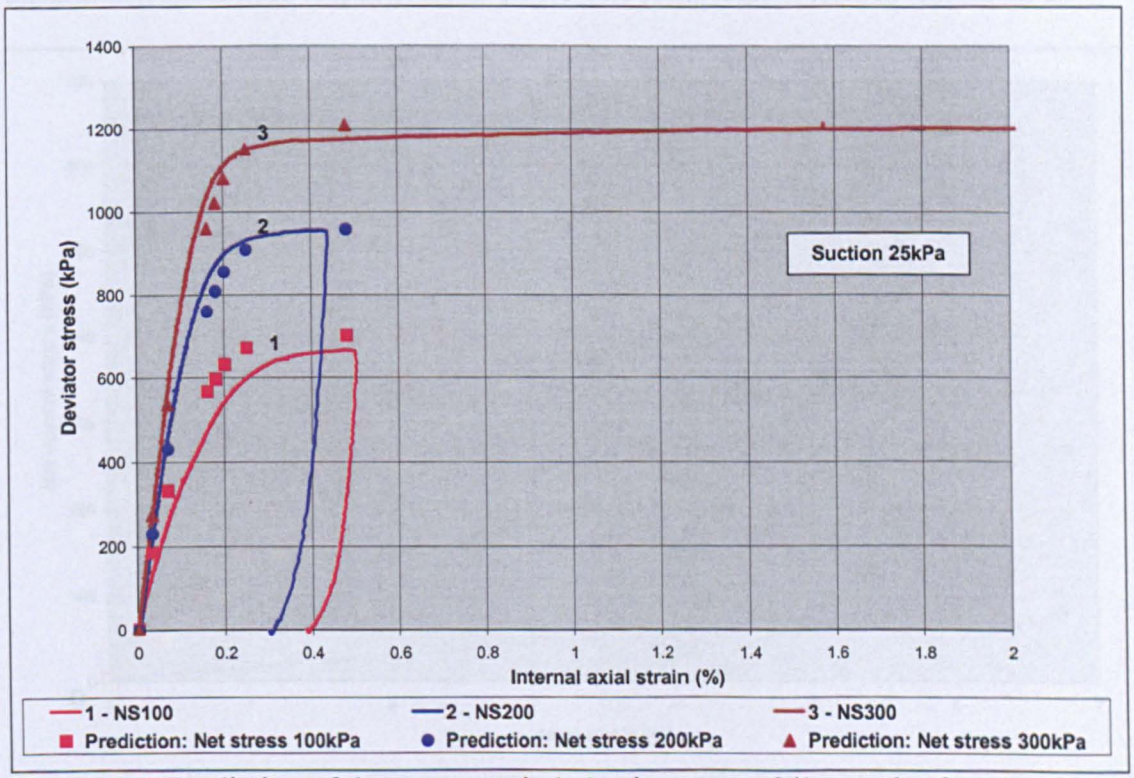

Figure 6.47 Prediction of the stress-strain behaviour up to failure point for triaxial test on unsaturated specimens of suction 25 kPa at net stresses of 100, 200 and 300 kPa.

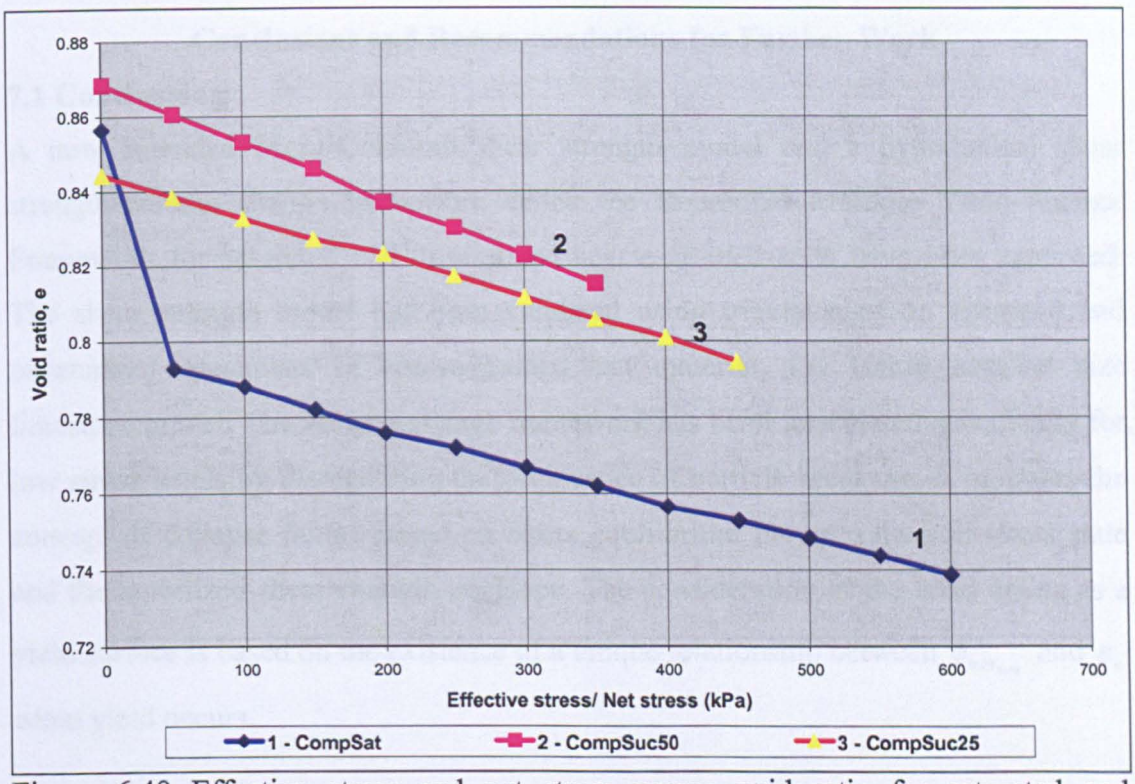

Figure 6.48 Effective stress and net stress versus void ratio for saturated and unsaturated specimens respectively in Rowe cell compression tests in test series E.

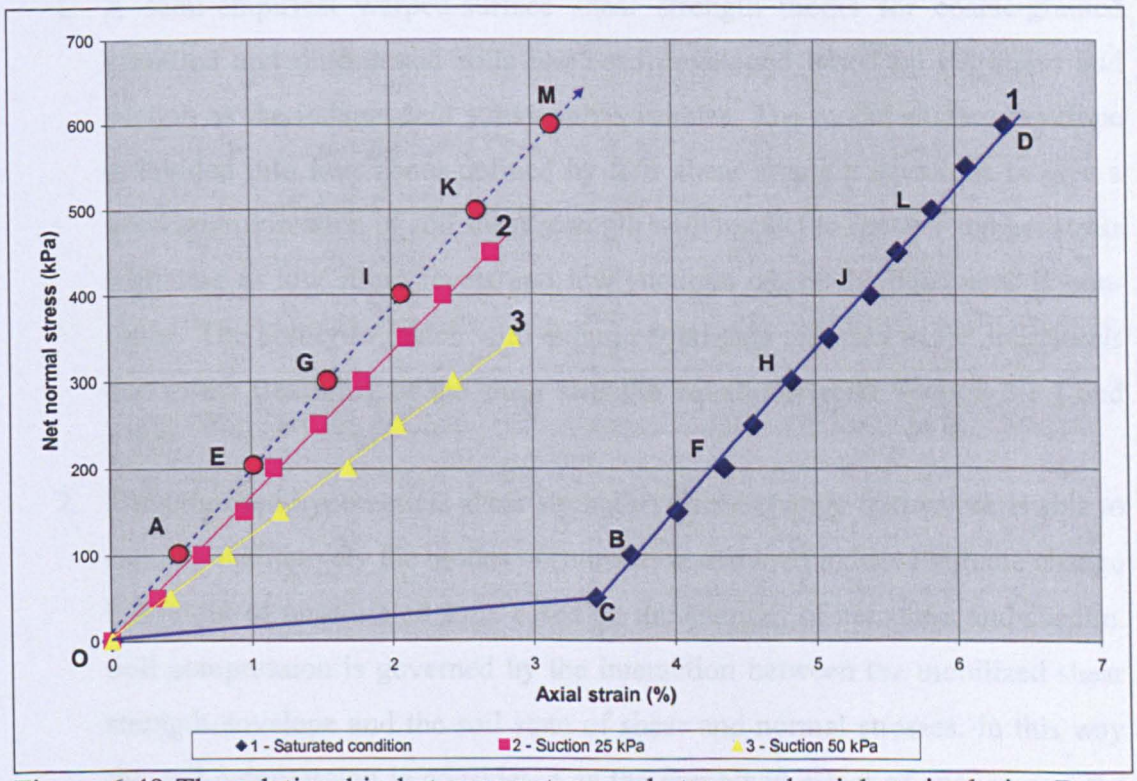

Figure 6.49 The relationship between net normal stress and axial strain during Rowe cell compression tests on saturated and unsaturated specimens.

Chapter 7

Conclusions and Recommendations for Further Work

7.1 Conclusions.

A new extended Mohr-Coulomb shear strength model and a hypothetical shear strength-volume change framework called the Rotational Multiple Yield Surface Framework for saturated and unsaturated coarse-grained soils have been proposed. The shear strength model has been validated using triaxial tests on saturated and unsaturated specimens of coarse-grained test material, i.e. 10mm nominal size limestone gravel. The volume change framework has been formulated specifically for low stress levels by disregarding the occurrence of particle breakage. It proposes the concept of collapse failure based on stress equilibrium between the soil stress state and the mobilized shear strength envelope. The consideration of the latter acting as a yield surface is based on the existence of a unique relationship between $\phi'_{\min_{mob}}$ and ε_a when yield occurs.

The following summarise the main conclusions of the work:

1. A semi-empirical warped-surface shear strength model for coarse-grained saturated and unsaturated soils has been developed based on net stress and suction as the independent stress state variables. The model surface envelope is divided into four zones defined by four shear strength equations to give a good approximation of soil shear strength with respect to suction and net stress including at low stress levels and low suctions where the behaviour is non-linear. The ability to match with experimental data reported in the literatureis due to the flexibility of the shear strength equations (refer Section 3.3.1 and 3.3.2).
2. The proposed hypothetical shear strength-volume change framework is able to explain qualitatively the modes of inundation and load induced volume change behaviour of unsaturated soils based on the changes of net stress and suction. Soil compression is governed by the interaction between the mobilized shear strength envelope and the soil state of shear and normal stresses. In this way the soil compression is considered as the combined effect of suction and the principal stresses. The applicability of the volume change framework relies on the existence of a unique relationship between $\phi'_{\min_{mob}}$ and ε_a at failure for low

stress levels. Qualitatively the framework is able to model loading and wetting collapse volume change behaviour, and include the significant volume change that occurs near saturation. The volume change framework showed that collapse due to inundation is chiefly governed by the steep drop in shear strength towards zero suction (refer Section 3.4.4 and 3.4.5).

3. The soil-moisture characteristic curve of the test material showed that the value of residual suction, $(u_a - u_w)_r$, is 15kPa, which is a very low value and is in accordance with the findings that residual suction decreases as the grain size increases (refer Section 5.1).
4. Triaxial tests on saturated specimens confirmed that the shape of the shear strength envelope relative to effective stress for the test material at saturation is curvilinear similar to the behaviour of coarse-grained soils reported in the literature. It behaves linearly with respect to effective stress at higher confining pressures and curves down to the origin as the confining pressure reduces to zero. This result verifies the shear strength behaviour at saturation according to the proposed warped-surface shear strength model (refer Section 6.7.1). Triaxial tests on the unsaturated specimens showed that the envelopes at various suctions are slightly higher than those of the saturated specimens. This confirms that the extra shear strength in the unsaturated specimens is due to the presence of suction. In addition, shear strength decreases when suction increases from residual suction and the decrease becomes gradual at higher net stress (refer Section 6.7.2).
5. The combination of the results of triaxial tests on saturated and unsaturated specimens is able to match closely with the proposed semi-empirical shear strength model and thereby demonstrate that the model may be usefully applied to coarse-grained soils (refer Section 6.7.3).
6. The results of the triaxial tests on saturated and unsaturated specimens of a coarse-grained soil have suggested the existence of a unique relationship of $\phi'_{\min_{mob}} - \varepsilon_a$ during the soil compression up to the shear strength at failure that occur at similar axial strain (refer to Section 6.8.2). This type of soil compression is categorised as loading collapse. Therefore the results of the triaxial tests on saturated and unsaturated specimens support the applicability of the hypothetical Rotational Multiple Yield Surface Framework in

explaining the mode of loading collapse in coarse-grained soils (refer Section 6.8.1). However there is no data in this research that can prove its applicability for the wetting collapse loading condition.

7. Particle breakage causes the dispersion in the graphs of $\phi^{'}_{\min_{mob}} - \varepsilon_a$ at different net confining stresses and therefore the unique relationship between $\phi^{'}_{\min_{mob}}$ and ε_a no longer holds. This restricts the application of the proposed hypothetical volume change framework to cases of low stress levels only where particle breakage is very unlikely (refer Section 6.8.3).
8. Rowe cell compression tests have indicated a linear behaviour between effective stress and axial strain for a saturated specimen and a linear behaviour between net stress and axial strain for unsaturated specimens, similar to the findings by the previous researchers. (refer Section 6.8.4).

7.2 Recommendations for Further Work.

As the proposed semi-empirical shear strength model is new, more work is needed to prove the diversity of its applicability. Some suggestions for future work are noted below:

1. More testing is required to explore the applicability of the proposed semi-empirical shear strength model to different grain size material with triaxial tests being carried out on both saturated and unsaturated specimens. Using a smaller specimen size may be appropriate for finer soils which will speed up the time for equalization and thus the time for the whole test.
2. The variation of ultimate suction with respect to net stress needs further study. The linear variation in the proposed shear strength model seems to fit with the test material, but its behaviour for different types of coarse-grained soil needs to be investigated.
3. To test the applicability of the proposed new shear strength model for fine grained soils requires a complete validation by conducting shear strength tests on both saturated and unsaturated specimens of such materials.

The Rotational Multiple Yield Surface Framework requires further work in order to prove its applicability for wetting collapse conditions. Some suggestions for future work are noted below:

1. In order to prove the applicability of the volume change framework on wetting collapse condition triaxial test on unsaturated specimens need to be inundated at some stage during the application of the deviator stress. The inundation axial compression should correspondingly indicate the increase in the mobilized shear strength under constant deviator stress. The resultant stress-strain curve should be similar to the unloading and reloading path described in Section 2.3.1 except that the continuation of the stress-stress curve should resume at the point slightly higher than the deviator stress at which it was inundated. This is to verify that inundation soil compression has also elevated the mobilized shear strength in accordance to the concept of wetting collapse adopted in the volume change framework.
2. Simulation of wetting collapse in triaxial compression tests at identical suction for different net confining stresses is anticipated to cause identical axial compression. This is because according to the proposed volume change framework the magnitude of wetting collapse is independent of the net confining stress when suction is constant. This is because the rotation of the yield surface envelope must be identical irrespective of its position along the net stress axis when the Mohr stress circle is moved from the position representing unsaturated condition to the net stress axis when the condition is being saturated.
3. Further triaxial tests on saturated and unsaturated specimens of different material are required to check the validity of the framework's assumption that the $\phi^{'}_{\min_{mob}} - \varepsilon_a$ relationship is unique for low stress levels. This is to test the applicability of the framework on different materials.
4. Further Rowe cell compression tests with lateral pressure measurement are required in order to establish the existence of the unique relationship of $\phi^{'}_{\min_{mob}} - \varepsilon_a$ for both loading and wetting collapse stress conditions for 1-D soil compression.
5. More 1-D compression tests are required at different suctions in order to understand the volume change behaviour with respect to suction. The gradient of the linear variation of void ratio with respect to net normal stress may be changing in a unique manner as suction changes, or may be constant irrespective of the suction values.

6. Further work is required in order to understand the effect of particle breakage on the stress-strain behaviour. This may lead to the modification of the Rotational Multiple Yield Surface Framework to accommodate the effects of particle breakage and thus allow application at higher stress levels.
7. The effect of breakage on the graph of mobilized friction angle relative to void ratio is a potential technique for detecting particle breakage and more work is needed in order to establish the technique.

References:

Aitchison, G. D. (1961). "Relationship of moisture and effective stress functions in unsaturated soils." *Proceedings of the Pore Pressure and Suction in Soils Conference.*, London, England: 47-52.

Alonso, E. E., Gens, A., and Hight, D. W. (1987). "General Report: Special problem soils." *Proceedings of the 9th. European Conference on Soil Mechanics and Foundation Engineering.*, 3, Dublin: 1087-1146.

Alonso, E. E., Gens, A., and Josa, A. (1990). "A constitutive model for partially saturated soil." *Geotechnique*, 40(3), 405-430

Alonso, E. E., Lloret, A., Gens, A., and Yang, D. Q. (1995). "Experimental behaviour of highly expansive double-structure clay." *Proceedings of the 1st. International Conference on Unsaturated Soils*, 1, Paris: 11 - 16.

Anderson, W. F., Goodwin, A. K., Pyrah, I. C., and Salman, T. H. (1997). "Equipment for One-Dimensional Compression and Triaxial Testing of Unsaturated Granular Soils at Low Stress Levels." *ASTM Geotechnical Testing Journal*, 20(1), 74 - 89.

ASTM D2325-68. (1985). "Standard Test Method for Capillary-Moisture Relationships for Coarse and Medium Textured Soils by Porous Plate Apparatus." *Annual Book of ASTM Standards; Soil and Rock, Building Stones*, 4(8), 363-369.

Atkinson, J. H. (1975). "Anisotropic elastic deformations in laboratory tests on undisturbed London Clay." *Geotechnique*, 25(2), 357-374.

Baldi, G., and Nova, R. (1984). "Membrane penetration effects in triaxial testing." *Journal of Geotechnical Engineering*, 110(3), 403-420.

Barden, L., Madedor, A. O., and Sides, G. R. (1969). "Volume Change Characteristics of Unsaturated Clay." *Journal Soil Mechanics Foundation Engineering, ASCE.*, 95, 33-52.

Basma, A. A., and Tuncer, E. R. (1992). "Evaluation and control of collapsible soils." *Journal of Geotechnical Engineering.*, 118(10), 1491-1504.

Billam, J. (1972). "Some aspects of the behaviour of granular materials at high pressures." *Proceedings of the Roscoe Memorial Symposium, Cambridge University, March 1971.*

Bishop, A. W. (1959). "The principle of effective stress." *Teknisk Ukeblad*, 106(39), 859-863.

Bishop, A. W. (1966). "The strength of soils as engineering materials." *Geotechnique*, 16(2), 91-130.

Bishop, A. W. (1972). "Shear strength parameters of undisturbed and remoulded soil specimens." *Proceedings of the Roscoe Memorial Symposium, Cambridge University, March 1971.*

Bishop, A. W., Alpan, I., Blight, G. E., and Donald, I. B. (1960). "Factors Controlling the Shear Strength of Partly Saturated Cohesive Soils." *ASCE Res. Conference Shear Strength of Cohesive Soils*, University of Colorado, Boulder: 503-532.

Bishop, A. W., and Blight, G. E. (1963). "Some aspects of effective stress in saturated and unsaturated soils." *Geotechnique*, 13(3), 177-197.

Bishop, A. W., and Donald, I. B. (1961). "The Experimental Study of Partly Saturated Soil in the Triaxial Apparatus." *Proceedings of the 5th. International Conference Soil Mechanics and Foundation Engineering.*, 1, Paris, France: 13-21.

Blanchfield, R., and Anderson, W. F. (2000). "Wetting collapse in opencast coalmine backfill." *Proceedings of the ICE Geotechnical Engineering*, London: 139-149.

Brackley, I. J. A. (1971). "Partial Collapse in Unsaturated Expansive Clay." *Proceedings of the 5th Reg. Conference Soil Mechanics Foundation Engineering*, South Africa: 23-30.

Brandon, T. L., Duncan, J. M., and Gardner, W. S. (1990). "Hydrocompression settlement of deep fills." *Journal of Geotechnical Engineering*, 116(10), 1536 - 1548.

Burland, J. B. (1964). "Effective Stresses in Partly Saturated Soils." discussion of "Some Aspects of Effective Stress in Saturated and Partly Saturated Soils." by G.E.Blight and A.W.Bishop." *Geotechnique*, 14, 65-68.

Burland, J. B. (1965). "Some aspects of the mechanical behaviour of partly saturated soils." *Moisture Equilibria and Moisture Changes in the Soils Beneath Covered Areas, A Symp. in Print.*, Australia: 270-278.

Callisto, L., and Calabresi, G. (1998). "Mechanical behaviour of a natural soft clay." *Geotechnique*, 48(4), 495-513.

Charles, J. A., and Watts, K. S. (1980). "The influence of confining pressure on the shear strength of compacted rockfill." *Geotechnique*, 30(4), 353-367.

Cox, D. W. (1978). "Volume change of compacted clay fill." *Proceedings of a Conference on Clay Fills, Institution of Civil Engineers, London*, 79 - 86.

Croney, D., Coleman, J. D., and Black, W. P. M. (1958). "Movement and Distribution of Water in Soil in Relation to Highway Design and Performance." *Water and Its Conduction in Soils, Highway Res. Board, Special Report, Washington, DC*, 40, 226-252.

Delage, P., and Graham, J. (1995). "Understanding the behaviour of unsaturated soils requires reliable conceptual models. State-of-art report, session 1, soil properties." *Proceedings of the 1st Int. Conference on Unsaturated Soils, Paris*, 3, 1223-1256.

Delage, P., Suraj de Silva, G. P. R., and De Laure, E. (1987). "Un nouvel appareil triaxial pour les sols non-satures." *9th. European Conference on Soil Mechanics and Foundation Engineering.*, 1, 25-28.

Escario, V., and Juca, J. (1989). "Strength and deformation of partly saturated soils." *Proccedings of the 12th. International Conference on Soil Mechanics and Foundation Engineering.*, Rio de Janeiro: 3, 43-46.

Escario, V., and Saez, J. (1973). "Measurements of the properties of swelling and collapsing soils under controlled suctions." *Proceedings of the 3rd International Conference on Expansive soils.*, Haifa, Israel: 1, 195-200.

Escario, V., and Saez, J. (1986). "The shear strength of partly saturated soils." *Geotechnique*, 36(3), 453-456.

Fair, P. (2004). "The geotechnical behaviour of ballast materials for railway track maintainence," Ph.D. Thesis, University of Sheffield.

Feda, J. (1988). "Collapse of loess upon wetting." *Engineering Geology*, 25, 263-269.

Fredlund, D. G. (2000). "The 1999 R.M. Hardy Lecture: The implementation of unsaturated soil mechanics into geotechnical engineering." *Canadian Geotechnical Journal*, 37, 963-986.

Fredlund, D. G., and Morgenstern, N. R. (1976). "Constitutive relations for volume change in unsaturated soils." *Canadian Geotechnical Journal*, 13(3), 261-276.

Fredlund, D. G., and Morgenstern, N. R. (1977). "Stress state variables for unsaturated soils." *Journal of the Soil Mechanics and Foundations Division, ASCE*, 103(GT5), 447-466.

Fredlund, D. G., and Rahardjo, H. (1993). *Soil Mechanics for unsaturated soils.*, John Wiley and son.

Fredlund, D. G., and Xing, A. (1994). "Equations for the soil-water characteristic curve." *Canadian Geotechnical Journal*, 31(4), 533-546.

Fredlund, D. G., Morgenstern, N. R., and Widger, R. A. (1978). "Shear Strength of Unsaturated Soils." *Canadian Geotechnical Journal*, 15(3), 313-321.

Fredlund, D. G., Rahardjo, H., and Gan, J. K. M. (1987). "Non-linearity of strength envelope for unsaturated soils." *Proceedings of the 6th. International Conference on Expansive Soils.*, New Delhi : 49-54.

Fredlund, D. G., Xing, A., Fredlund, M. D., and Barbour, S. L. (1995). "The relationship of the unsaturated soil shear strength to the soil-water characteristic curve." *Canadian Geotechnical Journal*, 33(3), 440-448.

Futai, M. M., and Almeida, M. S. S. (2005). "An experimental investigation of the mechanical behaviour of an unsaturated gneiss residual soil." *Geotechnique*, 55(3), 201-213.

Gallipoli, D., Gens, A., Sharma, R. S., and Vaunat, J. (2003). "An elasto-plastic model for unsaturated soil incorporating the effects of matric suction and degree of saturation on mechanical behaviour." *Geotechnique*, 53(1), 123-135.

Gallipoli, D., Gens, A., Sharma, R. S., and Vaunat, J. (2003). "An elasto-plastic model for unsaturated soil incorporating the effects of matric suction and degree of saturation on mechanical behaviour." *Geotechnique*, 53(1), 123-135.

Gan, J. K. M., and Fredlund, D. G. (1988). "Multistage direct shear testing of unsaturated soil." *ASTM, Geotechnical Testing Journal.*, 11(2), 132-138.

Gan, J. K. M., and Fredlund, D. G. (1996). "Shear strength characteristics of two saprolitic soils." *Canadian Geotechnical Journal*, 33, 595-609.

Gan, J. K. M., Fredlund, D. G., and Rahardjo, H. (1988). "Determination of the Shear Strength Parameters of an Unsaturated Soil Using the Direct Shear Test." *Canadian Geotechnical Journal*, 25(No.3), 500-510.

Gens, A., and Alonso, E. E. (1992). "A framework for the behaviour of unsaturated expansive clays." *Canadian Geotechnical Journal*, 29(6), 1013-1032.

Goodwin, A. K. (1991). "One dimensional compression behaviour of unsaturated granular soils at low stress level." Ph.D., University of Sheffield.

Head, K. H. (1981). *Manual of Soil Laboratory Testing*, Pentech Press, London.

Hilf, J. W. (1956). "An investigation of pore-water pressure in compacted cohesive soils." United States Bureau of Reclamation, Denver.

Ho, D. Y. F., and Fredlund, D. G. (1982). "A Multistage Triaxial Test for Unsaturated Soils." *ASTM Geotechnical Testing Journal.*, 5(1/2), 18-25.

Indraratna, B., and Salim, W. (2001). "Shear strength and degradation characteristics of railway ballast." *Proc. 4th. Southeast Asian Geotechnical Conference*, Hong Kong., Vol.1, 521-526.

Indraratna, B., Wijewardena, L. S. S., and Balasubramaniam, A. S. (1993). "Large-scale triaxial testing of greywacke rockfill." *Geotechnique*, 43(1), 37-51.

Jaky, J. (1948). "Pressures in soils." *Proc. 2nd. International Conference Soil Mechanics, Rotterdam.*, Vol. 1, 103-107.

Jennings, J. E. and J. B. Burland (1962). "Limitations to the use of effective stresses partly saturated soils." *Geotechnique*, 12(No.2): pp.125-144.

Josa, A., Balmaceda, A., Gens, A., and Alonso, E. E. (1992). "An elasto-plastic model for partially saturated soils exhibiting a maximum of collapse." *Int. Conference on Computational Plasticity.*, Barcelona, Spain.

Jovicic, V., and Coop, M. R. (1997). "Stiffness of coarse-grained soils at small strains." *Geotechnique*, 47(3), 545-561.

Kirkpatrick, W. M., and D.J.Belshaw. (1968). "On the interpretation of the triaxail test." *Geotechnique*, 18(3), 336-350.

Kirkpatrick, W. M., and J.S.Younger. (1970). "Strain conditions in compression cylinder." *JSMFD, ASCE*, 96(SM5), 1683-1695.

Koorevaar, P., Menelik, G., and Dirksen, C. (1983). "Elements of Soil Physics." *Amsterdam, The Netherlands*, 228.

Kramer, S. L., Sivaneswaran, N., and Davis, R. O. (1990). "Analysis of membrane penetration in triaxial test." *JEM, ASCE*, 116(4), 773-789.

Lloret, A., and Alonso, E. E. (1980). "Consolidation of Unsaturated Soils Including Swelling and Collapse Behaviour." *Geotechnique*, 30(4), 449-477.

Lloret, A., and Alonso, E. E. (1985). "State Surfaces for Partially Saturated Soils." *Proceedings of the 11th Int. Conference Soil Mechanics Foundation Engineering*, San Francisco: 2, 557-562.

Mahalinga-Iyer, U., and Williams, D. J. (1995). "Unsaturated strength behaviour of compacted lateritic soils." *Geotechnique*, 45(2), 317-320.

Maswoswe, J. (1985). "Stress Paths for a Compacted Soil During Collapse due to Wetting," Ph.D. Thesis, Imperial College, London.

Matyas, E. L., and Radhakrishna, H. S. (1968). "Volume change characteristics of partially saturated soils." *Geotechnique*, 18(4), 432-448.

Molenkamp, F., and Luger, H. J. (1981). "Modelling and minimization of membrane penetration effects in tests on granular soils." *Geotechnique*, 31(4), 471-486.

Morgenstern, N. R. (1979). "Properties of Compacted Soils." *Contibution to Panel Discussion, Session IV, Proceding of the 6th Panamerican Conference Soil Mechanics Foundation Engineering*, Lima, Peru: 3, 349-354.

Nishimura, T., and Fredlund, D. G. (2000). "Relationship between shear strength and matric suction in an unsaturated silty soil." *Proceedings for the Unsaturated Soil for Asia.*, Singapore: 563 - 568

Penumadu, D., and Dean, J. (2000). "Compressibility effect in evaluating the pore-size distribution of kaolin clay using mercury intrusion porosimetry." *Canadian Geotechnical Journal*, 37(2).

Powrie, W. (1997). *Soil mechanics; concepts and applications*, SPON PRESS, Oxford, Great Britain.

Rahardjo, H., and Fredlund, D. G. (1993). "Stress paths for shear strength testing of unsaturated soils." *Proceedings 11th Southeast Asia Geotechnical Conference, Singapore*

Rahardjo, H., and Fredlund, D. G. (2003). "Ko - Volume change characteristics of an unsaturated soil with respect to various loading paths." *Geotechnical Testing Journal*, 26(1).

Rassam, D. W., and Williams, D. J. (1999). "Relationship describing the shear strength of unsaturated soils." *Canadian Geotechnical Journal*, 32(2), 363-368.

Richards, B. G. (1966). "The significance of moisture flow and equilibra in unsaturated soils in relation to the design of engineering structures built on shallow foundations in Australia." *Symposium on Permeability on Capillary, ASTM.*

Sabbagh, A. (2000). "The lateral swelling pressure on the volumetric behaviour of natural expansive soils deposits." *Proceedings for the Unsaturated Soil for Asia*, Singapore: 709 - 714.

Salman, T. H. (1995). "Triaxial behaviour of partially saturated granular soils at low stress levels.," Ph.D., University of Sheffield, Sheffield.

Sharma, R. S. (1998). "Mechanical behaviour of unsaturated highly expansive clays.," Ph.D. Thesis, University of Oxford, UK.

Skempton, A. W. (1961). "Effective Stress in Soils, Concrete and Rocks." *Proceedings Conference Pore Pressure*, London(Butterworths), 4-16.

Tadepalli, R., Rahardjo, H., and Fredlund, D. G. (1992). "Measurement of matric suction and volume change during inundation of collapsible soil." *ASTM Geotechnical Testing Journal*, 15(2), 115 - 122.

Taha, M. R., Hossain, M. K., and Mofiz, S. A. "Shear strength behaviour of unsaturated granite residual soil." *Proceedings for the Unsaturated soil for Asia*, Singapore: 575 - 580.

Tang, G. X., and Graham, J. (2002). "A possible elastic-plastic framework for unsaturated soils with high-plasticity." *Canadian Geotechnical Journal*, 39, 894-907.

Tang, G. X., and Graham, J. (2002). "A possible elastic-plastic framework for unsaturated soils with high-plasticity." *Canadian Geotechnical Journal*, 39, 894-907.

Terzaghi, K. (1936). "The shear resistance of saturated soils." *Proceedings for the 1st. International Conference on Soil Mechanics and Foundation Engineering (Cambridge, MA)*, 1, 54 - 56.

Terzaghi, K. (1943). Theoretical soil mechanics, New York, Wiley Publications.

Ting, C. M. R., Sills, G. C., and Wijeyesekera, D. C. (1994). "Development of K_o in soft soils." *Geotechnique*, 44(1), 101-109.

Toll, D. G. (1990). "A framework for unsaturated soil behaviour." *Geotechnique*, 40(1), 31-44.

Toll, D. G., Ong, B. H., and Raharjo, H. (2000). "Triaxial testing of unsaturated samples of undisturbed residual soil from Singapore." *Proceedings of the Unsaturated soil for Asia.*, Singapore: 581-586.

Ueng, T. S., and Chen, T. J. (2000). "Energy aspects of particle breakage in drained shear of sands." *Geotechnique*, Vol.50(1), 65-72.

Vanapalli, S. K., Fredlund, D. G., Pufahl, D. E., and Clifton, A. W. (1996). "Model for the prediction of shear strength with respect to soil suction." *Canadian Geotechnical Journal*, 33(3), 379-392.

Vanapalli, S. K., Sillers, W. S., and Fredlund, M. D. (1998). "The meaning and relevance of residual state to unsaturated soils." *51st Canadian Geotechnical Conference.*

Vandiver, V. V. (2002). "Biology and control of algae." *Agronomy Department, Florida Cooperative Extension Service, Institute of Food and Agricultural Sciences, University of Florida.*, SS-AGR-34, 1-7.

Villar, O. M. (1995). "Suction control oedometer tests on compacted clay." *Proceedings of the 1st International Conference on Unsaturated Soils.*, 201 - 206.

Wheeler, S. J. (1988). "The undrained shear strength of soils containing large gas bubbles." *Geotechnique*, 38(3), 399-413.

Wheeler, S. J., and Sivakumar, V. (1993). *Development and application of critical state model for unsaturated soil.*, Thomas Telford, London.

Wheeler, S. J., and Sivakumar, V. (1995). "An elasto-plasticity critical state framework for unsaturated silt soil." *Geotechnique*, 45(1), 35-53.

Wheeler, S. J., Sharma, R. S., and Buisson, M. S. R. (2003). "Coupling of hydraulic hysteresis and stress-strain behaviour in unsaturated soils." *Geotechnique*, 53(1), 41-54.

Wong, J. C., Raharjo, H., Toll, D. G., and E.C., L. (2000). "Shear strength of undisturbed Bukit Timah granitic soils under infiltration conditions." *Proceedings of the Unsaturated Soil for Asia*, Singapore: 587 - 592

Appendix 1

Labview Calibration Program for the Double-wall Triaxial Cell

Appendix 2

Labview Data Acquisition Program for the Double-wall Triaxial Cell

Appendix 3

Assembly and Dismantling Procedure for the Double-wall Triaxial Cell

Appendix 1

Labview Calibration Program for the Double-wall Triaxial Cell

Calibration of 13 Channels Double-wall Cell.vi
C:\WINNT\Profiles\cip01mjm\Desktop\JamalTestProgram\Calibration of 13 Channels Double-wall Cell.vi
Last modified on 6/10/05 at 10:25 AM
Printed on 6/27/05 at 11:53 AM

Front Panel

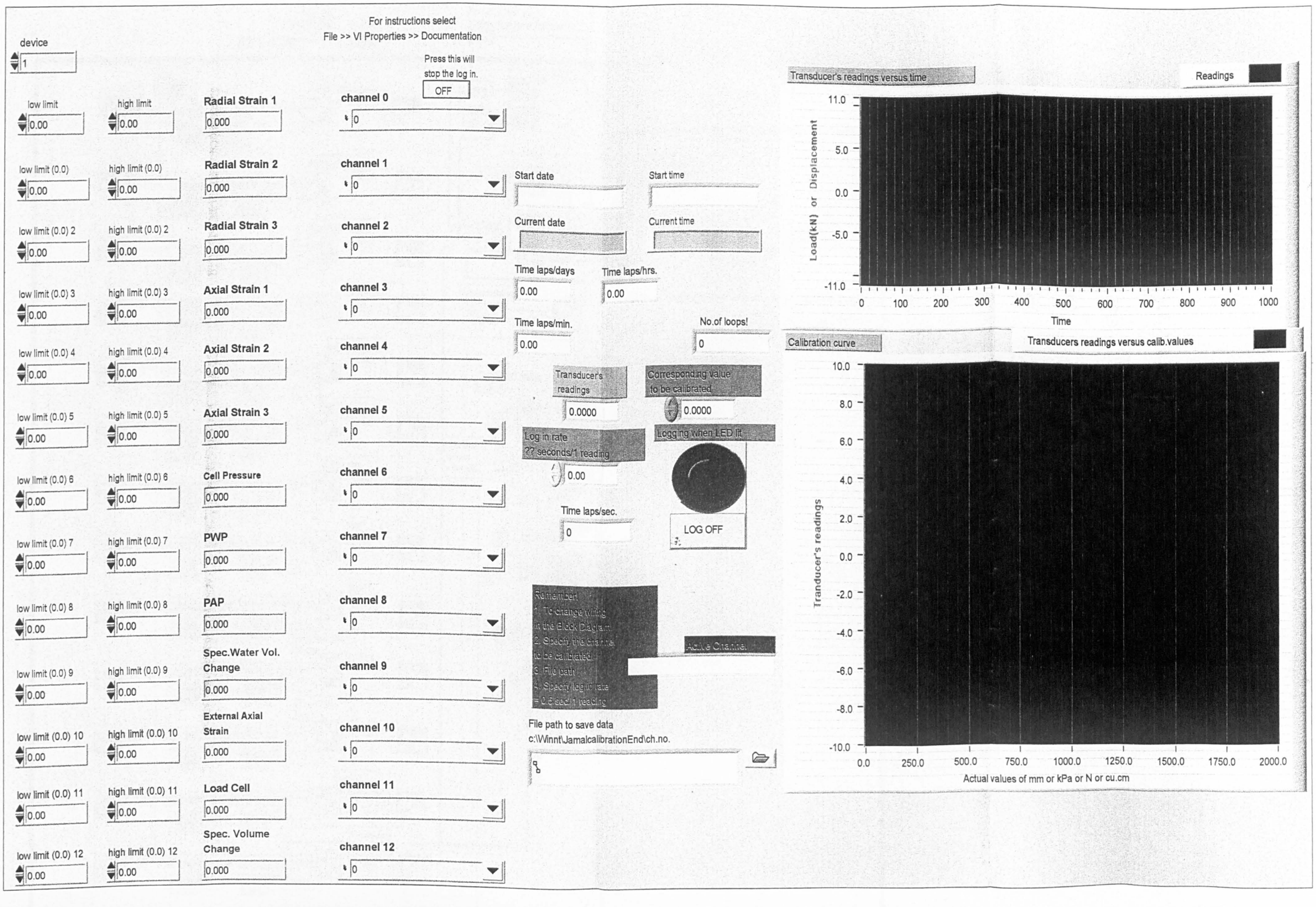

Calibration of 13 Channels Double-wall Cell.vi
C:\WINNT\Profiles\cip01mjm\Desktop\JamalTestProgram\Calibration of 13 Channels Double-wall Cell.vi
Last modified on 6/10/05 at 10:25 AM
Printed on 6/27/05 at 11:53 AM

Block Diagram

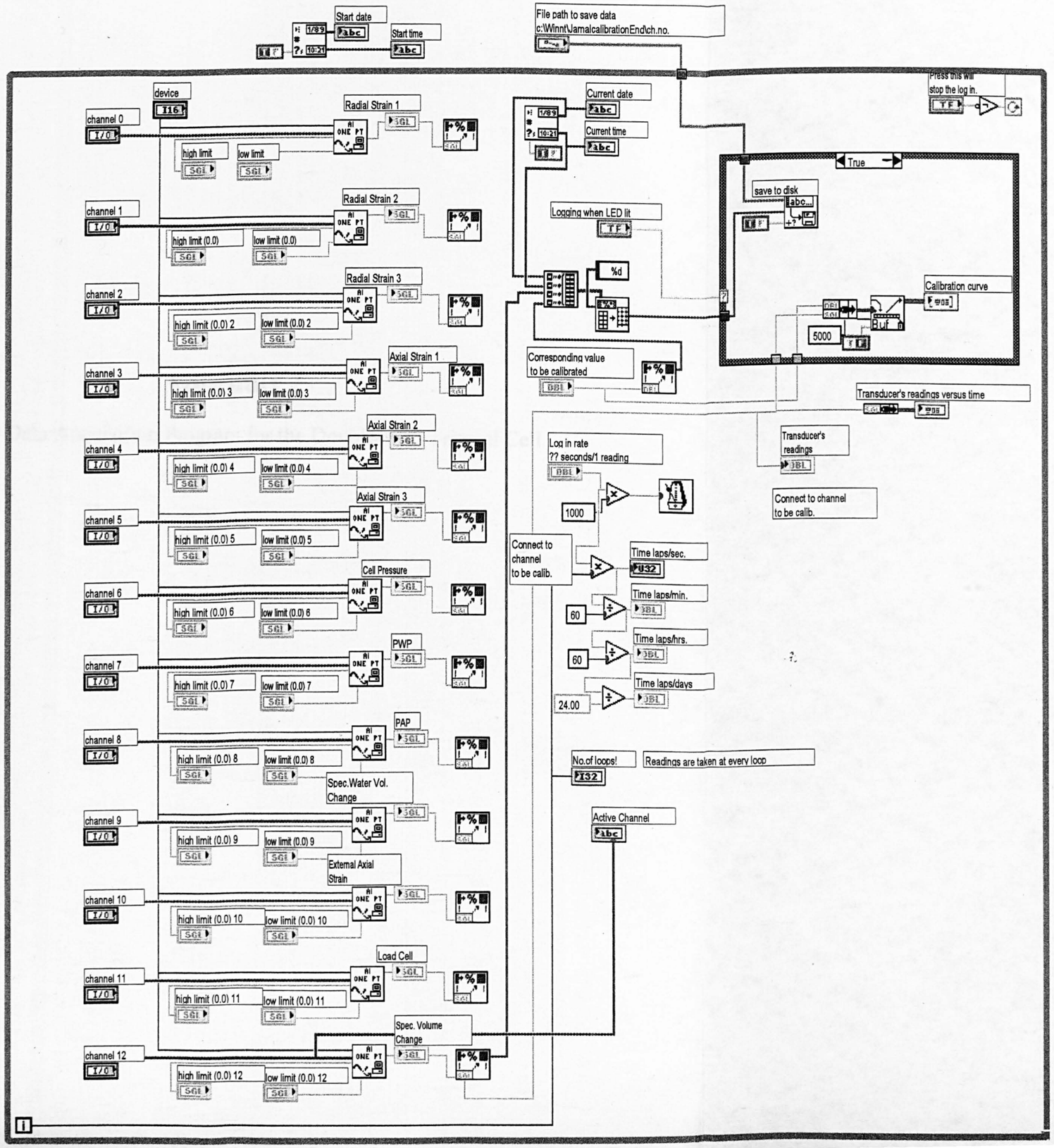

Appendix 2

Labview Data Acquisition Program for the Double-wall Triaxial Cell

13 Channels Data Acquisition Double-wall Cell.vi
C:\WINNT\Profiles\cip01mjm\Desktop\JamalTestProgram\13 Channels Data Acquisition Double-wall Cell.vi
Last modified on 6/10/05 at 10:22 AM
Printed on 6/23/05 at 12:52 PM

Front Panel

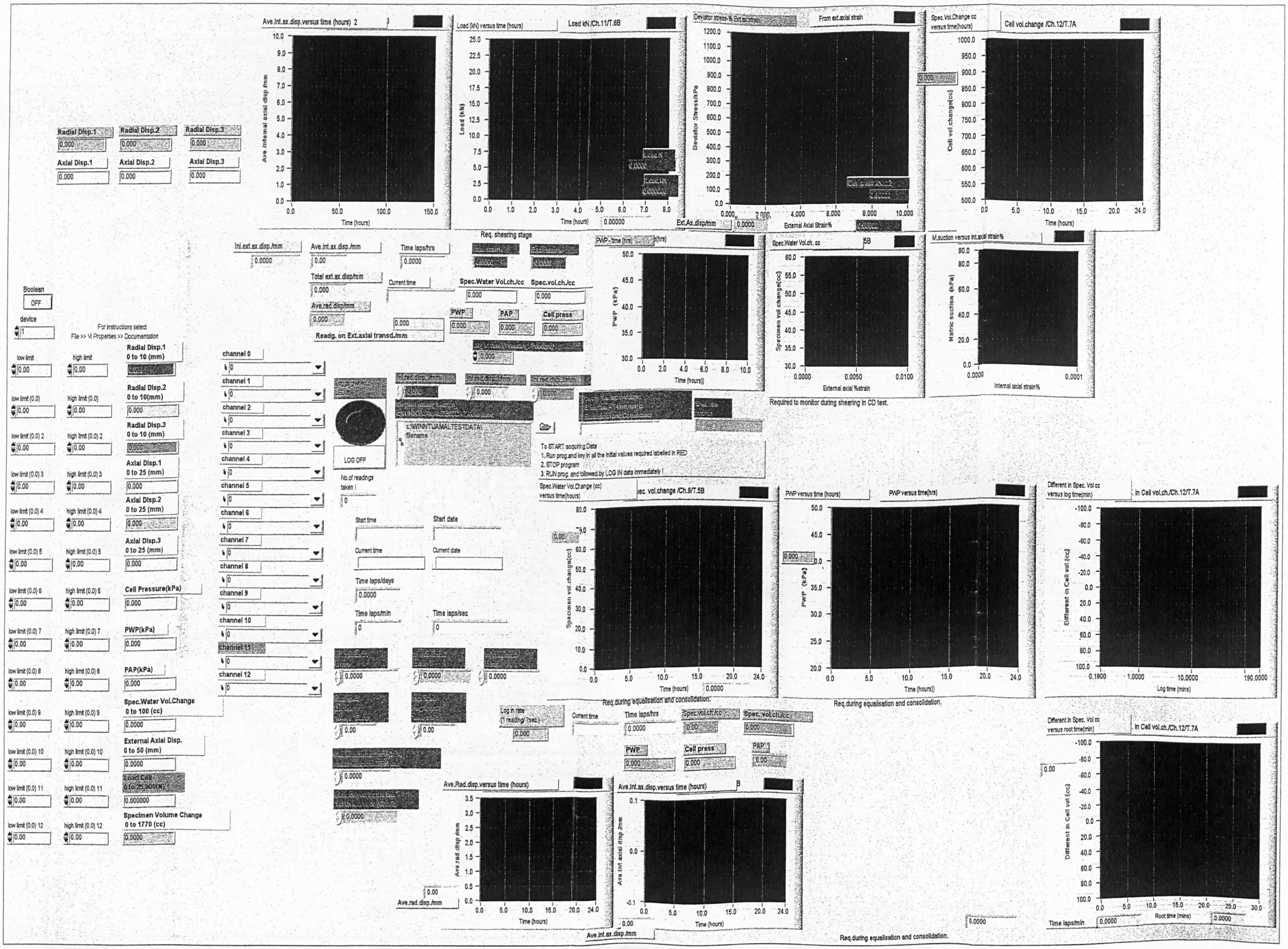

13 Channels Data Acquisition Double-wall Cell.vi
C:\WINNT\Profiles\cip01mjm\Desktop\JamalTestProgram\13 Channels Data Acquisition Double-wall Cell.vi
Last modified on 6/10/05 at 10:22 AM
Printed on 6/23/05 at 12:53 PM

Block Diagram

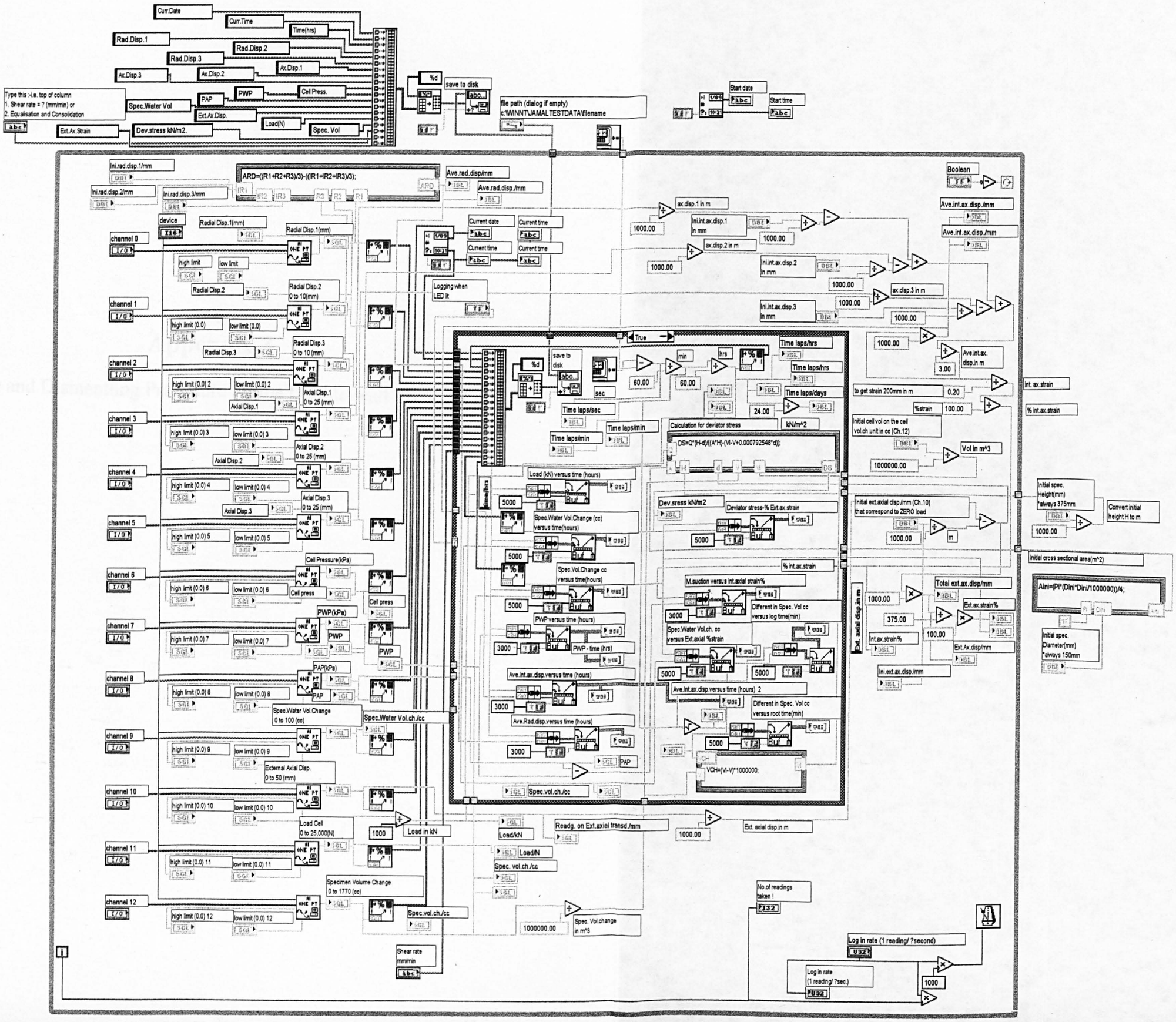

Appendix 3

Assembly and Dismantling Procedure for the Double-wall Triaxial Cell

Appendix 3
Assembly and Dismantling Procedures for the Double-wall Triaxial Cell.

1. Oven dry the soil sample one day before the cell assembly. Mix the dry sample after being cooled for at least 5 hours (i.e. after coming out from the oven) with the appropriate amount of de aired water (i.e. 4%, 6%, 8% etc) in a mixer for 10 minutes.
2. Compact the sample to exactly 375mm height. Each layer takes 1.4 kg of soil and is compacted for 10 seconds using Kongo vibration hammer.
3. Flush to de-air the pore water pressure line.
4. Assemble the high air entry disc.
5. Allow water to pass through the spiral groove below the disc to remove any trapped air by applying a back pressure of 10 kPa from the specimen water volume change unit (100cc) and out to the flushing outlet. Keep the top surface of the disc flooded with a pond of water to keep the disc saturated while doing the rest of the assembly process.
6. Start the process of the specimen placement onto the pedestal. When the specimen is in position place the porous stone followed by the top platen onto the specimen and roll off the membrane at the top and bottom. Grip with an O-ring at each end and connect the air pressure line on top platen.
7. Apply a vacuum and close the valve in the pore air pressure line to keep the specimen under vacuum. Monitor the amount of water entering the specimen through the specimen volume change unit using the data logger to make sure that the ceramic disc does not de-saturate.
8. Remove the mould from the specimen.
9. Apply silicon grease between the membranes. Place the second membrane around the specimen and secure the O-rings (2 at each end).
10. Glue the Perspex curves onto the specimen and fasten the 3 internal axial transducers with their armatures and the extensions.
11. Place the lower inner and outer cell wall segments, the intermediate ring and the upper inner and outer wall segments and fasten the radial transducers' fixing bolts onto the intermediate ring.
12. Bring the top outer cell cap into place and fasten the nuts.
13. Fill the cell with de-aired and de-ionised water from the storage tanks until full by applying air pressure of 20kPa through the vacuum outlets of both tanks.
14. Place the top inner cell cap and fasten it down.
15. Note the amount of water entering the specimen as in STEP 7.
16. Apply a cell pressure of 10kPa and switch off the vacuum. Connect the pore air pressure line to the top of the specimen.
17. With all the valves closed again, start applying a cell pressure of 50kPa, pore air pressure of 40kPa and pore water pressure of 20kPa.
18. Open the cell pressure valve and the pore air pressure valve simultaneously to avoid specimen compression.
19. Connect the transducer wires to the switch box. This includes the load cell, 3 internal axial transducers, 1 external axial transducer and 3 internal radial transducers and run the data logging program without logging in, in order to warm up the system.
20. Position the loading frame cross beam over the load cell piston to avoid the load cell being pushed upwards when a higher cell pressure is applied.
21. Warm up the data logging program for 20 minutes before starting the equalisation, while flushing to de-air the whole plumbing system.

22. Make sure the inner and outer cell pressure valves, pore water pressure valve, pore air pressure valve are closed and set the cell pressure at 100kPa, pore air pressure at 90kPa and pore water pressure at the required suction.
23. Open the inner and outer cell pressure valves and the pore air pressure valve simultaneously to avoid specimen compression.
24. Set the initial values required in the program and STOP the program momentarily. Adjust the level of the large volume change unit and reset the position of the transducer float to be at the centre of its travel.
25. Restart the program again and immediately start the logging.
26. Open the pore water pressure line to start the equalisation process. Water will be expelled and when the specimen water 100cc volume change unit is full (i.e. out of travel) close the pore water pressure line and empty the unit by pushing the water from the volume change unit out into the lower flushing storage tank. Data logging must be switched off during this emptying process. Switch it on again before reopening the pore water pressure valve.
27. After allowing the equalization flow overnight, flushed the compartment below the ceramic disc and determine the volume of diffused air and minus this volume from the volume change indicated by the volume change unit.
28. Stop equalization when the net flow rate is less than 0.05cc in 12 hours.
29. To start consolidation, increase the cell pressure to the required net stress, $(\sigma_3 - u_a)$ while the inner and the outer cell pressure valves closed.
30. Set the logging rate at 10 readings/ second and start the logging and immediately open both cell pressure valves simultaneously to start the consolidation process.
31. Change the logging rate to 1 reading/second after 5 minutes past.
32. Consolidate is considered finish when the specimen volume change ceased to indicate changes.
33. To start shearing, set the required strain rate and proceed while the load cell is just about to touch the top cap so that the zero deviator stress point can be determined.
34. When shearing be cautious not to exceed the capacity of the load cell i.e. 25,000N.
35. At the end of the final shearing stage closed the pore water pressure line to avoid water entering the specimen during the dismantling process.
36. Before dismantling the cell all the applied pressure have to be reduced to zero and this has to be carried out step by step by maintaining the cell pressure 10kPa higher than the applied air pressure to avoid damaging the membranes.
37. This is followed by emptying the cells water by draining it through the inlets of the inner and outer cells at the base platen. This process can be speed up by applying pore air pressure of 50kPa through bleed valves at the inner and outer top plates.
38. This is followed by the dismantling process of the cell parts in reverse order to as they were assembled i.e. in descending order from step 20, 19, 14, 12, 11 and 10.
39. At this stage the specimen is ready to be removed from the bottom pedestal and to carry out the gravimetric moisture content test.
40. Then the ceramic disc was removed from the base pedestal to undergo another saturation process for the next test.
41. The surface of the base plate and the O-ring grooves were wiped cleaned from dirt before the next assembly process begins.